The development and validation of a computational fluid dynamics model of an industrial watertube boiler burning bagasse

by
Philip Coenrad du Toit

Thesis presented in partial fulfilment of the requirements for the degree of Master of Engineering (Mechanical) in the Faculty of Engineering at Stellenbosch University

Supervisor: Prof Chris Meyer

March 2015

Declaration

By submitting this thesis electronically, I declare that the entirety of the work contained therein is my own, original work, that I am the sole author thereof (save to the extent explicitly otherwise stated), that reproduction and publication thereof by Stellenbosch University will not infringe any third party rights and that I have not previously in its entirety or in part submitted it for obtaining any qualification.

Signature: ……

Philip du Toit

Date: ……

Abstract

Development and validation of a computational fluid dynamics model of an industrial watertube boiler burning bagasse

P. du Toit

Department of Mechanical and Mechatronic Engineering
Stellenbosch University
Private Bag X1, 7802, Matieland, South Africa

A model of a bagasse fired boiler using the commercial CFD software package, ANSYS® Fluent, was developed. The simulation included heterogeneous and homogenous combustion with species transport after chemical reaction. Since the focus of the study was on the heat transfer to a tube bank in the combustion zone, the required grid resolution in the bank and turbulence model were investigated in detail. The effect of different combustion modelling strategies on the heat transfer was found to be minimal, but fouling on the outside of the tubes had a substantial impact. The model was validated during an experimental campaign with a suction pyrometer and thermal camera utilising optical tomographic and two-colour pyro metric techniques. The simulation methodology was then applied to a new high pressure industrial boiler design suited to cogeneration.

Key words: Industrial watertube boiler, superheater, combustion, heat transfer, bagasse, computational fluid dynamics

Opsomming

Ontwikkeling en validering van 'n numeriese vloeidinamika model van 'n industriële waterbuisketel brandende bagasse

P. du Toit

Departement Meganiese en Megatroniese Ingenieurswese

Universiteit van Stellenbosch
Privaatsak X1, 7802 Matieland , Suid-Afrika

'N model van 'n bagasse brandende ketel is ontwikkel met behulp van die kommersiële CFD sagteware pakket, ANSYS® Fluent. Die simulasie sluit in heterogene en homogene verbranding met die vervoer van spesies nadat die chemiese reaksies plaasgevind het. Die fokus van die studie was op die hitte-oordrag na 'n buis bank in die verbranding sone, dus is die vereiste rooster resolusie in die bank en turbelensie model ondersoek in detail. Die effek van verskillende verbranding model strategieë op die hitte-oordrag is minimaal gevind, maar aanpaksels aan die buitekant van die buise het 'n aansienlike impak. Die model is gedurende 'n eksperimentele veldtog met 'n suiging pirometer en termiese kamera wat gebruik maak van optiese tomografiese en twee-kleur piro-metriese tegnieke gevalideer. Die simulasie metode is toegepas op 'n nuwe hoë druk industriële ketel ontwerp wat geskik is vir gekombineerde hitte en krag opwekking.

Sleutel woorde : Industrial waterbuisketel, stoomverhitter , verbranding , hitte-oordrag, bagasse , numeriese vloeidinamika

Dedication

Dedicated to Selina, who supported me through the hard work.

Acknowledgements

I would like to express my sincere acknowledgement of the following people:

My supervisor, Prof. Meyer, for guidance and patience through this very steep learning curve.

The staff at Qfinsoft and the combustion department of ANSYS® in the states for help with the initial model setup and technical support through-out the work.

The staff at TSB Komati sugar mill for support during the testing.

My colleagues at John Thompson for help with the modelling, testing and comparison of results with years of practical experience.

Table of Contents

List of figures

List of tables

Nomenclature

Symbols

A	Area, m^2
a	Absorption coefficient
A_r	Pre-exponential factor, s^{-1}
A_o	Rate constant, s^{-1}
c_p	Specific heat at constant pressure, J/kg.K
C	Molar concentration, mol/m^3
C_2	Second Planck constant
D	Diffusion coefficient
d	Diameter, m
E	Total energy, J
E	Empirical constant, 9.793
E_r	Activation energy, J/kmol
e	Internal energy, J
F	Force, N
f	mass fraction
G	Reconstructed grey-levels of the red & green channels
G_b	Generation of turbulent kinetic energy due to buoyancy, J/m^3
G_k	Generation of turbulent kinetic energy due to mean velocity gradients, J/m^3
g	Gravitational acceleration, m/s^2
h	Species enthalpy, J/kg
h	Convective heat transfer coefficient, $W/(m^2.K)$
h^0	Standard state enthalpy of formation, J/kmol
I	Unit tensor
I	Radiation intensity

J	Diffusion flux, kg/m^2
k	Thermal conductivity, W/(m.K)
k	Kinetic energy per unit mass, J/kg
k	Rate constant, s^{-1}
k_p	Turbulent kinetic energy at near-wall node p, J/kg
M	Mass transfer from discrete phase to continuous phase
M_w	Molar mass, kg/kmol
m	Mass, kg
N	Number of chemical species
n	Rate exponent
n	Refractive index
Nu	Nusselt number
P	Pressure, Pa
Pr	Prandtl number
R	*R*ate of creation or destruction, kg/(m^3.s)
R	Universal gas constant, 8.31447e+3 J/(kmol.K)
$\boldsymbol{R}$	Volumetric rate of creation, kmol/(m^3.s)
$\hat{R}$	Arrhenius rate of creation or destruction, kmol/(m^3.s)
R_e	Reynolds number
r	Position, m
S	Source term
S	Instrument factor
S_{ij}	Strain-rate tensor
Sc	Schmidt number
S_b	Stoichiometry
s	Direction

s'	Scattering direction
T	Temperature, K
t	Time, s
U	Velocity, m/s
u	Velocity, m/s
u	Component of flow velocity perpendicular to the gravitational vector, m/s
u_p	Mean velocity at near-wall node p, m/s
u^+	Wall coordinate
u^*	Wall coordinate
v	Component of flow velocity parallel to the gravitational vector, m/s
$\boldsymbol{v}$	Velocity of solid zone, m/s
x	Position, m
y^+	Wall coordinate
y^*	Wall coordinate
Y	Mass fraction
y_p	Distance from node p to the wall, m
y	Distance from closest node to the wall, m

Greek symbols

γ	Third body efficiency
δ	Condensate film thickness, m
ε	Turbulent dissipation rate, m^2/s^3
ε	Emissivity
θ_R	Radiation temperature, K
κ	Von Karman constant = 0.4187

λ	Wave length
μ	Dynamic viscosity, Pa.s
ν	Stoichiometric coefficient
v	Kinematic viscosity, m^2/s
ρ	Density, kg/m^3
σ	Stefan-Boltzmann constant, 5.67e-8 $W/(m^2.K^4)$
σ_k	Turbulent Prandtl number of turbulent kinetic energy
σ_ε	Turbulent Prandtl number of turbulent dissipation rate
σ_s	Scattering coefficient
$\bar{\bar{\tau}}$	Stress tensor, Pa
τ_w	Wall shear stress, Pa
ϕ	Phase function
Ω'	Solid angle, rad
Ω_{ij}	Rotation rate tensor
ω_k	Angular velocity, rad/s

Superscripts

j	Time designation variable in numerical simulation
o	Formation
‘	Reactant
“	Product
.	Flow

Subscripts

atm	Atmosphere
b	Backward

D	Drag
eff	Effective
f	Forward
G	Green
h	Heat
i	Species i
i	Components of tensor
in	at cell entry
j	Species j
j	Components of tensor
k	Kinetic energy per unit mass
k	Components of tensor
lam	Laminar
m	Mass
p	Particle
ref	Reference
rxn	Reaction
T	Thermal (Soret)
T	Turbulent
t	Turbulent
turb	Turbulent
ε	Turbulent dissipation rate
R	Reactant
R	Red
r	Reaction r
s	Path length

sph	Sphere
v	Volatiles
w	Evaporating/boiling material
OX	Oxidant
out	at cell exit
P	Product
pyrol	pyrolysis
∞	Continuous phase
o	Initial

Abbreviations

CV	Control volume

1. Introduction

The global change to renewable energy shifts the focus even more to energy sources derived from biomass as it is already contributing substantially. Thermochemical conversion of bagasse plays an important role in bioenergy amongst other fuels such as woody biomass. (Shanmukharadhya 2007). Therefore bagasse was used as the fuel in this study.

There are various terms and names for components that are very specific to the boiler industry and therefore need to be clarified before the topic of the study can be addressed. The flow of air, fuel, combustion gas and steam inside a medium pressure industrial watertube boiler will be discussed next with reference to Figure 1.1.

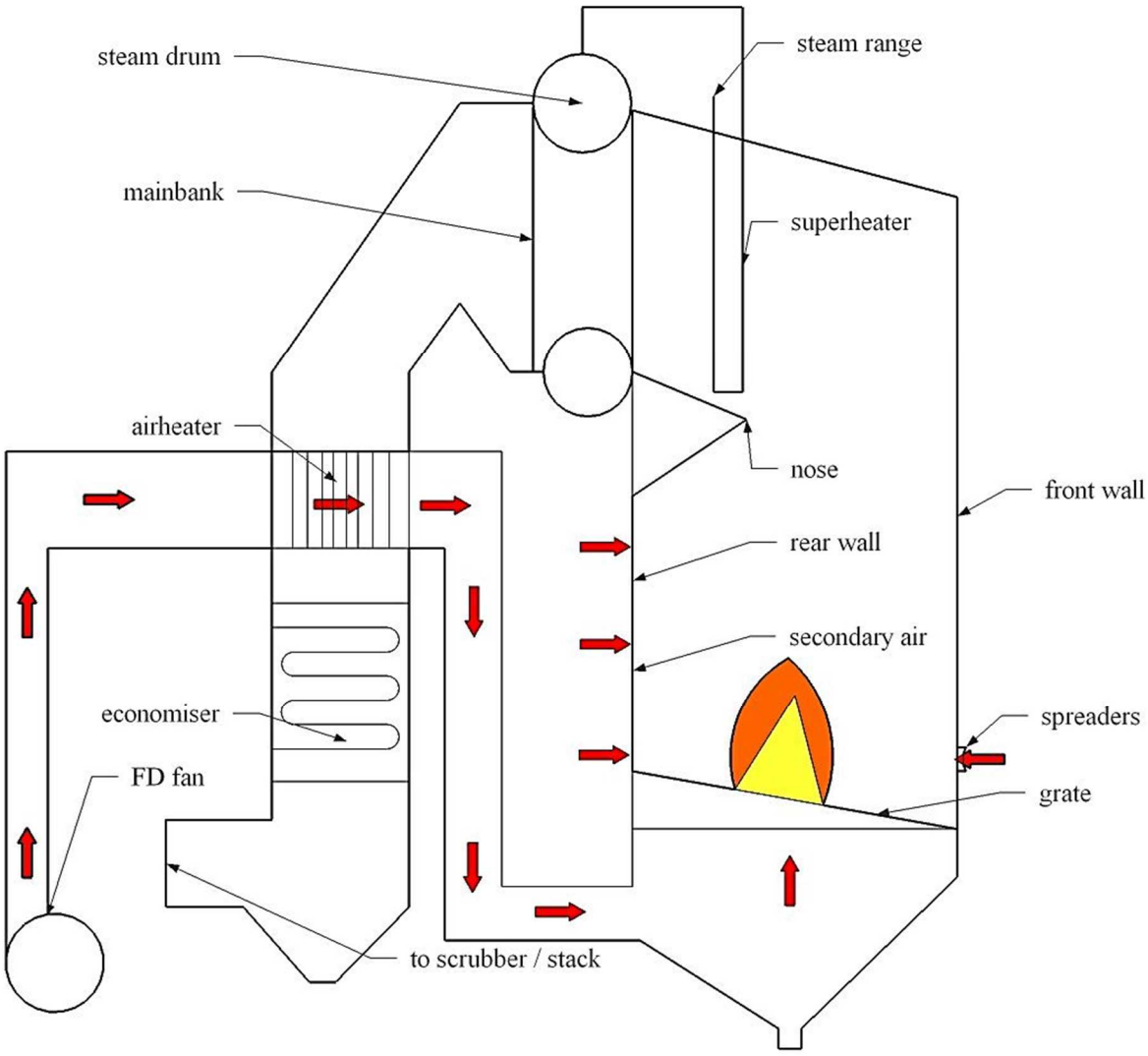

Figure 1.1: Boiler Sectional Side Elevation

The Forced draught (FD) fan blows ambient air through the airheater, interconnecting ducting and grate into the furnace. This is called the primary air and accounts for 85 % of the total air flow.

The airheater heats this air by utilising the energy from the combustion gas at the outlet of the mainbank. It consists of tube plates at the top and bottom. A bundle of tubes are located vertically between these plates. The combustion gas flows inside these tubes downwards while air flows horizontally through the bundle on the outside.

This heating is important for high moisture biomass fuels such as bagasse in order to maintain stable combustion. The remaining unheated air fractions are called spreader air and secondary air at 6 % and 9 % respectively for which a higher pressure fan is used, the secondary air or SA fan.

The bagasse is metered by feeders located above the spreaders. The spreader air blows the bagasse into the furnace via the spreaders on the front wall. This pneumatic fuel spreading is achieved by means of a jet as the air flows through a narrow slot located behind a metal plate. The bagasse particles fall onto this plate and is injected into the combustion zone. The secondary air also enters the furnace at high velocity through 3 rows of nozzles at different elevations between the furnace wall tubes of the rear wall. Refer to the red arrows in Figure 1.1 for the direction of airflow.

Combustion takes place primarily just below the nose of the furnace. The combustion gas flows upwards under a slight negative pressure delivered by the induced draught (ID) fan. The ID fan is located before the chimney stack. Therefore the furnace is maintained at a balanced draught condition by the FD and ID fan. The gas flows through the superheater tube bank heating the steam and across the mainbank transferring heat to the saturated steam water mixture.

The superheater and mainbank both consist of an array of tubes. The elements of the superheater hang from the roof of the cavity in the form of loops. The mainbank tubes are connected to drums at the top and bottom. The combustion gas flows from the outlet of the mainbank through the airheater tubes and over the finned tubes of the economiser where the feedwater flowing to the steam drum is heated.

The economiser is another tube bank that differs from the other heat exchangers in its horizontal layout. The sub cooled feedwater flows horizontally counter to the gas flow in order to maximise the heat transfer. From this point onwards the energy in the gas is considered as a loss since no further heat is recovered. It flows to the gas cleaning equipment, e.g. a scrubber, the ID fan and chimney stack.

Saturated steam flows from the steam drum to the superheater elements. The steam flow inside these tubes can be parallel to the gas flow in high temperature regions or counter flow. The elements discharge into a header which is routed to the steam range that transports all the superheated steam to the turbines.

The biomass specific boiler components are the airheater, static pinhole grate and refractory band in the combustion zone. Since bagasse burns primarily in suspension, movement of the grate is not required and therefore a pinhole grate is used. The ash is transported to the discharge hopper via steam jets. A pinhole grate consists of rearwall tubes bent to a header in front of the ash discharge hopper. Grate bars are bolted to this frame and forms the static surface where the fuel burns. The refractory band provides the thermal inertia required for combustion stability as the moisture content of the biomass fuel varies.

The latest pollution legislation in South Africa (Air Quality Act (ACT no. 39) 2004) requires more environmentally friendly boilers. Combustion and detailed radiation modelling was not required until the implementation of this legislation and the current co-generation drive in South Africa which led to the need for higher pressure, more efficient boilers with lower emissions. This presents challenges with e.g. new superheater designs and thus more detailed modelling is needed as steam temperature is critical in order to achieve the required turbine performance.

Traditionally boilers are designed using global combustion reactions to determine the flue gas quantity, composition and properties for the lumped parameter heat transfer calculations to size the boiler and ancillaries. Due to this simplification of the heat transfer calculations neglecting e.g. three dimensional effects, correction factors are required to bring the models in line with actual conditions. Current methods are from (Stephan 2010) and correlates well with site data after applying factors for different fuels, geometries and operating conditions from years of experience.

These calculations are therefore not ideal for the development of new high efficiency, environmentally friendly systems utilising new fuels as correction factors do not yet exist.

During the past 20 years the numerical simulation of heat transfer and turbulent flow phenomena in combustion systems have developed rapidly concurrently with the development of new and more powerful computers. Following this development, commercial Computational Fluid Dynamics (CFD) programs have evolved for use in project planning, optimizing and diagnostic tests of plants. The CFD programs are advanced calculation tools for computations of 3-dimensional turbulent flow with heat and mass transfer. (Computational Fluid Dynamics In Waste-to-Energy Technology 2003)

CFD is a test platform to prove a concept or new ideas. Parametric studies can be done to reduce experimental testing. Systems can be simulated and data obtained that are not easily tested or measured.

The primary objective of this study was to develop a physically consistent model that can predict the steam temperature from an industrial watertube boiler burning bagasse reliably. It must take all the aspects that influence this result into account with the corresponding sensitivity. Boiler no. 3 at TSB Komati sugar mill was simulated with the commercial software, ANSYS® Fluent version 15.0, as a case study. This boiler is a typical example of a bagasse combustor at industrial scale, 25 MWe, and medium pressure.

The secondary objective was to refine this model through detailed validation. Global measurements, such as steam temperature and averaged combustion gas conditions after the mainbank, were recorded. This data was traditionally used to calibrate the lumped parameter model. However due to the higher level of detail in the modelling, 3 dimensional data closer to the combustion zone was needed requiring more sophisticated instruments than was used in the past on boilers.

A Literature study was undertaken to investigate the feasibility of the thesis by focusing on the aspects of bagasse boilers modelled up to date, the findings and how the models were applied. The standard practice of bagasse boiler simulations were reviewed in order to select the correct CFD sub models. Experimental work conducted in the past was assessed to select appropriate instruments and plan the testing strategy.

The theory related to the models available in ANSYS® Fluent was reviewed in order to make the correct choices and select appropriate parameters. A grid was constructed and the boundary conditions specified.

The sensitivity of combustion modelling parameters was tested and the effect on the heat transfer to the superheater checked. The convection heat transfer over the superheater tube bank was modelled in isolation and validated with published empirical correlations. The simulation was validated with detailed measurements in the region around the superheater and the results were interpreted. The modelling methodology was applied to a new superheater design.

2. Literature study

This literature study contains the following aspects relating to the CFD modelling of an industrial watertube boiler burning bagasse:

- Discussion of bagasse combustion modelling performed in the past
- Standard practice of modelling
- Experimental work conducted in the past and outcomes

2.1. Bagasse combustion modelling

SRI (Australia)

The earliest CFD modelling of bagasse was performed in Australia by individuals linked to the Sugar Research Institute (SRI).

(Luo & Stanmore 1992) from the University of Queensland studied the combustion characteristics of bagasse and determined the rate kinetics for the devolatilisation and char combustion. Their studies on fuel moisture indicated that the total burnout rate of the furnace suddenly decreased at a moisture content of 60 %, which is found in practice as well.

(Woodfield, Kent & Dixon 2000) and (Woodfield et al. 1999) from the University of Sydney studied bagasse combustion instability due to moisture content. Steady state and transient models were set up. The geometry used was for a typical industrial watertube boiler 18.3 m high x 9.46 m wide x 7.56 m deep. The operating conditions were 109 MW thermal, burning 70 t/h bagasse, with 250 t/h air and steam pressure around 20 bar. Typical bagasse was used at 51.5 % moisture content.

They found that instabilities occur at high bagasse loadings as a result of the competition between the fuel supply- and drying rate. A cyclic pattern was observed in practice and with the theory. Gas temperature fluctuations from 300 to 600 °C sensitive to the drying rate, the burnout rate and the ignition criterion (moisture) were seen. The predicted transition between stable and oscillating firing regimes showed reasonable agreement with measurements qualitatively and quantitatively.

Their numerical modelling strategy can be used to assess the effects on stability due to changes in furnace geometry, air flows, fuel flows and other operating conditions, demonstrating the power of CFD. It was seen as a major step forward from the trial and error approach that yielded only minor improvements over 25 years with regards to ignition stability of bagasse-fired boilers. Improvements in the combustion kinetics were recommended.

(Mann 2012), (Mann & O'Hara 2012) and (Mann et al. 2005) investigated the use of CFD to improve the performance and reduce the cost of bagasse fired boilers. The code FURNACE was used to predict the effect of excess air, bagasse moisture, fuel firing rate and grate air flow distribution on boiler operation.

Heat fluxes, gas temperatures and unburnt fuel losses of the same industrial watertube boiler used for the research of (Woodfield, Kent & Dixon 2000) and (Woodfield et al. 1999) were studied. Alternative spreaders and secondary air (SA) were investigated.

A lumped parameter model indicated that the furnace of most bagasse boilers were oversized with regards to residence time, but in practice when the bagasse feed rate was increased, grate deposition and combustion instability increased.

Part of these combustion characteristics is due to the limitations of conventional bagasse spreaders and thus a new swirl spreader combustion system was developed. Overall combustion performance with this system was very good with normal unburnt fuel losses. The boiler capacity could be increased by 15 % with relatively low bagasse moisture and even with high moisture the grate deposition was much less than before. Fewer spreaders could also be used for higher fuel flows, indicating capital cost savings.

FURNACE was used to reduce convection bank erosion with success. The code was improved with regards to convection bank heat transfer as this is normally sacrificed to reduce erosion.

Airheater erosion was also improved by correcting non-uniform flow and flow not parallel with the tube axis. It was also proven with CFD that airheater corrosion is due to non-uniform flow causing cold spots below dew point and not start-up as believed in the past. This was corrected and it also improved the heat transfer considerably.

Future applications of CFD were identified e.g. CO and NO predictions where measurements were made, tangential hot SA and ducting modifications to reduce erosion.

A new bagasse boiler was developed with Clyde Babcock Hitachi (CBH) to reduce capital cost and improve combustion performance. The furnace aspect ratio and height was changed. The size and location of the superheaters and furnace nose shape and size were also changed. SA nozzles on the front wall to enhance the furnace recirculation, residence time and thus burnout was also investigated using CFD. The effect of swirl spreaders was also investigated. The overall results indicated an improvement in combustion with increased heat transfer lower in the furnace and reduced unburnt fuel losses.

The effects of lower volatile bagasse due to stockpiling for cogeneration were also investigated. Assuming that the heat generation of combustible fibre during storage is equal to the calorific value, the net effect is a saving in fuel when burnt at the lower moisture and volatiles. This is due to the drying of the bagasse in the stockpile by the heat liberated from the oxidation of the combustible fibre.

The CFD results using FURNACE indicated that the flame will be closer to the rear wall of the boiler furnace with lower moisture and volatile bagasse and the gas temperatures in the bagasse drying zone near the spreaders will be lower. The greater fraction of combustible fibre consumed in the slower char burn-out phase and reduced drying will slow the rate of bagasse combustion and increase unburnt fuel losses according to the CFD results.

In 2011 the effect of depithed bagasse (bagasse with the smaller particles removed) on boiler performance was studied. These smaller particles are used for manufacturing bagasse by-products such as pulp and paper. Pith has a lower calorific value than bagasse due to higher ash and moisture content. It also has greater external surface area due to the smaller particles which increases particle heat up, drying and burnout rates. These competing effects influence combustion.

The CFD results showed that firing pith only will result in unstable combustion and possible explosions with the lowest boiler efficiency compared to firing bagasse, depithed bagasse and bagasse with a low proportion of pith added. The main flame was predicted near the roof, no

combustion was predicted on the grate and the gas temperatures in the furnace were very low. Thus the boiler fuel and air injecting systems will have to be modified to fire pith only.

The results from the simulation firing depithed bagasse produced a higher fuel burnout, similar combustion than normal bagasse and the highest boiler efficiency. The main flame was slightly higher and closer to the rear wall since the ignition of the larger particles was delayed. A model with a relatively low proportion of pith added to bagasse indicated a small effect on combustion and boiler efficiency compared to bagasse only.

(Rogerson, Kent & Bilger 2007) applied a first order conditional moment closure (CMC) to FURNACE to predict CO and NO in the flue gas.

(Dixon et al. 2005) and (Dixon et al. 2003) were of the first researchers to study bagasse combustion in suspension. Dixon was involved with the practical aspects such as site measurements of e.g. furnace cycling. He also used the lumped parameter boiler design tool, BOILER, to determine inputs for CFD models and studies involving boiler efficiency. He was involved with the projects of (Woodfield, Kent & Dixon 2000), (Woodfield et al. 1999) and (Mann 2012) mentioned above and especially with the development of the swirl spreader.

It was noted in these studies that the flame front is not attached to the bagasse spreaders and that a continuously burning bed at the rear of the furnace stabilises combustion.

The studies on airheater erosion provided an opportunity for extraction of particles before entering the airheater and ducting changes with hoppers were developed.

CFD was used to optimise the internal aerodynamics of the swirl spreader and to resolve erosion problems of unwanted particle recirculation. Modelling and validation of the resulting flame profile and operating envelope of the spreaders were done.

Focus was drawn on SA systems with regards to NO_x and CO working together with (Rogerson, Kent & Bilger 2007) and matching the swirl spreader to a new SA system. The sensitivity of the swirl intensity to the flame pattern was noticed. Increasing the swirl level draws the flame column progressively closer to the front wall of the boiler. A remarkable improvement of combustion with the optimised SA system was achieved.

Bagasse gasification was also simulated. The purpose of this work was to present inputs to a process model of a bagasse gasification cycle to determine the feasibility for power generation.

Various other applications for CFD in the sugar industry were found e.g. vacuum pan stirrer design, evaporator vessel flow modelling and juice clarification.

All the literature of the SRI place great emphasis on validation and explain the effort put in to gather site data to gain confidence in the models. They also continually update and improve the code.

Mobotec Inc (USA)

(Liu et al. 2005) used CFD to analyse the effect of an advanced SA system to reduce CO and NO_x in a stoker-fired industrial boiler burning bagasse. Mobotec's Rotating Opposed Fired Air (ROFA) stages combustion to reduce NO_x.

25 to 40 % of the air is injected in the upper furnace through asymmetric nozzles. The jets enhance the turbulent mixing and induce a rotating bulk flow in the entire furnace.

The boiler is 10.5 m high, 5.8 m deep and 7.3 m wide. The grate is static at a 5 ° angle. It has 4 feeders 1.7 m above the grate and 1.7 m apart. All the surrounding walls are refractory lined. The operating conditions of the boiler was 100 % maximum continuous rating (MCR) of 73 t/h, burning 40 t/h bagasse, excess air of 73 %, steam temperature of 300 °C and pressure of 20 bar. Typical bagasse was used at a moisture content of 51.5 % and 2 % ash on a dry base.

The high moisture bagasse caused severe combustion problems. The emissions of the boiler, particularly CO and Volatile Organic Compounds (VOC), were a few thousand ppm.

In the ROFA case the excess air was reduced to 40 %. ROFA air was injected through 4 boxes, 2 on each side wall, and 2 nozzles per box. Piling on the grate caused re-distributed air flow, but this was modelled separately and found to be negligible.

The model showed poor air fuel mixing on the grate regardless. In a fixed bed the particles form a porous layer of solids and thus the fluid dynamics, radiation, heat and mass transfer between the fuel and surrounding gas need to be approached differently than suspension firing of e.g. pulverised coal.

Fuel distribution is critical to combustion. The fuel inlet parameters were adjusted in the model to qualitatively match the site observations. The relative NO_x decrease between the ROFA case and the baseline was however deemed realistic. For the ROFA case CO reduced from 3000 to 154 ppm.

The furnace exit temperature also reduced by 65 °C. NO_x reduced by 39 % due to the reduced air flow. There was also increased carbon conversion. As a result of the before mentioned effects, the furnace and superheater heat transfer increased by 22 %.

Comparing the contours of temperature, O_2, CO and kinetic energy it was apparent that the increased turbulent kinetic energy of the ROFA enhanced mixing which led to hotter more uniform combustion and less CO. PM emissions were also reduced due to decreased fly ash as a result of the increased carbon conversion.

Further reduction was due to the decreased grate air flow rate which lowered the lift force on the particles. The decrease in fly ash resulted in an increase of bottom ash.

Bannari Amman Institute of Technology (India)

(Shanmukharadhya 2007), (Shanmukharadhya & Sudhakar 2007), (Shanmukharadhya & Sudhakar 2008) and (Shanmukharadhya & Sudhakar 2007) investigated the effect of fuel size and moisture content on bagasse combustion in an industrial watertube boiler with a tangential over fire air system, 5 front wall spreaders and a travelling grate.

Tangential over fire air systems have evolved because of the benefits associated with the design, namely: rapid contact of fuel and air, reduced flame impingement and increased particle residence time. Since tangential SA is flexible and able to control the heat rate, it has a good reputation for low NO_x. The drawbacks of this SA system is that low velocities cause overheating of burners with high volatile fuels and high velocities centrifuge particles out of the combustion zone as unburnt carbon. The limits of combustion for these systems depend on the size of the vortex and the inclination angle of the air nozzles.

During the test period the boiler fired bagasse with a moisture content ranging from 47 to 54 % with no gross instabilities, but at higher moistures instabilities occurred. The air split was 65 % underneath the grate, 5 % through the spreaders and 3 0% through the SA system.

The boiler operating conditions used in the simulation were 100 % MCR at 20 MW electrical load, burning 33 t/h bagasse at 12 % excess air. The O_2 measured in the flue gas was around 5.6 %. Typical bagasse was burnt at 50.5 % moisture.

Generally 250 to 1000 µm particles burnt in suspension, medium size particles burnt at the back of the furnace and larger sizes on the grate. Scanning electron microscope images were used to understand the structure of the surface of the particles and revealed numerous minute holes on the entire surface. The larger particles were cylindrical in shape and the smaller particles irregular.

To determine the effect of fuel size and moisture content on the temperature distribution inside the furnace, 250, 750, 1003 µm and large particles were tested by thermo gravimetric differential thermal analysis (TG-DTA) and differential scanning calorimetry (DSC). From 30 to 130 °C moisture evaporation took place with a peak at 61 °C. Between 250 °C and 350 °C the major decomposition took place with volatiles released during pyrolysis. Above 350 °C was considered as passive pyrolysis at a slower rate up to 516 °C. At temperatures less than 100 °C, moisture was mainly released. Between 100 and 250 °C the extractives decomposed and from 250 to 350 °C mainly the hemicellulose. The lignin and cellulose decomposed between 350 and 516 °C. Char formation occured above 516 °C due to lignin decomposition. The DSC was done in air at 100 °C/min. An increase in peak temperature was observed during the exothermic reaction with increasing particle size. Activation energy also increased as particle size increased.

The CFD model was used to determine the timeline of the processes occurring with the bagasse particles. Firstly just analysing the history of a 181 µm and 668 µm particle from entering the furnace at the spreaders it was found that the smaller particle lost moisture much quicker (in 0.9 s as oppose to 2 s) and reached a substantially higher temperature of more than double the larger particle temperature at 1630 °C which was almost at the adiabatic flame temperature of 1651 °C.

The smaller particle also reached a higher velocity quicker (35 m/s in 0.02 s as oppose to 28 m/s in 0.1 s). The smaller particle was dry at a position 7 m above the grate and the larger particle in the high temperature zone near the rear wall.

An initial region where negligible drying took place was identified for both particle sizes and again proportionally more for the larger size. This region was due to low particle temperature and high gas moisture in the concentrated bagasse stream near the spreader.

It was calculated that the larger particle contained 17 times the amount of moisture per unit surface area as the smaller one. These effects got more pronounced at larger sizes.

The CFD results indicated lower temperatures in the centre of the furnace due to the tangential over fire air. The small particles rose and burnt in suspension, medium particles burnt at the rear and large particles fell on the grate. Recirculation of particles at the front wall was predicted. Most of the combustion took place in the rear half of the furnace.

The tangential over fire air affected the size of the recirculation zone. The vortex gained more momentum with height and was initiated by the SA and later influenced by the undergrate air. The NO_x content in the flue gas also reduced with height due to the vortex.

It was predicted that an increase in under grate air could significantly increase the delay to ignition. As expected the spreader air flow also influenced the delay to ignition and where the piling took place.

The effect of particle pyrolysis and the larger surface area of the smaller particles on the delay to ignition were emphasized as an important influence on thermal fields and combustion stability.

The TG-DTA and DSC data provided the link between particle size, moisture and pyrolysis and the CFD model showed the resulting effect on combustion in the boiler.

2.2. Standard practice of modelling

(Luo & Stanmore 1992) found that the devolatilisation of bagasse is a first order reaction with activation energy of 88 kJ/mol. They also concluded that the char combustion has activation energy of 188 kJ/mol and a reaction order with respect to oxygen of 0.65.

They implemented these rates in a software package called FURNACE written for pulverised fuel (PF) combustion systems by (Boyd & Kent 1986) and co-workers at the University of Sydney to model bagasse boilers. A drying model from (McIntosh 1976) was added to FURNACE to make it suitable for bagasse.

(Woodfield, Kent & Dixon 2000) and (Woodfield et al. 1999) also used the software package FURNACE with a grid consisting of 22 848 cells. This coarse grid was chosen to reduce the computational time since it was a transient simulation. Only half of the furnace was modelled due to symmetry.

The k-ε turbulence model with additional turbulence production due to buoyancy was implemented. Equations for the mixture fraction and its variance were solved as part of a fast chemistry PDF combustion model. The equations for the evaporated water vapour mass fraction were also included.

Radiation was modelled via the Discrete Transfer Method. Fifteen representative particles sizes were used, each with two characteristic dimensions (Dixon 1994). A cylindrical particle shape with length to diameter ratios from 1.6 to 18.2 was used. The bagasse particles were tracked with 13440 trajectory paths using a Lagrangian equation of motion with the drag coefficient for bagasse particles based on measurements of (Nebra & Macedo 1988) and the empirical correlation for a sphere proposed by (Schiller & Nauman 1933).

The drying model for the entrained particles was based on Spalding's B-number approach (Kuo 1986). The heat transfer coefficient was determined from a correlation for small cylindrical or spherical particles in suspension.

The volatiles were divided into tar and pyrolysis moisture. Devolatilisation was modelled using single step Arrhenius form equations. The pre-exponential factor was 2.66×10^4 and 3.17×10^2 s^{-1} for the tar and moisture respectively. The activation energy of the tar was 66.1 kJ/mol and 40.1 kJ/mol for the moisture. These parameters were based on the work of (Stubington & Aiman 1994).

The coal-char model of (Smith 1982) using the char combustion kinetics determined by Luo and Stanmore was used. The pre-exponential factor was 6.27×10^7 s^{-1} and activation energy 188 kJ/mol.

Piling of bagasse on the grate at higher moisture content was considered as a three-dimensional packed bed. The pile occupied a few layers of cells at the bottom of the furnace based on the height which was calculated using a packing density, the number of particles falling on the grate per unit time and the particle burning rate.

The pile was treated as a two-phase system. Due to the loose packing direct heat exchange between the particles was neglected, except radiation. However the particles exchanged heat, mass and momentum with the air and there was thus also a coupling with the gas phase, similar to the entrained particles. Thus although the particles in the bed were not dispersed like their entrained counterparts, the computations were still done in a Lagrangian manner, but with the heat and mass transfer correlations for packed beds.

The drying model was also as described before, but with a heat transfer coefficient for a packed bed (Incropera & De Witt 1986). Ignition was assumed when the moisture content in the pile fell below a critical value. The combustion of the bagasse in the pile was modelled via the Arrhenius kinetic mechanism following the work of (Drummond & Drummond 1996) with kinetic parameters of 2.13 x 10^6 s^{-1} and 92.6 kJ/mol for the pre-exponential factor and activation energy respectively.

Another approach was also used treating the bed as a single continuum with unified characteristics and a constant combustion rate of 0.3 kg/m^2s based on the work of (Fatehi & Kaviany 1994) for adiabatic reverse combustion in a packed bed of wood particles.

(Mann 2012), (Mann & O'Hara 2012) and (Mann et al. 2005) also used FURNACE. The code was improved with regards to convection bank heat transfer. This simulation was done in 2010 and the cell count for the entire boiler was 1.3 million. A coarser grid section of 2880 cells was used for radiation and 17280 particle tracks.

(Rogerson, Kent & Bilger 2007) applied a first order conditional moment closure (CMC) to FURNACE to predict CO and NO in the flue gas. The ultimate analysis of the bagasse was used to estimate the concentration of volatiles from a $(CH_xO_yN_z)_n$ formula for the bagasse.

(Dixon 1994), (Dixon et al. 2005) and (Dixon et al. 2003) used a lumped parameter boiler design tool, BOILER, to determine inputs for CFD models. Porous zones with empirical correlations for pressure drop and heat transfer of e.g. (Zukauskas 1972) for tube banks were added to FURNACE to improve accuracy and reduce computational expense.

FURNACE was modified to account for the homogenous combustion kinetics- and fuel-air mixing limitations at low and high temperatures respectively by introducing a modified eddy break-up model. Provision was also made to account for CO produced from devolatilisation and char combustion by using a fraction of 0.1 to match with site data.

Bagasse gasification was also simulated using an Eulerian multiphase approach with the commercial CFD package CFX.

(Liu et al. 2005) used a grate model in FLUENT through a User-Defined-Function (UDF). The particle tracking was changed so that the particles in the bed follow the movement of the bed. A zone was defined for the bed and particles captured only left when they became light enough to lift or fall in the ash hopper. Primary air entered the furnace through the grate zone. Particle fragmentation occurred when a critical porosity was reached. A particle size distribution was used. A shape factor was used for the particle drag. The CO oxidation reaction was frozen below 777 °C to qualitatively account for kinetic rate limited behaviour in the bed.

The Discrete Phase Model (DPM) with particle radiation interaction was used for particle tracking. The ANSYS Fluent default particle laws of inert heating, drying, devolatilisation and char burnout was used.

The rate parameters for devolatilisation were taken from studies done by (Gera et al. 1999) using a similar biomass fuel, switch grass. For comparisons of different secondary air systems the effect of rate parameters were expected to be small.

The standard k-ε turbulence model and Discrete Ordinates (DO) radiation model was used.

The Eddy Break Up (EBU) model was used for the 2 step homogenous combustion mechanism with a $(CH_xO_yN_z)_n$ formula for the volatiles reacting to form CO before CO_2. The formula and resulting stoichiometric coefficients were calculated from the fuel proximate and ultimate analysis.

The 2 step NO_x model of (De Soete 1975) was used. The evaporator and superheater were modelled with panels of equivalent surface area instead of tubes to account for heat absorption and flow stratification.

577 000 unstructured, hybrid hexahedral cells were used for the furnace. The maximum cell edge size was 0.1 m relatively uniform.

Half the mass of the fuel particles was larger than 1 mm. Fuel was injected through the wall with velocity components specified to spread it on the grate. The larger particles fell on the grate. A reflect type DPM boundary condition was used on this surface and together with the UDF ensured that the particles stay on the grate and do not leave the domain.

(Shanmukharadhya 2007), (Shanmukharadhya & Sudhakar 2007), (Shanmukharadhya & Sudhakar 2008) and (Shanmukharadhya & Sudhakar 2007) set up a 3 dimensional CFD model using ANSYS Fluent. The segregated implicit solver was used. The standard k-ε turbulence model and DO and P1 radiation model (identical to (Woodfield, Kent & Dixon 2000) and (Woodfield et al. 1999)) was used. A pre-PDF was developed for C, H, O, S, N, CO_2 and H_2O species.

The bagasse particles were tracked with the lagrangian method. The particle size distribution used was identical to (Woodfield, Kent & Dixon 2000) and (Woodfield et al. 1999) with the smallest size of 181μm.

The “Mixed-is-burned” approximation with the flame sheet reaction scheme was used. Non-premixed combustion with separate fuel and air streams was modelled.

A single step Arrhenius scheme was used for devolatilisation of combustibles and moisture with kinetic parameters identical to (Woodfield, Kent & Dixon 2000) and (Woodfield et al. 1999). Char oxidation was modelled with a different kinetic relationship.

For the study on moisture a zone at the bottom of the furnace was defined as the grate and bed. In this zone the same drying model, devolatilisation kinetics, char combustion kinetics and particle convective heat transfer was used as (Woodfield, Kent & Dixon 2000) and (Woodfield et al. 1999).

The pressure drop over this porous media was modelled with permeability and an inertial loss coefficient. The pressure drop over the packed bed was calculated by the Ergun equation, a semi-empirical correlation.

2.3. Experimental work conducted in the past

(Luo & Stanmore 1992) used a differential thermogravimetric analyser (DTG) with a heating rate of 15 °C/min to determine the bagasse heterogeneous kinetics. Their measurements on a boiler of temperature, oxygen concentration and wall heat fluxes at steady-state conditions showed reasonable agreement with the CFD predictions. However the details of the instruments used was not stated in the literature.

(Woodfield, Kent & Dixon 2000) and (Woodfield et al. 1999) used air-cooled probes constructed to support k-type thermocouples for boiler gas temperature measurements. Thermocouple readings were corrected for radiation and transient response. The accuracy of the readings were estimated at +-50K based on the uncertainties associated with the emissivities, gas velocity, wall temperature and physical properties of the thermocouple material.

(Rogerson, Kent & Bilger 2007) found that the CFD predictions of NO compared reasonably well with boiler measurements, but CO was under predicted.

(Dixon 1994), (Dixon et al. 2005) and (Dixon et al. 2003) saw good comparison with site measurements of CO and CFD predictions.

(Liu et al. 2005) compared measurements and CFD predictions of the baseline case modelled. The mean gas temperature over the cross section 3.4 m above the grate differed with 100 °C, but errors in measurements were suspected. The type of pyrometer used was not mentioned. CO measured was 3470 ppm compared to 2948 predicted. NO_x was over predicted (0.14 lb/MMBtu measured and 0.31 lb/MMBtu predicted).

(Shanmukharadhya 2007), (Shanmukharadhya & Sudhakar 2007), (Shanmukharadhya & Sudhakar 2008) and (Shanmukharadhya & Sudhakar 2007) used scanning electron microscope images to understand the structure of the surface of the bagasse particles. To determine the effect of fuel size and moisture on the temperature distribution inside the furnace, 250, 750, 1003 µm and large particles were tested by thermo gravimetric differential thermal analysis (TG-DTA) and differential scanning calorimetry (DSC).

The maximum predicted temperature was around 1300 °C at the neck of the furnace which was confirmed with measurements. CFD predictions at different elevations also compared well with measurements. Temperature measurements along the depth at grate level agreed very well with CFD predictions and showed the same increasing trend from the spreaders to the rear wall. Temperature measurements at the grate windows over the width of the boiler at the front, middle and rear showed the same increasing constant qualitative and quantitative trend as the CFD.

One point of concern is that no mention of suction is made when describing the pyrometer used, which raises the question about the accuracy of the pyrometer. A “specially built k-type chromel-alumel thermocouple in a flexible 316 SS tubing (8 mm)” was used.

No corrections for e.g. radiation errors as done by (Woodfield, Kent & Dixon 2000) and (Woodfield et al. 1999) were mentioned. A suction pyrometer is required at these high temperatures. This instrument is discussed in Chapter 3, section 3.1.

3. Experimental setup and procedure

Tests were conducted at TSB Komati boiler no.3 on 4 September 2012. It was subcontracted due to the fact that John Thompson did not own the correct equipment to measure temperatures in excess of 450 °C at the time.

A suction pyrometer was used. This instrument measures the true gas temperature by eliminating radiation and conduction effects as the gas flows at a high velocity over the thermocouple and the convection heat transfer dominates. Therefore the gas velocity over the thermocouple is critical in order to achieve accurate measurements.

(Liptak 1993) states that 100 to 150 m/s are mostly used. Subsequent to the tests, the velocity over the thermocouple was calculated at 11 m/s, based on the pump delivering 10 l/min at STP (20 ºC, 1 bar atmospheric). The research indicates that the error could be hundreds of °C.

Various academic, research and industrial institutions in South Africa were approached to source a suction pyrometer, but with no success. As a last resort a unit was purchased from Paul Gothe GmbH in Germany and the tests repeated in the weeks of 29 July and 31 September 2013. Thermal cameras were also used.

3.1. Experimental setup

Boiler no.3 at TSB Komati was chosen for this study primarily because various modifications were made to the superheater in order to meet the contractual steam temperature. The performance of this unit thus had to be better understood.

Other advantages of this plant is that it burns bagasse exclusively, eliminating the possibility of fouling on the heat transfer surfaces due to coal and it is the newest sugar mill in South Africa running at stable conditions.

The boiler capacity is 150 t/h of superheated steam at 31 bar and 410 °C. The output is 117 MW thermal and 20 MW electrical. Since the focus of the study is the superheater performance, the most important variables measured were the steam flow, steam temperature and steam pressure.

The instrumentation on the plant is regularly calibrated and therefore the data from the distributed control system (DCS) was used. From this information the global effect on steam temperature can be seen, but in order to validate the CFD model, further insight into the flow field around the superheater is required.

Therefore temperature transverses were done in front of and behind the superheater at two elevations. Thermal cameras were also used in this area to observe the flame position and shape, particle tracks and gas temperature.

The suction pyrometer system consists of a lance, cooling water pipes, a gas cooling coil, condensate trap and ejector as shown in Figure 3.1.

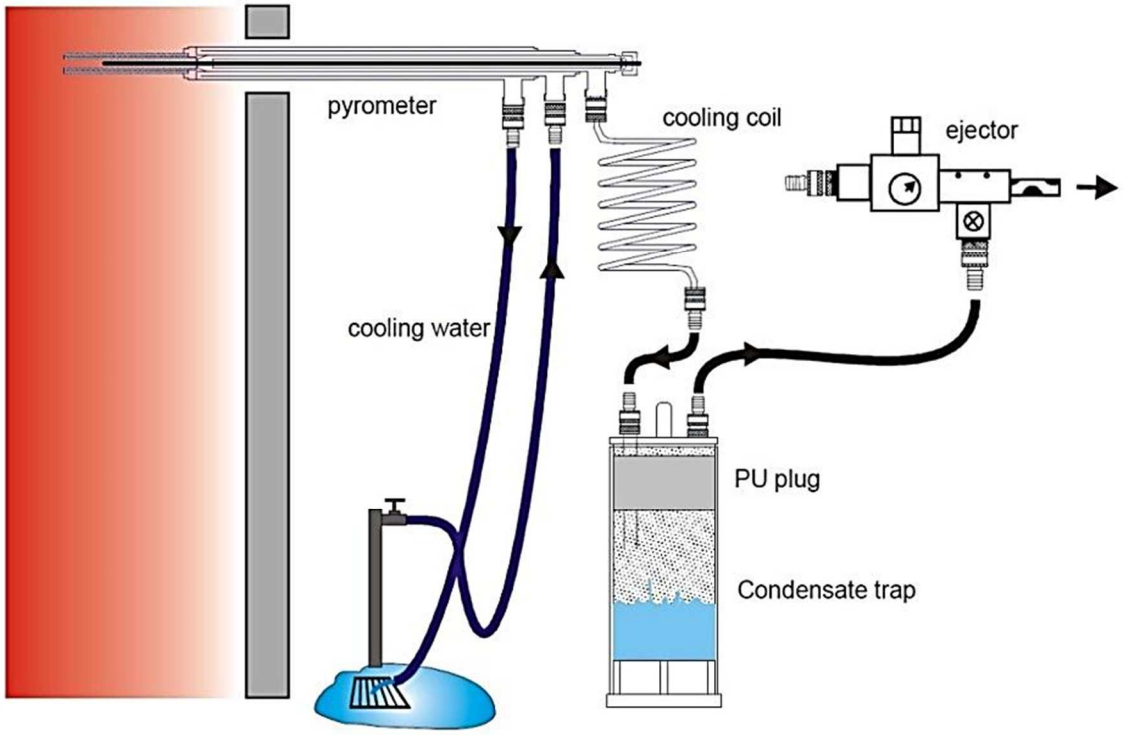

Figure 3.1: Diagram of suction pyrometer system (Paul Gothe 2013)

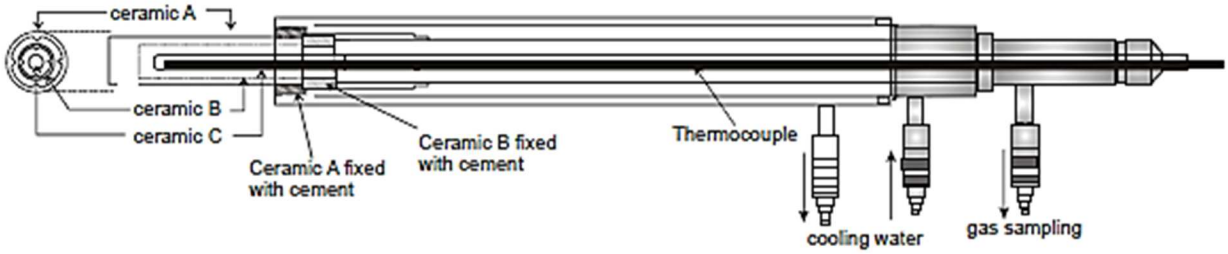

Figure 3.2: Diagram of suction pyrometer lance and sleeve (Paul Gothe 2013)

The lance is manufactured from Titanium to reduce weight and flexibility. These aspects are important at a length of 6.5 m. The instrument consists of an outer annulus, inner annulus and central core.

Water flows along the outer annulus and back through the inner annulus to provide cooling. The thermocouple wire is situated in the central core and the tip inside a ceramic sleeve at the end of the lance (see Figure 3.2).

The combustion gas is sucked at high speed over the thermocouple tip and then through the cooling coil, condensate trap and into the venturi of the compressed air ejector. At high suction rates or low cooling water flow the sucked gas can exceed 80 °C. The cooling coil protects the rubber hoses against melting.

The condensate trap prevents moisture damage of the ejector. It also conditions the gas for species measurement. Due to the high moisture in the bagasse a considerable amount of condensate is formed.

The compressed air ejector is a very important component of the instrument since it ensures a gas speed over the thermocouples in excess of 80 m/s. It contains a pressure reducing valve to regulate the flow and a sound absorber.

Besides the speed of the gas, the arrangement of the radiation shield is also very important for the accuracy of the device. The instrument used in this experiment is in accordance with the International Flame Research Foundation (IFRF) standard. It consists of three ceramic shields.

The inner ceramic sleeve covers the thermocouple completely with a tight fit. The gas sampling takes place through a hole in the outer sleeve. A third sleeve fits loosely between the two to allow gas flow. At a velocity in excess of 80 m/s the equilibrium thermocouple temperature using this shield is equal to the gas temperature without the need for correction. Therefore the accuracy of the device is equal to the accuracy of the type K thermocouple used, which is -3.5 °C at 1000 °C according to the calibration certificate.

The response time of the instrument depends on the size of the shield and the suction velocity. From ambient to 1600 °C it takes 5-8 min to reach equilibrium temperature at a suction velocity of 150 m/s. It takes a further 3-4 min for subsequent temperature changes of 100 °C.

The Durag video based Thermography System used during the experiments consists of a water-cooled lance similar to the pyrometer and a lens at the end of the lance with compressed air cooling and cleaning. The camera is connected to a computer to process the images. Refer to Figure 3.3.

Optical tomographic and two-colour pyro metric techniques are used by the camera as illustrated in Figure 3.4. The first step is to capture a digital image of the flame. The red and green images are then separated. Next the gray-scale reconstruction of the two images is performed using tomographic algorithms such as Filtered back-projection (FBP) and Algebraic Reconstruction Technique (ART).

The temperature distribution can then be calculated with the two-colour pyrometric technique, which is widely accepted in the determination of the radiative temperature of solid particles (e.g. soot, fly-ash) in the flame where the emissivity of the medium is not known.

An example of a two-colour technique is the rewriting of Planck's law to the Wein's approximation (Hossain, Lu & Yan 2012):

$$T = C_2 \left(\frac{1}{\lambda_R} - \frac{1}{\lambda_G}\right) / \left[ln\frac{G(\lambda_G,T)}{G(\lambda_R,T)} + ln\frac{S_{\lambda_R}}{S_{\lambda_G}} + \ln\left(\frac{\lambda_G}{\lambda_R}\right)^5\right] \quad (53)$$

With:

C_2 = second Planck constant

λ = wave length

$G(\lambda,T)$ = reconstructed grey-levels of the R & G channels

$\frac{S_{\lambda_R}}{S_{\lambda_G}}$ = instrument factor for calibration

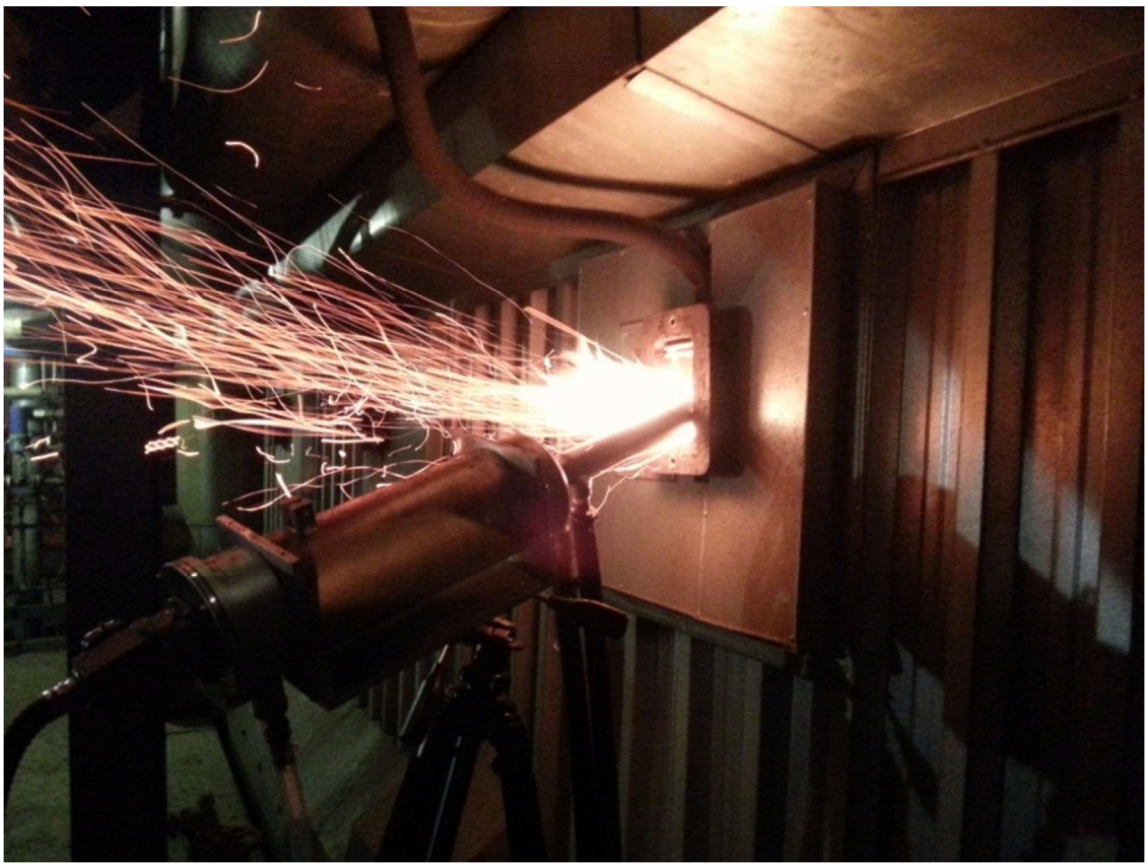

Figure 3.3: Durag thermal camera

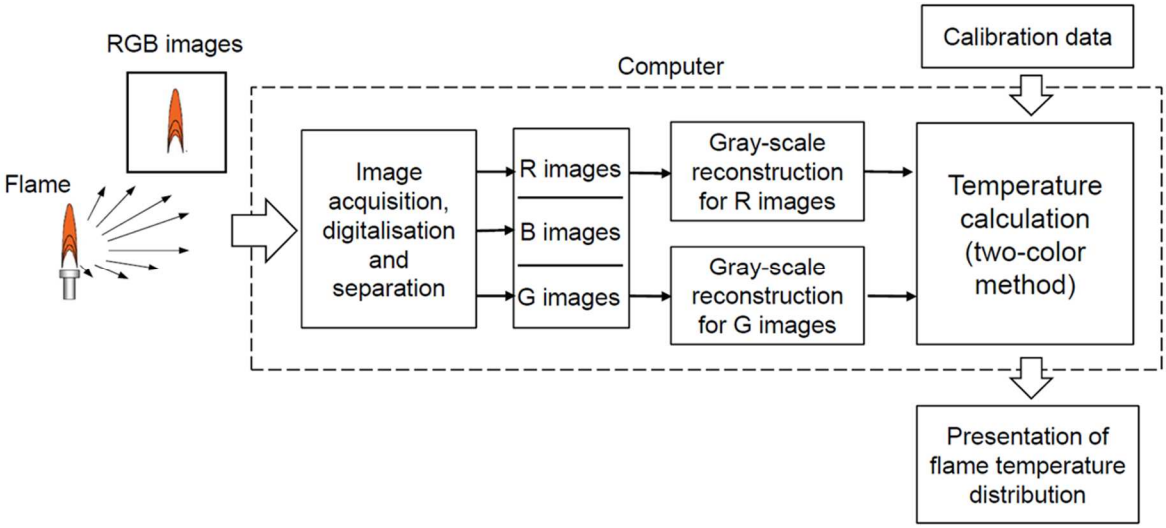

Figure 3.4: Block diagram of optical tomographic and two-colour pyrometric techniques (Hossain, Lu & Yan 2012)

The accuracy of this method was determined by (Hossain, Lu & Yan 2012) at 1.8 % (26 °C) for the temperature range from 1300 °C to 1550 °C.

During the third site visit an in-house developed thermal camera was used. It also requires water cooling and air cleaning, but accommodates enhanced manoeuvrability and temperature contour image processing.

3.2. Experimental procedure

The combustion of bagasse is very unstable compared to coal and highly dependent on particle size grading, moisture and ash. Since it is a waste product from the sugar mill the fuel consistency varies with the process which leads to changes in the combustion. The fuel handling systems can also block and lead to uneven fuel distribution in the furnace.

The load on the boilers varies with the capacity of the sugar factory and in combination with the fuel inconsistency and blockages result in very difficult testing conditions. The tests were done with the boiler running at maximum continuous rating (MCR) and stable conditions. The grate was monitored continuously for piling of bagasse which leads to unstable combustion.

One member of the team was permanently in the control room to maintain stable load and advise when it is suitable to collect data by observing the DCS trends for fluctuations in the system.

The sugar mill relies on a total of three boilers. One of these was taken off line; another ran at a very low load and Boiler #3 at full capacity for the test. Boiler #3 was set on manual and the other boiler on auto to take the load swings via the master pressure controller.

The spreaders were set at the correct angles and air pressure to achieve an even fuel bed on the grate. The secondary air pressures were adjusted as per John Thompson standard with the highest pressure on grate level. The undergrate trim dampers were adjusted to achieve an even air flow over the grate. These are the optimum settings and the boundary conditions of the CFD model were determined accordingly.

During the test the furnace pressure was monitored to anticipate fuel moisture and size grading variations. High moisture, coarse grading bagasse results in piles on the grate. This blocks the airflow and delays the combustion due to a longer drying period and insufficient air fuel mixing. Mini explosions results with furnace pulsations. In severe cases a cycling phenomenon leads to even more unstable combustion. Readings were only taken during stable periods.

Although the boiler was set at a constant load, the demand and response of the other boiler still varied causing changes in steam flow. The combination of steam flow, feedwater flow, steam pressure and drum level was constantly monitored to anticipate upset conditions.

A drop in pressure due to increased steam flow raises the drum water level due to expansion of the steam bubbles. This in turns decreases the feedwater flow to the drum via the level controller which lowers the water level after a while.

When the feedwater controller increases the flow due to the low level, the colder water in the drum shrinks the bubbles and drops the drum level further. The control system compensates for this effect, although instabilities still occur at large load swings. Therefore the drum level is also a good indication of system stability.

The most important parameter monitored was the combustion gas oxygen content at the mainbank outlet. Test measurements were taken at an average value of 3.8 %. There are two Zirconian probes on the boiler, one at each side of the furnace. The variance between the two also indicates the fuel bed distribution and combustion stability.

The fuel feeding equipment was also carefully monitored. Ploughs divert the bagasse off the conveyer belt into the feeder chutes. These ploughs had to be adjusted at times to prevent blockages and the feeder chutes running empty. Fuel samples were also taken from the bagasse conveyer at regular intervals to monitor moisture and ash content.

Temperature traverses were taken with the suction pyrometer in front of and behind the superheater at two elevations. See Figure 3.5. Data was collected at 500 mm increments from the side wall of the furnace across the width to the middle of the boiler.

At the same time images were recorded with the thermal camera and processed to obtain the temperatures. Extreme caution was taken when handling the probe due to the 6.5 m length, height of the testing location on the boiler and flames from the access ports during furnace pulsation.

Plugging of the probe also occurred at times due to the high particle loading in the gas stream. It is thus a very difficult and aggressive testing environment far from laboratory conditions.

Tests were conducted during three different site visits. Due to the incorrect instrument used during the first visit the data of combustion gas temperature was discarded, but O_2 and CO measurements are valid. During the second visit very useful images were captured with the thermal camera and one temperature traverse was completed. The last site visit was dedicated to conducting temperature traverses. The new JT thermal camera was also tested. The results from all the tests will be discussed in Chapter 10.

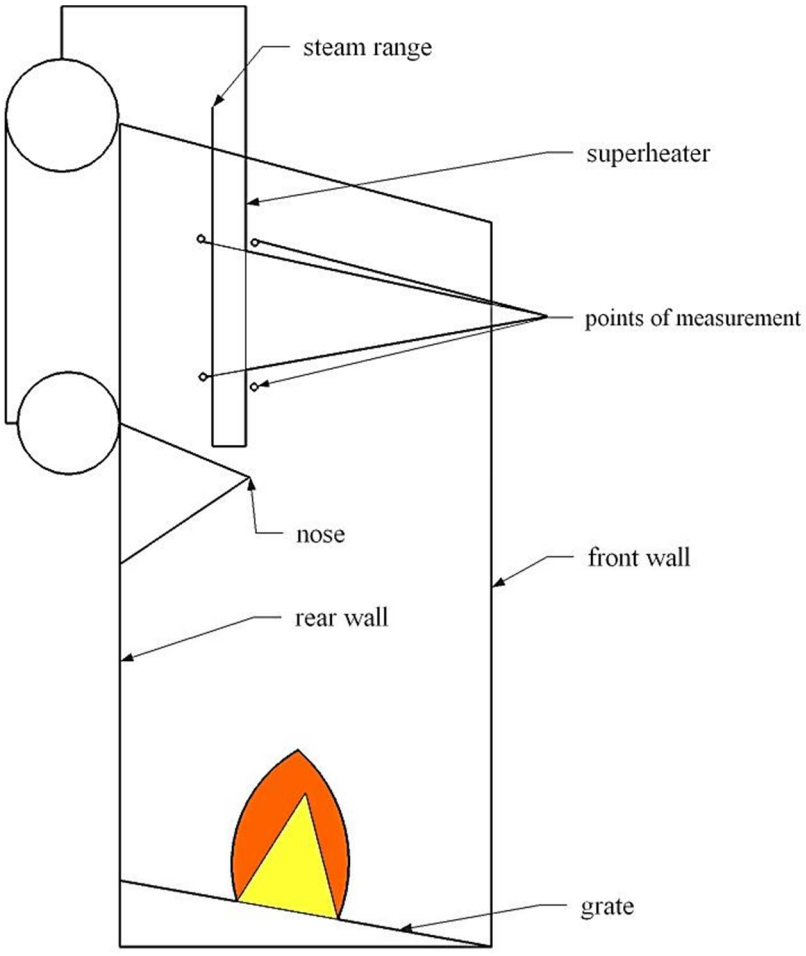

Figure 3.5: Komati schematic layour of sootblower access

4. Numerical methodology

The physics modelled are the flow of air to a combustion chamber and the mixing with the fuel in the form of injected solid particles. The heterogeneous and homogenous combustion with species transport after chemical reaction and associated heat transfer are then modelled in detail.

Euler and Lagrangian reference frames are used for the continuous gas phase and discrete solid phase respectively. The two phases interact through the exchange of mass, momentum and energy. The analytical governing differential equations are discretised by a finite volume method.

4.1. Continuous phase

Conservation equations of the fluid phase

The flow modelled is turbulent and therefore the Reynolds averaged form of the governing equations were utilised (dropping the time dependent term and over bar on the mean velocity, $\bar{u}$):

$$\frac{\partial}{\partial x_i}(\rho u_i)=S_m \tag{1}$$

$$\frac{\partial}{\partial x_j}(\rho u_i u_j)= -\frac{\partial P}{\partial x_i}+\frac{\partial}{\partial x_j}\left[\mu\left(\frac{\partial u_i}{\partial x_j}+\frac{\partial u_j}{\partial x_i}-\frac{2}{3}\delta_{ij}\frac{\partial u_k}{\partial x_k}\right)\right]+\frac{\partial}{\partial x_j}\left(-\rho\overline{u'_\iota u'_j}\right)+\rho g+F \tag{2}$$

ρ = density
μ = molecular viscosity

The Reynolds Averaged Navier Stokes (RANS) equations contain 9 extra variables that can be related to the mean velocity gradients by the Boussinesq hypothesis:

$$-\rho\overline{u'_\iota u'_J}=\mu_t\left(\frac{\partial u_i}{\partial x_j}+\frac{\partial u_j}{\partial x_i}\right)-\frac{2}{3}\left(\rho k+\mu_t\frac{\partial u_k}{\partial x_k}\right)\delta_{ij} \tag{3}$$

The Boussinesq approach is implemented in this work through the k-ε model where 2 extra transport equations are solved for the turbulence kinetic energy, k ($k = (\frac{1}{2}\overline{u'_\iota u'_\iota})$, and the turbulence dissipation rate, ε. The turbulent viscosity μ_t is then computed as a function of k and ε.

Substituting (3) into (2) results in:

$$\frac{\partial}{\partial x_j}(\rho u_i u_j)= -\frac{\partial P}{\partial x_i}+\frac{\partial}{\partial x_j}\left[(\mu+\mu_t)\left(\frac{\partial u_i}{\partial x_j}+\frac{\partial u_j}{\partial x_i}-\frac{2}{3}\delta_{ij}\frac{\partial u_k}{\partial x_k}\right)-\frac{2}{3}\delta_{ij}\rho k\right]+\rho g+F \tag{4}$$

The mass transfer from the discrete phase takes places via the source term, S_m. In this body of work it is due to evaporation of the liquid droplets, devolatilisation and char combustion of the fuel particles.

P is the static pressure, ρg the gravitational body force and F external body forces e.g. from the discrete phase. F also contains porous zone and user defined source terms when applicable.

The energy equation is described by the following:

$$\frac{\partial}{\partial x_i}(u_i(\rho E+P)=\frac{\partial}{\partial x_i}\left[k_{eff}\frac{\partial T}{\partial x_i}-\sum_j h_j J_{\boldsymbol{ij}}+\left(\bar{\bar{\tau}}_{eff}.u_i\right)\right]+S_h \tag{5}$$

T is temperature. k_{eff} is the effective conductivity ($k+k_t$), where k is the thermal conductivity and k_t the turbulent conductivity depending on the turbulence model. The same applies for $\bar{\bar{\tau}}_{eff}$ where an effective viscosity is used. J_{ij} is the diffusion flux vector of species j. S_h is the source term for heat of chemical reaction, radiation, heat transfer between the continuous and discrete phase or any volumetric energy sources defined.

In this body of work the variation of density due to pressure is small compared to variation because of temperature changes. Therefore the flow was resolved as incompressible with the pressure-based solver. The variations of density due to temperature were accounted for by using the ideal-gas relationship.

The following is explained with relation to equation (5):

$$E = e + \frac{v^2}{2} \tag{6}$$

$$h = e + \frac{P}{\rho} \tag{7}$$

e is the internal energy.

For incompressible flows $e \gg \frac{P}{\rho}$ (Cengel & Boles 1994) thus:

$$E = h + \frac{v^2}{2} \tag{8}$$

For a mixture of ideal gases:

$$h = \sum_j Y_j h_j \tag{9}$$

Y_j is the mass fraction of species j and

$$h_j = \int_{T_{ref}}^{T} c_{p,j} dT \tag{10}$$

$c_{p,j}$= the specific heat of species i

T_{ref} for the pressure-based solver used in this model is 298.15K.

The sources of energy due to chemical reaction are the following:

$$S_{h,rxn} = \sum_j h_j^o \boldsymbol{R}_j \tag{11}$$

Where h_j^o is the enthalpy of formation of species j and $\boldsymbol{R}_j$ is the volumetric rate of creation of species j.

Since the pressure-based solver was chosen for this model, pressure work, kinetic energy and viscous heating is not included in equation (5) by default. These terms are negligible in incompressible flows.

Therefore equation (5) reduces to:

$$\frac{\partial}{\partial x_i}[u_i(\rho E)] = \frac{\partial}{\partial x_i}\left[k_{eff}\frac{\partial T}{\partial x_i} - \sum_j h_j J_{ij}\right] + S_h \quad (12)$$

With

$$E = h \quad (13)$$

Species equations

During combustion the gas phase mixture contains a variety of species that need to be tracked, as indicated in the energy equation described above. The transport equation takes the following form:

$$\frac{\partial}{\partial x_i}[u_i(\rho Y_j)] = \frac{\partial}{\partial x_i}J_{ij} + R_j + S_j \quad (14)$$

Y_j = mass fraction of species j

R_j = rate of production or destruction of species j due to chemical reaction

S_j is the rate of creation of species j from the discrete phase and any user-defined sources. The equation above is solved for all the species except the one with the largest mass fraction, which is determined through a mass balance.

In turbulent flows as in the current body of work, the diffusion flux is written as:

$$J_{ij} = -(\rho D_{j,m} + \frac{\mu_t}{Sc_t})\frac{\partial Y_j}{\partial x_i} - D_{T,j}\frac{\partial T}{\partial x_i}\frac{1}{T} \quad (15)$$

$D_{j,m}$= mass diffusion coefficient for species j

$D_{T,j}$= thermal (Soret) diffusion coefficient

Neglecting thermophoretic force:

$$J_i = -(\rho D_{j,m} + \frac{\mu_t}{Sc_t})\frac{\partial Y_j}{\partial x_i} \quad (16)$$

In equation (15) Sc_t is the turbulent Schmidt number ($\frac{\mu_t}{\rho D_t}$ with μ_t and D_t turbulent viscosity and diffusivity respectively).

State equations

Density of the gas phase is calculated with the incompressible ideal gas law as stated below:

$$P = \rho\frac{R}{M}T \quad (17)$$

$$\rho = \frac{1}{\sum_i \frac{Y}{\rho_i}} \quad (18)$$

R is the universal gas constant and M the molar mass.

Turbulence

Turbulence is the physical phenomena in the boiler that forms a link between the flow field, particle motion, rate of chemical reactions and heat transfer. It is therefore imperative to account for the most important turbulent flow characteristics realistically. During the development of the boiler model various turbulence models for the free stream and boundary layers were assessed.

Standard k-ε model

The k-ε model was proposed by Launder and Spalding in 1972 and has become very popular in industrial applications due to its robustness, computational economy and reasonable accuracy. The following describes this semi-empirical model:

$$\frac{\partial}{\partial x_j}(\rho k u_j) = \frac{\partial}{\partial x_j}\left[\left(\mu + \frac{\mu_t}{\sigma_k}\right)\frac{\partial k}{\partial x_j}\right] + G_k + G_b - \rho\varepsilon + S_k \tag{19}$$

$$\frac{\partial}{\partial x_j}(\rho \varepsilon u_j) = \frac{\partial}{\partial x_j}\left[\left(\mu + \frac{\mu_t}{\sigma_\varepsilon}\right)\frac{\partial \varepsilon}{\partial x_j}\right] + C_{1\varepsilon}\frac{\varepsilon}{k}(G_k + C_{3\varepsilon}G_b) - C_{2\varepsilon}\rho\frac{\varepsilon^2}{k} + S_\varepsilon \tag{20}$$

Since the flow is incompressible, the term representing the contribution of the fluctuating dilatation in compressible turbulence to the overall dissipation rate has been neglected in the k equation.

The turbulent viscosity is calculated by:

$$\mu_t = \rho C_\mu \frac{k^2}{\varepsilon} \tag{21}$$

The model constants are:

$$C_{1\varepsilon} = 1.44, C_{2\varepsilon} = 1.92, C_\mu = 0.09, \sigma_k = 1.0, \sigma_\varepsilon = 1.3$$

σ_k and σ_ε are the turbulent Prandtl numbers for k and ε respectively.

G_k is the turbulence kinetic energy due to the mean velocity gradients:

$$G_k = -\rho\overline{u'_i u'_j}\frac{\partial u_j}{\partial x_i} \tag{22}$$

It is modelled similar to the Boussinesq hypothesis:

$$G_k = \mu_t S^2 \tag{23}$$

$$S = \sqrt{2S_{ij}S_{ij}} \tag{24}$$

G_b is the generation of turbulence kinetic energy due to buoyancy. In this work the ideal gas form is used:

$$G_b = -g_i \frac{\mu_t}{\rho Pr_t}\frac{\partial \rho}{\partial x_i} \tag{25}$$

ε is affected by buoyancy through the constant $C_{3\varepsilon}$ based on the work of (Henkes, van der Flugt & Hoogendoorn 1991):

$$C_{3\varepsilon} = tanh\left|\frac{v}{u}\right| \tag{26}$$

In equation (26) *v* is the component of the flow velocity parallel to the gravitational vector and *u* is the component of the flow velocity perpendicular to the gravitation vector. S_k and S_ε are user defined source terms.

Realizable k-ε model

Combining the Boussinesq hypothesis equation (3) with the eddy viscosity formulation equation (21), the following is obtained for the normal Reynolds stress:

$$\overline{u_i'^2} = \frac{2}{3}k - 2\frac{\mu_t}{\rho}\frac{\partial u_i}{\partial x_i} \tag{27}$$

Thus $\overline{u_i'^2}$ becomes negative when the strain is large enough so that

$$\frac{k}{\varepsilon}\frac{\partial u_i}{\partial x_i} > \frac{1}{3C_\mu} \approx 3.7 \tag{28}$$

Which is "non-realizable" since the normal stress is by definition a positive quantity. The Schwarz inequality for shear stresses ($\overline{u_i}\overline{u_j}^2 \leq \overline{u_i^2 u_j^2}$) can also be similarly violated.

One of the weaknesses of the *k-ε* model is the poor prediction of the spreading rate for axisymmetric jets due to the modelled equation for the dissipation rate (ε). The realizable *k-ε* model by (Shih et al. 1995.) addresses the above mentioned deficiencies by a new eddy viscosity formula with a variable C_μ and a new model equation for the dissipation rate based on the mean-square vorticity fluctuation . The resulting equations follow:

$$\frac{\partial}{\partial x_j}(\rho\varepsilon u_j) = \frac{\partial}{\partial x_j}\left[\left(\mu + \frac{\mu_t}{\sigma_\varepsilon}\right)\frac{\partial \varepsilon}{\partial x_j}\right] + \rho C_1 S\varepsilon - \rho C_2 \frac{\varepsilon^2}{k+\sqrt{\nu\varepsilon}} + C_{1\varepsilon}\frac{\varepsilon}{k}C_{3\varepsilon}G_b + S_\varepsilon \tag{29}$$

With

$$C_1 = max\left[0.43, \frac{\eta}{\eta+5}\right],\ \eta = S\frac{k}{\varepsilon},\ S = \sqrt{2S_{ij}S_{ij}}$$

$$C_\mu = \frac{1}{A_o + A_s\frac{kU^*}{\varepsilon}} \tag{30}$$

$$U^* = \sqrt{S_{ij}S_{ij} + \tilde{\Omega}_{ij}\tilde{\Omega}_{ij}} \tag{31}$$

$$\tilde{\Omega}_{ij} = \Omega_{ij} - 2\varepsilon_{ijk}\omega_k$$

$$\Omega_{ij} = \bar{\Omega}_{ij} - \varepsilon_{ijk}\omega_k$$

Where $\bar{\Omega}_{ij}$ is the mean rate-of-rotation tensor viewed in a moving reference frame with angular velocity ω_k

$A_o = 4.04,\ A_s = \sqrt{6}\cos\phi$

Where $\phi = \frac{1}{3}\cos^{-1}\left(\sqrt{6}W\right)$, $W = \frac{S_{ij}S_{jk}S_{ki}}{\tilde{S}^3}$, $\tilde{S} = \sqrt{S_{ij}S_{ij}}$, $S_{ij} = \frac{1}{2}\left(\frac{\partial u_j}{\partial x_i} + \frac{\partial u_i}{\partial x_j}\right)$

The model constants are:

$C_{1\varepsilon} = 1.44, C_2 = 1.9, \sigma_k = 1.0, \sigma_\varepsilon = 1.2$

The model thus performs better than the standard k-ε when the flow has a strong streamline curvature, vortices, rotations and jets according to (Shih et al. 1995.) and (Kim, Choudhury & Patel 1997). These flow characteristics are all present within the boiler and therefore this model was used with a wall function for the initial setup.

Three different types of turbulence near wall treatment were investigated namely wall functions, a two-layer approach and Low-Reynolds-Number (LRN) formulations.

Wall functions

Experimental measurements show that for internal and external flows the velocity near the wall varies logarithmically with the distance from the surface. The fluid near the wall can be devided into 3 regions. In the viscous sublayer right next to the wall, the molecular viscosity plays the dominant role in momentum and heat or mass transfer. The fluid in this region is almost laminar. The outer fully turbulent or log-law region is governed by turbulence. The buffer layer or blending region is situated between these two zones where molecular viscosity and turbulence have equal effects (see Figure 4.1).

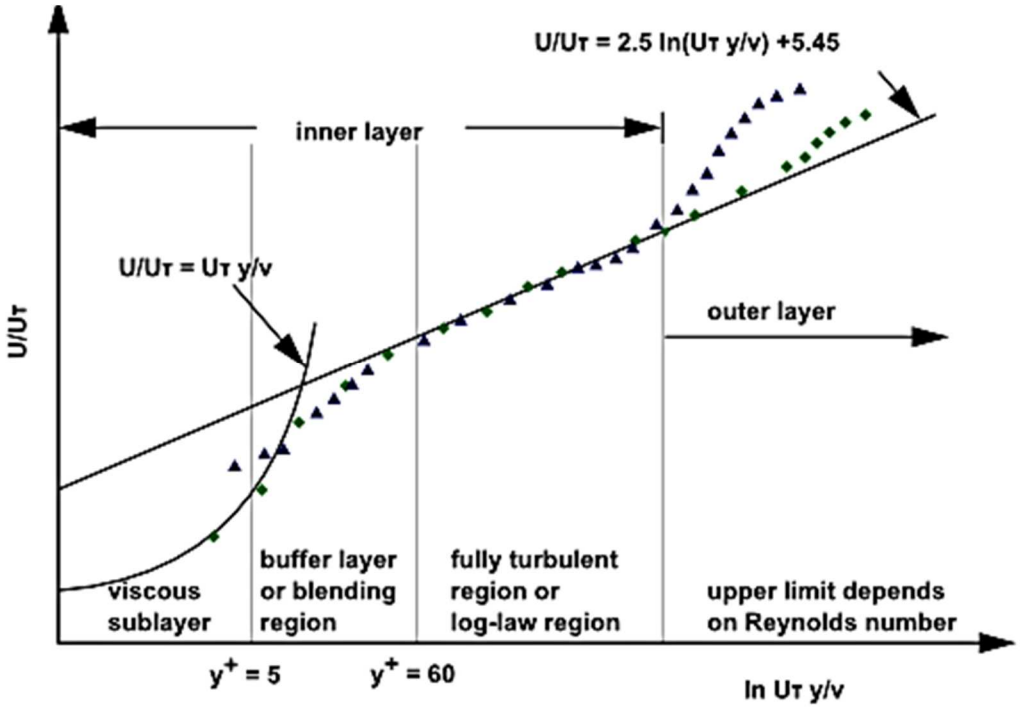

Figure 4.1: Law-of-the-wall (ANSYS Inc. 2013)

The molecular viscosity affected inner region of the boundary layer is not resolved with adequate mesh resolution using wall functions. These semi-empirical formulas bridge the viscosity-affected region between the wall and the turbulent free stream (see Figure 4.2).

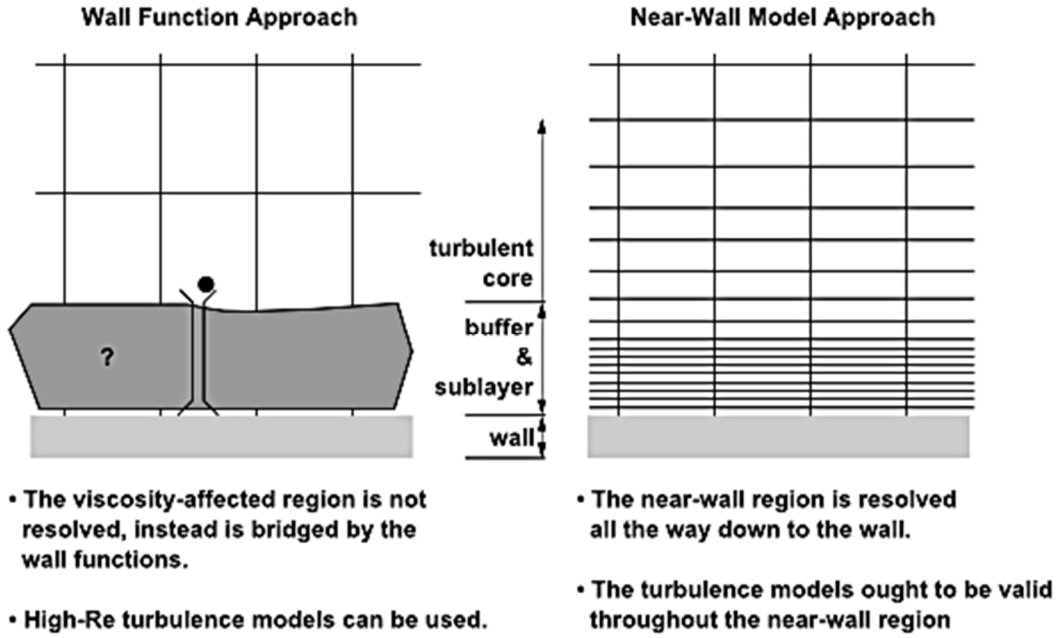

Figure 4.2: Near-wall treatments (ANSYS Inc. 2013)

It requires the first node from the wall to be in the fully turbulent or log-law region ideally. Therefore the y^+ -value is very important in order to model the correct thermal boundary profile and calculate accurate heat transfer. Given the complexity and scale of the simulation it was the option of choice in order to save computational cost.

Standard wall functions

ANSYS® Fluent implements the law-of-the-wall in the following manner:

$$U^* = \frac{1}{\kappa} ln(Ey^*) \tag{32}$$

$$U^* = \frac{U_p C_\mu^{\frac{1}{4}} k_p^{\frac{1}{2}}}{\frac{\tau_w}{\rho}} \tag{33}$$

$$y^* = \frac{y_p C_\mu^{\frac{1}{4}} k_p^{\frac{1}{2}}}{\nu} \tag{34}$$

κ = von Karman constant , 0.4187

E = empirical constant, 9.793

U_p = mean velocity at near-wall node p

k_p = turbulent kinetic energy at near-wall node p

y_p = distance from node p to the wall

The y^+-value is approximately equal to the y^*-value in the case of equilibrium boundary layers for which wall functions were originally formulated.

The general accepted range of y^+ is from 30 to 300 for standard wall functions, (Versteeg & Malalasekera 2007).

A y^*-value of 15 or higher is recommended (ANSYS Inc. 2013). At $y^* \leq 11.225$ the software switches from the Log-Law to the laminar stress-strain relationship, namely, $U^* = y^*$, if standard wall functions are used.

Scalable wall functions

Scalable wall functions prevent the deterioration of standard wall functions at $y^* < 11$. A y^* limit of 11.225 is introduced. Therefore y^* values calculated with equation (34) that are less than 11.225 are set equal to 11.225 and equation (32) is used to calculate U^*, as with standard wall functions.

At $y^* > 11.225$ the scalable wall functions are identical to standard wall functions.

Blended wall functions of (Kader 1981)

So called "enhanced wall functions" are used at higher values of y^+ than 1 when the suite of models called "enhanced wall treatment" is utilised. The linear laminar and logarithmic turbulent laws of the wall are blended using a function by (Kader 1981) thus:

$$u^+ = e^{\Gamma} u^+_{lam} + e^{1/\Gamma} u^+_{turb} \tag{35}$$

With

$$\Gamma = -\frac{a(y^+)^4}{1+by^+} \tag{36}$$

a = 0.01

b = 5

These functions perform better than standard wall functions in the buffer region for $3 < y^+ < 10$.

Non-Equilibrium wall functions

The non-equilibrium wall functions of (Kim, Choudhury & Patel 1997) are recommended for complex flow with separation, reattachment and impingement where the mean flow and turbulence are exposed to pressure gradients and fast changes.

Launder and Spalding's log-law for mean velocity is sensitized to pressure gradients and the two-layer concept is adopted to compute the turbulent kinetic energy in the cells next to the walls.

These cells are therefore assumed to consist of a viscous sub layer and a fully turbulent layer. The resulting log-law is:

$$\frac{\tilde{U}C_{\mu}^{1/4}k^{1/2}}{\tau_w/\rho} = \frac{1}{\kappa} ln\left(E\frac{\rho C_{\mu}^{1/4}k^{1/2}y}{\mu}\right) \quad (37)$$

With

$$\tilde{U} = U - \frac{1}{2}\frac{dp}{dx}\left[\frac{y_v}{\rho\kappa\sqrt{k}} ln\left(\frac{y}{y_v}\right) + \frac{y-y_v}{\rho\kappa\sqrt{k}} + \frac{y_v^2}{\mu}\right] \quad (38)$$

y_v is the viscous sub layer thickness and calculated from:

$$y_v = \frac{\mu y_v^*}{\rho C_{\mu}^{1/4} k_p^{1/2}} \quad (39)$$

$$y_v^* = 11.225$$

(Kim, Choudhury & Patel 1997) validated the wall functions by simulating a back step, blunt-edged flat plate and axisymmetric body. The range of y^+ values used was 13 to 36, 11 to 30 and 40 to 100 respectively.

Two-layer model of (Wolfshtein 1969)

When a two-layer approach is used the inner region of the boundary layer is resolved all the way to the wall. This strategy requires the correct grid resolution in the boundary layer region. The amount of layers close to the wall and the position of these cells are thus important (see Figure 4.2).

A low enough y^+ -value is indirectly important in order to achieve accurate results and generally the computational expense required is higher than using wall functions.

ANSYS® Fluent implements the two-layer approach of (Wolfshtein 1969) as part of the suite of models named "Enhanced Wall Treatment" when the near-wall mesh is fine enough.

This condition is typically satisfied at a y^+ -value of approximately one. A higher y^+ -value might also be acceptable as long as it is well inside the viscous sublayer ($y^+ < 2 \sim 4$). Ideally at least 10 cells are required in the viscosity-affected near-wall region in order to resolve the mean velocity and turbulent quantities.

In the one-equation model of (Wolfshtein 1969) the momentum and *k* equations are retained in the viscosity-affected near-wall region.

The difference from the fully turbulent region where the *k* -ε models is used is that the turbulent viscosity is calculated from:

$$\mu_t = \rho C_{\mu} l_{\mu} \sqrt{k} \quad (40)$$

With:

$$l_{\mu} = y C_l^* \left(1 - e^{-Re_y/A_{\mu}}\right) \quad (41)$$

$$Re_y = \frac{\rho y\sqrt{k}}{\mu} \quad (42)$$

y = distance to the nearest wall

And from (Chen & Patel 1988):

$$C_l^* = \kappa C_\mu^{-3/4} \tag{43}$$

$$A_\mu = 70 \tag{44}$$

Low-Reynolds-Number (LRN) k-ε models

A LRN formulation resolves the boundary layer right up to the wall and therefore requires similar grid resolution and y^+ -value as the two-layer model.

A modification of the k-ε model is made in order to use it at low Reynolds numbers and very close to the wall by means of damping functions to the source terms of the ε transport equation and turbulent viscosity formulation. The transport equations are solved right up to the wall and the damping functions account for the near-wall phenomena.

The damping functions are formulated with specifically defined Reynolds numbers:

$$Re_t = \frac{\rho k^2}{\mu \varepsilon} \tag{45}$$

$$Re_y = \frac{\rho \sqrt{k} y}{\mu} \tag{46}$$

Damping functions for the model of (Chang, Hsieh & Chen 1995):

$$f_\mu = \left(1 - e^{-0.0215 Re_y}\right)^2 \left(1 + 31.66 Re_t^{-1.125}\right) \tag{47}$$

$$f_1 = 1$$

$$f_2 = \left(1 - 0.01 e^{-Re_t^2}\right)^2 (1 - 0.0631 e^{-0.0631 Re_y}) \tag{48}$$

Damping functions for the model of (Abid 1991):

$$f_\mu = tanh\left(0.008 Re_y\right)\left(1 + 4 Re_t^{-\frac{3}{4}}\right) \tag{49}$$

$$f_1 = 1$$

$$f_2 = \left(1 - \frac{2}{9} e^{-\frac{Re_t^2}{36}}\right)^2 \left(1 - e^{-\frac{Re_y}{12}}\right) \tag{50}$$

Damping functions for the model of (Launder & Sharma 1974):

$$f_\mu = e^{\frac{-3.4}{\left(1 + \frac{Re_t}{50}\right)^2}} \tag{51}$$

$$f_1 = 1$$

$$f_2 = 1 - 0.3e^{-Re_t^2} \tag{52}$$

These LRN turbulence models avoid the singularity problem at flow re-attachment points where the wall shear stress approaches zero value since the functions shown is not expressed in terms of y^+ (or wall shear stress implicitly).

The damping functions are applied to equations (20) and (21):

$$\frac{\partial}{\partial x_j}(\rho\varepsilon u_j) = \frac{\partial}{\partial x_j}\left[\left(\mu + \frac{\mu_t}{\sigma_\varepsilon}\right)\frac{\partial \varepsilon}{\partial x_j}\right] + C_{1\varepsilon}\frac{\varepsilon}{k}(f_1 G_k + C_{3\varepsilon}G_b) - C_{2\varepsilon}f_2\rho\frac{\varepsilon^2}{k} + S_\varepsilon \tag{53}$$

$$\mu_t = \rho C_\mu f_\mu \frac{k^2}{\varepsilon} \tag{54}$$

Conservation equations of the solid phase

In solids the following energy equation is used:

$$\frac{\partial}{\partial x_i}[v_i(\rho h)] = \frac{\partial}{\partial x_i}\left[k\frac{\partial T}{\partial x_i}\right] + S_h \tag{55}$$

The symbols in the equation above are consistent with the fluid phase. The convective term is due to rotational or translational motion of the solids and not used in this work therefore the equation reduces to:

$$-\frac{\partial}{\partial x_i}\left[k\frac{\partial T}{\partial x_i}\right] = S_h \tag{56}$$

4.2. Rate of homogeneous combustion

In this work the fuel is assumed to be fast burning and therefore the rate of reaction is governed by the turbulent mixing of the fuel and oxidiser. Only the chemical kinetic rate of CO is considered. This is a valid assumption for biomass and widely accepted and applied (Turns 2011).

The Eddy-Dissipation turbulence chemistry interaction model based on the work of (Magnussen & Hjertager 1976) and (Spalding 1970) is used. The rate of production of species i as a result of reaction r, $R_{i,r}$ is determined by the smaller of the following:

$$R_{i,r} = \nu'_{i,r} M_{W,i} A\rho\frac{\varepsilon}{k} min_{\boldsymbol{R}}\left[\frac{Y_{\boldsymbol{R}}}{\nu'_{\boldsymbol{R},r} M_{W,\boldsymbol{R}}}\right] \tag{57}$$

$$R_{i,r} = \nu'_{i,r} M_{W,i} AB\rho\frac{\varepsilon}{k}\frac{\sum_P Y_P}{\sum_j^N \nu''_{j,r} M_{W,j}} \tag{58}$$

With

$\nu'_{i,r}$ = stoichiometric coefficient for reactant i in reaction r

$\nu''_{j,r}$ = stoichiometric coefficient for product j in reaction r

$M_{W,i}$ = molar mass of species i

Y_R = mass fraction of reactant, $\boldsymbol{R}$

Y_P = mass fraction of product species, P

$min_{\boldsymbol{R}}$ = minimum of reactants

A = empirical constant of 4.0

B = empirical constant of 0.5

The finite rate model computes the sources of species using Arrhenius expressions. The sum of the Arrhenius reaction sources over N_R reactions determines the net source of chemical species i according to:

$$R_i = M_{w,i} \sum_{r=1}^{N_R} \hat{R}_{i,r} \tag{59}$$

where $M_{w,i}$ is the molar mass of species i and $\hat{R}_{i,r}$ is the Arrhenius rate of creation or destruction of species i in reaction r. If the turbulent mixing is governing the speed of the reaction, $R_{i,r}$ according to equation (57) or equation (58) is used instead of $\hat{R}_{i,r}$ in equation (59).

The r[th] reaction in general form follows:

$$\sum_{i=1}^{N} \nu'_{i,r} \boldsymbol{M_i} \overset{k_{f,r}/k_{b,r}}{\Longleftrightarrow} \sum_{i=1}^{N} \nu''_{i,r} \boldsymbol{M_i} \tag{60}$$

N = number of chemical species in the system

$\nu'_{i,r}$ = stoichiometric coefficient for reactant i in reaction r

$\nu''_{i,r}$ = stoichiometric coefficient for product i in reaction r

$\boldsymbol{M_i}$ = symbol for species i

$k_{\boldsymbol{f,r}}$ = forward rate constant for reaction r

$k_{\boldsymbol{b,r}}$ = backward rate constant for reaction r

The Arrhenius molar rate of creation or destruction of species i in non-reversible reaction r ($\hat{R}_{i,r}$) in (41) is given by:

$$\hat{R}_{i,r} = \Gamma(\nu''_{i,r} - \nu'_{i,r}) \left\{ k_{f,r} \prod_{j=1}^{N} [C_{j,r}]^{\left(n'_{j,r} + n''_{j,r}\right)} \right\} \tag{61}$$

$C_{j,r}$ = molar concentration of species j in reaction r

$n'_{j,r}$ = rate exponent for reactant species j in reaction r

$n''_{j,r}$ = rate exponent for product species j in reaction r

The net effect of third bodies (e.g. catalysts) on the reaction rate is given by:

$$\Gamma = \sum_{j}^{N} \gamma_{j,r}$$

$\gamma_{j,r}$ = third body efficiency of species j in reaction r

This effect is ignored in the current work.

The Arrhenius expression is used for the forward rate constant:

$$k_{f,r} = A_r T^{\beta_r} e^{\frac{E_r}{RT}} \tag{62}$$

With

A_r = pre-exponential factor

β_r = temperature exponent

E_r = activation energy

R = universal gas constant

The slowest rate of the mixing and kinetic formulations is used for the speed of the chemical reaction. However for the volatile reaction the kinetic rate was set to a very high value in order to be ignored.

A two-step chemical reaction incorporating the moisture in the fuel and converting all the volatiles to CO was used. A volatile molecule consisting of carbon, hydrogen, nitrogen and oxygen reacting with oxygen to form CO and water was used. In the following reaction the CO is oxidised to CO_2:

$$C_x H_y O_z N_n + (i_1 + i_2) O_2 \rightarrow xCO + \frac{y}{2} H_2O + \frac{n}{2} N_2 + i_2 O_2 \rightarrow xCO_2 + \frac{y}{2} H_2O + \frac{n}{2} N_2 \tag{63}$$

Where:

$$i_1 = \frac{x}{2} + \frac{y}{4} - \frac{z}{2} \qquad i_2 = \frac{x}{2} \tag{64}$$

The volatile reaction mixing constants were set as per the original values determined for PF. The kinetic rate of (Howard, Williams & Fine 1973) was used for the CO reaction with mixing constants of 0.6 for A and 1e+20 for B as recommended by (Scharler, Fleckl & Obernberger 2003).

4.3. Discrete phase model (DPM)

In this work the multiphase flow is modelled with an Euler-Lagrange approach. The dispersed solid fuel particles are tracked individually in a Lagrangian framework while the conservations equations are solved for the continuous gas phase in an Euler reference frame.

In a biomass boiler the particles occupy a low volume fraction of the flow field which is imperative to use this method. The recommended maximum solid-gas volume fraction in order to use DPM is 10-12%.

Equations of motion

The trajectory of a discrete phase particle is calculated by a force balance utilising Newton's 2nd law:

$$\frac{d\boldsymbol{u}_p}{dt} = F_D\left(\boldsymbol{u} - \boldsymbol{u}_p\right) + \frac{\boldsymbol{g}(\rho_p - \rho)}{\rho_p} \tag{65}$$

Neglecting virtual mass and pressure gradient forces since the density of the gas is much lower than the density of the particles. Also forces due to moving reference frames, thermophoretic force, Brownian force and Saffman's Lift force are all neglected since it is not applicable.

$$F_D = \frac{18\mu}{\rho_p {d_p}^2}\frac{C_D R_{e\,d}}{24} \tag{66}$$

With relative Reynolds number:

$$Re_d = \frac{\rho d_p |\boldsymbol{u}_p - \boldsymbol{u}|}{\mu} \tag{67}$$

and

$\boldsymbol{u}$ = fluid phase velocity

$\boldsymbol{u}_p$ = particle velocity

μ = molecular viscosity of the fluid

ρ = fluid density

ρ_p = particle density

d_p = particle diameter

Since the particles in this research are non-spherical, the following correlation by (Haider & Levenspiel 1989) for the drag coefficient is used:

$$C_D = \frac{24}{Re_{sph}}\left(1 + b_1 {Re_{sph}}^{b_2}\right) + \frac{b_3 Re_{sph}}{b_4 + Re_{sph}} \tag{68}$$

$$b_1 = e^{(2.3288 - 6.4581\phi + 2.4486\phi^2)}$$

$$b_2 = 0.0964 + 0.5565\phi$$

$$b_3 = e^{(4.905 - 13.8944\phi + 18.4222\phi^2 - 10.2599\phi^3)}$$

$$b_4 = e^{(1.4681+12.2584\phi-20.7322\phi^2+15.8855\phi^3)}$$

The shape factor is defined as:

$$\phi = \frac{s}{S} \tag{69}$$

S is the surface area of the particle and s is the surface area of a sphere having the same volume as the particle. The shape factor of the particles was calculated using equation (69) after analysing a sample of bagasse. A value of 0.7 was based on cylinder with an aspect ratio of 10. The Rosin Rammler expression was used to represent the bagasse size distribution. Data of typical South African bagasse size grading from (Bernhardt 1993) was utilised.

The coefficient of restitution of the particles was entered to ensure the correct particle wall interaction. This ensures that a realistic rebound of the particle off the surface is achieved, e.g. a value of 1 for the normal and tangential coefficient results in a perfect elastic rebound conserving all momentum. It is particularly important for fly-ash collection and erosion modelling. A polynomial of (Tabakoff & Sugiyama 1980) was used for sand on carbon steel, since bagasse fly-ash is mostly sand.

A bed model was implemented through User-Defined-Functions (UDF). A zone was defined which captures particles passing through. The particles stay in position until it becomes light enough to lift off due to mass loss. The primary air enters the furnace through this zone and lifts the particles if the drag force is greater than gravity. The particle tracking in the bed zone is also modified to account for the longer time spent without adding unnecessary computations.

Heterogeneous reactions

The fuel particles containing water, volatiles and char are at the vaporisation temperature of the water droplets when injected thus evaporation of the water takes place during heating. The water reaches boiling point and only after it is consumed can the particle reach the vaporization temperature of the volatiles. Devolatilisation and char combustion then follows.

Heating

The fuel particle and droplet are both heated by convection and radiation through the following heat balance:

$$m_p C_p \frac{dT_p}{dt} = hA_p\left(T_\infty - T_p\right) + \varepsilon_p A_p \sigma(\theta_R^4 - T_p^4) \tag{70}$$

With

m_p = mass of particle

C_p = specific heat of particle

T_p = temperature of particle

h = convective heat transfer coefficient

A_p = surface area of particle

T_∞ = local temperature of continuous phase

ε_p = particle emissivity

σ = Stefan-Boltzmann constant

θ_R = radiation temperature, $\left(\frac{G}{4\sigma}\right)^{\frac{1}{4}}$ & $G = \int_{\Omega=4\Pi} I d\Omega$

The heat transfer coefficient, h, is based on work done by (Ranz & Marshall 1952), (Ranz & Marshall 1952):

$$Nu = \frac{h d_p}{k_\infty} = 2.0 + 0.6 Re_d^{\frac{1}{2}} Pr^{\frac{1}{3}} \quad (71)$$

With

k_∞ = thermal conductivity of the continuous phase

Pr = Prandtl number of the continuous phase $\left(\frac{C_{p\mu}}{k_\infty}\right)$

Important properties of the bagasse particles namely, specific heat, emissivity and swelling coefficient were entered as per (Gera et al. 1999). The particle density of (Bernhardt 1993) was used.

Evaporation

Since the vaporization rate of the water in this work is very high, less than a second, the effect of the convective mass transfer from the droplet to the gas (Stefan Flow) is important. The following relation based on the work of (Miller, Harstad & Bellan 1998) and (Sazhin 2006) is used:

$$\frac{dm_p}{dt} = k_c A_p \rho_\infty ln(1 + B_m) \quad (72)$$

Where

m_p = droplet mass

k_c = mass transfer coefficient

A_p = droplet surface area

ρ_∞ = density of bulk flow

k_c is calculated from the Sherwood correlation (Ranz & Marshall 1952):

$$Sh_{AB} = \frac{k_c d_p}{D_{i,m}} = 2.0 + 0.6 Re_d^{\frac{1}{2}} Sc^{\frac{1}{3}} \quad (73)$$

B_m is the Spalding mass number given by:

$$B_m = \frac{Y_{i,s} - Y_{i,\infty}}{1 - Y_{i,s}} \quad (74)$$

Where

$Y_{i,s}$ = vapour mass fraction at the surface

$Y_{i,\infty}$ = vapour mass fraction in the bulk gas

Devolatilisation

Vaporization and then boiling of the liquid content in the particles occurs at the respective temperatures consecutively. After the water is consumed, devolatilisation initiates at the vaporisation temperature of the volatiles. It remains in effect while the mass of the particle is more than the non-volatiles.

A single rate model is used with the same Arrhenius expression described in section 3.1.2., except that the temperature exponent is set to 0. Only the pre-exponential factor and activation energy is specified. The vaporisation temperature, pre-exponential factor and activation energy of the de-volatilisation reaction rate is based on the work of (Gera et al. 1999) also used by (Liu et al. 2005) for modelling bagasse.

A constant rate model based on work by (Baum & Street 1971) was also used in the initial stages of the model development:

$$-\frac{1}{f_{v,0}(1-f_{w,0})m_{p,0}}\frac{dm_p}{dt} = A_0 \quad (75)$$

With

$f_{v,0}$ = mass fraction of volatiles initially present in the particle

$f_{w,0}$ = mass fraction of evaporating/boiling material

$m_{p,0}$ = initial particle mass

m_p = particle mass

A_0 = rate constant

Char combustion

After the volatiles are consumed, surface combustion of the carbon in the particles takes place.

The diffusion-limited surface reaction rate model also derived from the model of (Baum & Street 1971) is used:

$$\frac{dm_p}{dt} = -4\pi d_p D_{i,m} \frac{Y_{OX} T_\infty \rho}{S_b(T_p + T_\infty)} \quad (76)$$

With

$D_{i,m}$ = diffusion coefficient for oxidant in the bulk

Y_{OX} = local mass fraction of oxidant in the gas

ρ = gas density

S_b = stoichiometry (char(s) + $S_b$ox(g) → products(g))

The binary diffusivity of the char was entered as a temperature dependent function as per (Gera et al. 1999). The char is oxidised to CO before reacting to form CO_2.

Coupling

As a particle is tracked through the grid, mass energy and momentum exchange takes place with the fluid as depicted in Figure 4.3.

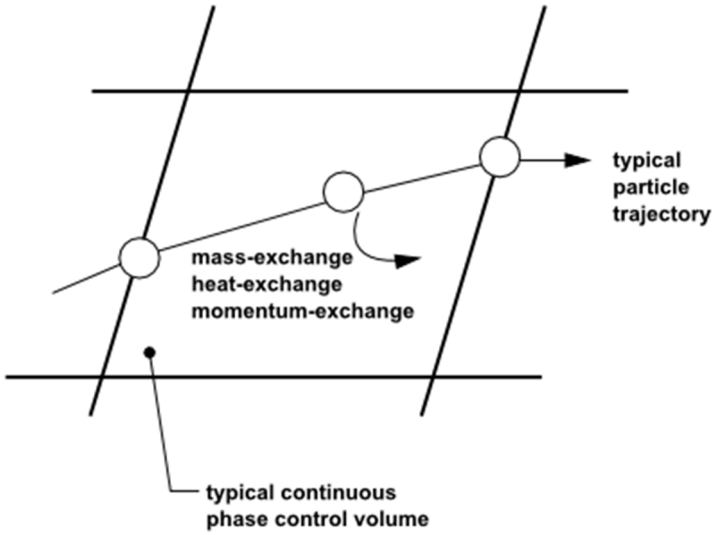

Figure 4.3: Mass, heat and momentum transfer between discrete and continuous phase (ANSYS Inc. 2013)

The mass transfer is calculated by the following:

$$M = \frac{\Delta m_p}{m_{p,0}} \dot{m_{p,0}} \quad (77)$$

M = mass transfer from discrete phase to continuous phase

Δm_p = change in mass of particle from entering to exiting control volume

In the absence of a chemical reaction (thus all processes except char combustion), the heat transfer is computed by:

$$Q = \frac{\dot{m_{p,0}}}{m_{p,0}}\left[\left(m_{p_{in}} - m_{p_{out}}\right)\left[-H_{lat_{ref}} + H_{pyrol}\right] - m_{p_{out}}\int_{T_{ref}}^{T_{p_{out}}} C_{p_p}dT + m_{p_{in}}\int_{T_{ref}}^{T_{p_{in}}} C_{p_p}dT\right] \quad (78)$$

Where

$\dot{m_{p,0}}$ = initial mass flow rate of particle injection

$m_{p,0}$ = initial mass of the particle

$m_{p_{in}}$ = mass of particle at cell entry

$m_{p_{out}}$ = mass of particle at cell exit

C_{p_p} = specific heat of particle

H_{pyrol} = heat of pyrolysis during devolatilisation

$T_{p_{in}}$ = temperature of particle at cell entry

$T_{p_{out}}$ = temperature of particle at cell exit

T_{ref} = reference temperature for enthalpy

$H_{lat_{ref}}$ = latent heat at reference conditions

During char combustion the particle heat balance is:

$$m_p C_p \frac{dT_p}{dt} = hA_p\left(T_\infty - T_p\right) - f_h \frac{dm_p}{dt} H_{reac} + A_p \varepsilon_p \sigma(\theta_R^4 - T_p^4) \quad (79)$$

f_h = fraction of heat absorbed by particle

H_{reac} = heat released by surface reaction

Momentum exchange neglecting other interaction forces is described by:

$$F = \sum\left[\frac{18\mu C_D Re}{\rho_p d_p^2 24}\left(u_p - u\right)\right]\dot{m_p}\Delta t \quad (80)$$

With

Δt = time step

4.4. Radiation

The radiative transfer equation (RTE) for a medium that is absorbing, emitting and scattering at position ***r*** in the direction ***s*** is:

$$\frac{dI(r_i,s_i)}{ds} + (a+\sigma_s)I(r_i,s_i) = an^2\frac{\sigma T^4}{\pi} + \frac{\sigma_s}{4\pi}\int_0^{4\pi} I(r_i,s_i')\emptyset(s_i.s_i')d\Omega' \quad (81)$$

With

r_i = position vector

s_i = direction vector

s_i' = scattering direction vector

s = path length

a = absorption coefficient

n = refractive index

σ_s = scattering coefficient

σ = Stefan-Boltzmann constant (5.669 x 10^{-8} W/m^{2}K^4)

I = radiation intensity depending on position (***r***), and direction (***s***)

T = local temperature

$\emptyset$ = phase function

Ω' = solid angle

Equation (81) is illustrated in Figure 4.4.

In this work the Discrete Ordinates (DO) model was used. This method solves the RTE for a finite number of discrete solid angles, each with a vector direction ***s*** in the global Cartesian system. When the effect of the particles on radiation is included, all other sources of scattering in the gas phase is neglected and the RTE is rewritten as:

$$\frac{\partial}{\partial x_i}(Is_i) + \left(a + a_p + \sigma_p\right)I(r_i,s_i) = an^2\frac{\sigma T^4}{\pi} + E_p + \frac{\sigma_p}{4\pi}\int_0^{4\pi} I(r_i,s_i')\emptyset(s_i.s_i')d\Omega' \quad (82)$$

With the following absorption, emission and scattering factors respectively due to particles

$$a_p = \lim_{V\to 0}\sum_{n=1}^{N}\varepsilon_{pn}\frac{A_{pn}}{V}$$

$$E_p = \lim_{V\to 0}\sum_{n=1}^{N}\varepsilon_{pn}A_{pn}\frac{\sigma T^4{}_{pn}}{\pi V}$$

$$\sigma_p = \lim_{V\to 0}\sum_{n=1}^{N}(1-f_{pn})(1-\varepsilon_{pn})\frac{A_{pn}}{V}$$

ε_{pn} , A_{pn} , T_{pn} is the emissivity, projected area and temperature of particle n. The summation is over N particles in volume V.

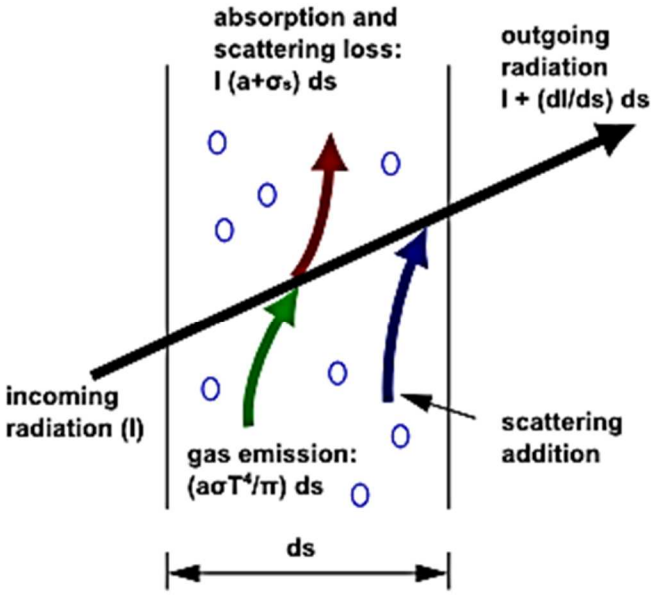

Figure 4.4: Radiative heat transfer (ANSYS Inc. 2013)

For high optical thickness cases, the DO model with second order discretisation is recommended since it covers the entire spectrum of optical thicknesses. The optical thickness is defined by the product of the absorption coefficient and the mean beam length. The characteristic absorption coefficient is typically around 1 per meter for hydrocarbon combustion and the characteristic combustor mean beam length is usually on the order of the combustion geometric scales. The maximum optical thickness of this simulation is thus considered high due to the size of the furnace. The DO model is also the most complete and accurate of the methods available in ANSYS Fluent. It accounts for gas, particle and surface radiation. (ANSYS Inc. 2013)

As mentioned before in section 3.1.4, the RTE is solved for a number of discrete solid angles and therefore the angular discretisation had to be set appropriately to 3 x 3 for theta and phi divisions defining the number of control angles used to discretize each octant of the angular space. This is considered the minimum to achieve more reliable results while maintaining lower computational cost. The theta and phi pixels were also set to 3 x 3 as recommended for problems involving symmetry.

5. Effect of hot air duct dampers on furnace symmetry

Modelling only half the boiler geometry reduces the computational expense considerably. Therefore a study to verify that the domain and physics are symmetrical about the centre line of the boiler was warranted.

When considering ideal operation of the plant, symmetry of combustion is the aim by regulating the fuel flow through the spreaders and airflow through the hot air duct dampers. Therefore it is consistent with the physical device.

Since the primary air fan is situated on the right hand side of the boiler, vanes and dampers are used to distribute the flow evenly over the airheater and grate.

In practice the flow need to be balanced between the left hand- and right hand side of the boiler with the dampers in the ducting below the grate level. These dampers are pneumatically actuated and controlled based on the air temperature and velocity measured upstream by means of venturi flow meters.

To eliminate concern that this could cause different flow patterns comparing the left and right hand underside of the grate, a separate sub model was run to study the effect of the dampers (see Figure 5.1).

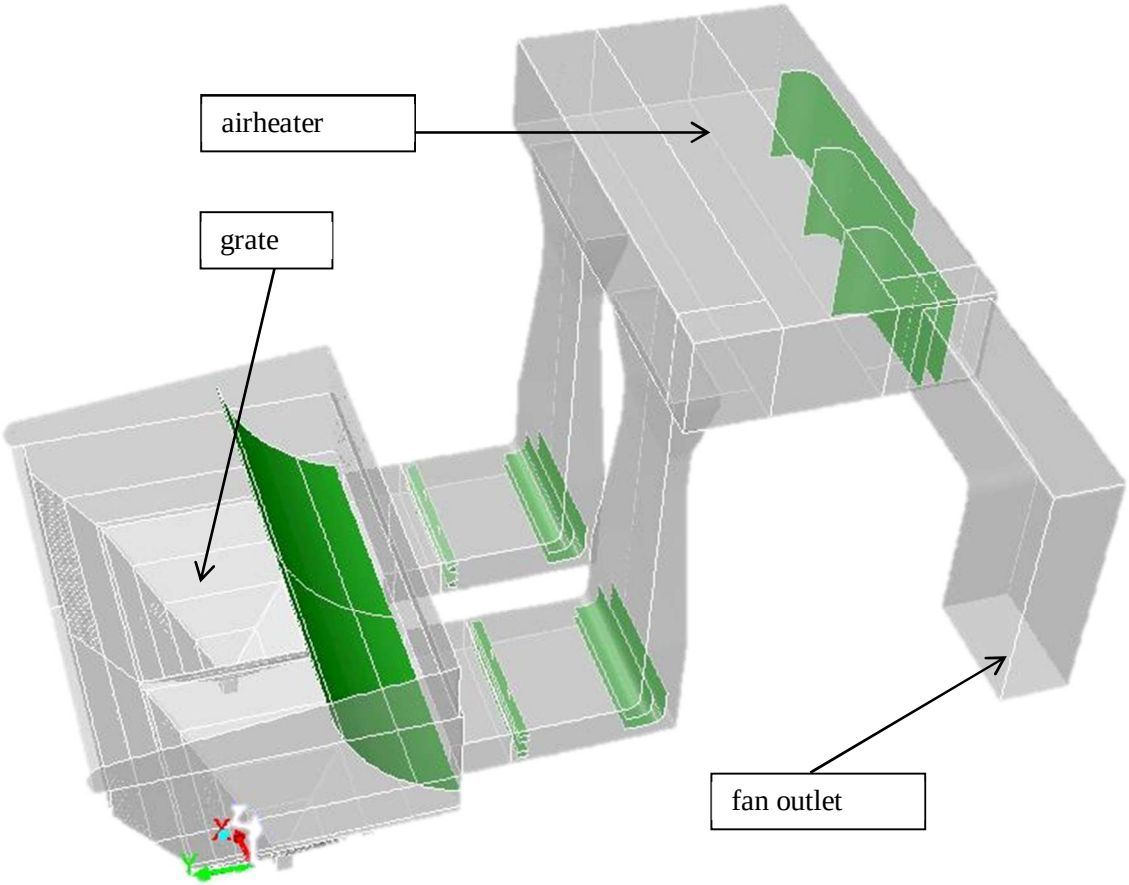

Figure 5.1: Sub model of primary air system

From the results in Figure 5.2 it was concluded that the velocity profile underneath the grate is symmetrical and therefore only half of the boiler need to be modelled.

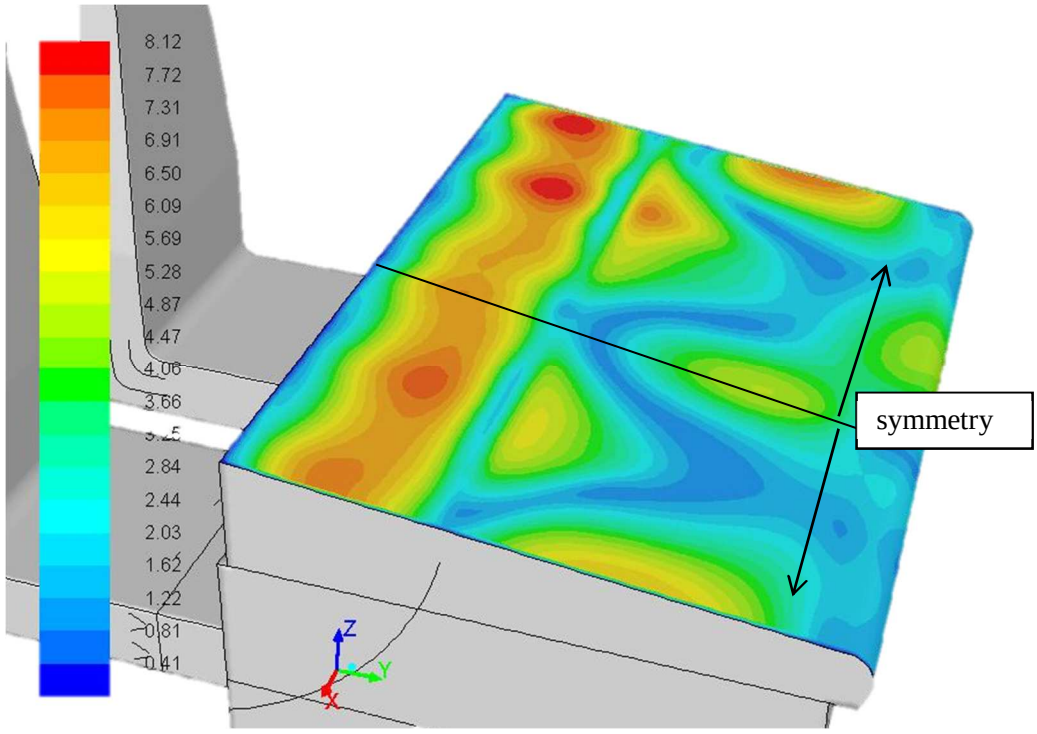

Figure 5.2: Contours of velocity magnitude underneath the grate in m/s

6. Sensitivity of combustion modelling parameters and effect on heat transfer

The influence of the following model parameters on the results of combustion was studied:

- Fuel particle size grading and shape factor
- Water droplet heat transfer model
- Devolatilisation model and parameters
- Char combustion model and binary diffusivity
- Volatile kinetic rate and constants of (Magnussen & Hjertager 1976)
- CO kinetic rate and constants of (Magnussen & Hjertager 1976)
- Turbulence model

The mesh used for the combustion study is shown in Figure 6.1. Grid independency with regards to the variables monitored in the study was achieved for this mesh of 2.5 million cells using 54000 discrete phase particles.

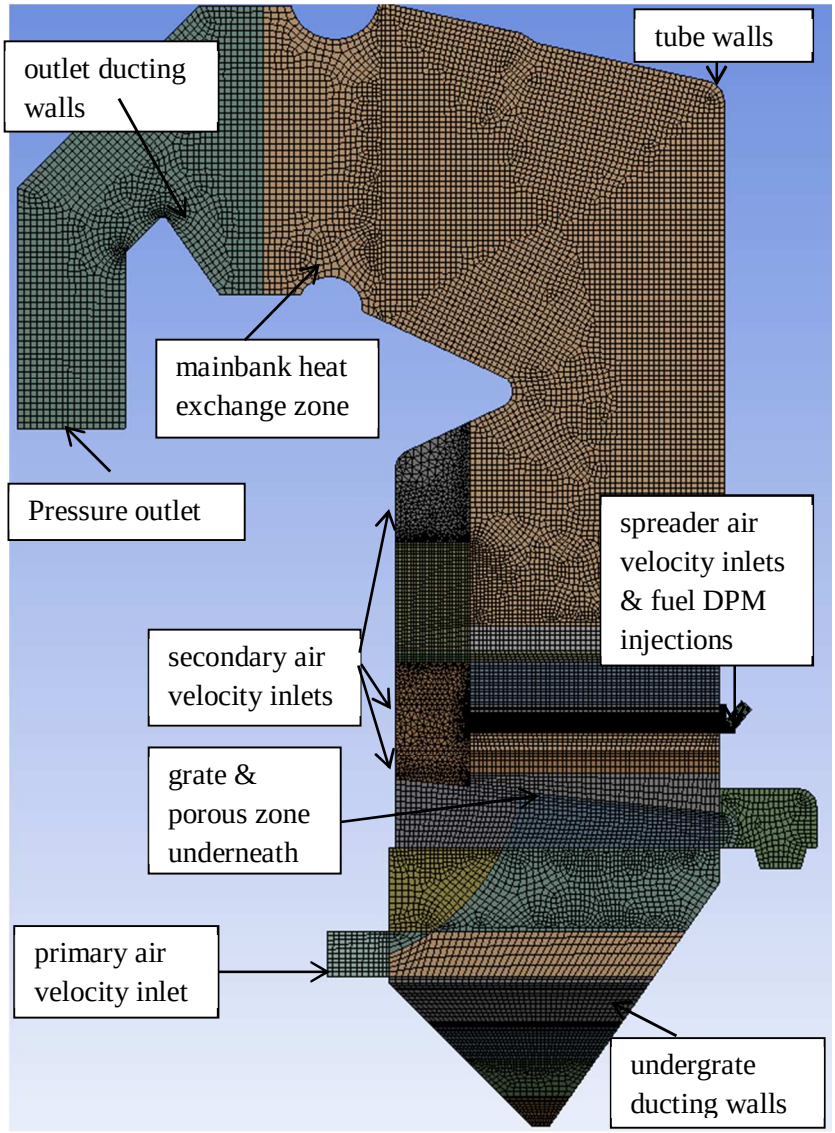

Figure 6.1: Mesh used for study on combustion

Contour plots or particle tracks are shown to illustrate the effect of each parameter. In displaying the results, the final model with the more accurate settings is always displayed on the left hand side and the model with a different parameter setting on the right. All contour plots were reported on the symmetry plane in the middle of the boiler.

The objective of this study was to identify the parameters that have the largest impact on combustion and related heat transfer to the superheater. The more accurate settings of these parameters were then determined by visual inspection of the model results and compared to measurements made and images captured during tests on the boiler, as discussed in Chapter 10.

The results were also discussed internally at John Thompson to verify that it corresponds with practical experience.

Fuel particle size grading and shape factor

The particle size grading of bagasse from 3 different sources were analysed, namely (Naude, McIntyre & Field 1993) from John Thompson, (Rainey et al. 2012) of the SRI in Australia and (Bernhardt 1993) of the Sugar Milling Research Institute in Durban. The grading of (Naude, McIntyre & Field 1993) was found to be the finest and the grading of (Bernhardt 1993) the coarsest. Therefore these two extremes were used in the simulations.

The grading of (Naude, McIntyre & Field 1993) resulted in too many particles in suspension compared to actual conditions. The grading of (Bernhardt 1993) resulted in a 70: 30 split between suspension and grate firing in line with actual conditions (see Figure 6.2 comparing the particle tracks). The coarser size grading results are presented on the left hand side.

The net result on combustion was a more concentrated temperature distribution lower down in the boiler resulting in more heat transfer to the furnace for the coarser size grading. There was also more combustion occurring at the rear on grate level not seen with the fine grading (see Figure 6.3 comparing the temperature contours). The coarser size grading is on the left hand side.

(Bernhardt 1993) used diffuser bagasse in his measurements which is the same bagasse preparation at TSB Komati mill. Since the particle behaviour of this grading in the simulation was more realistic it was chosen for the final model setting.

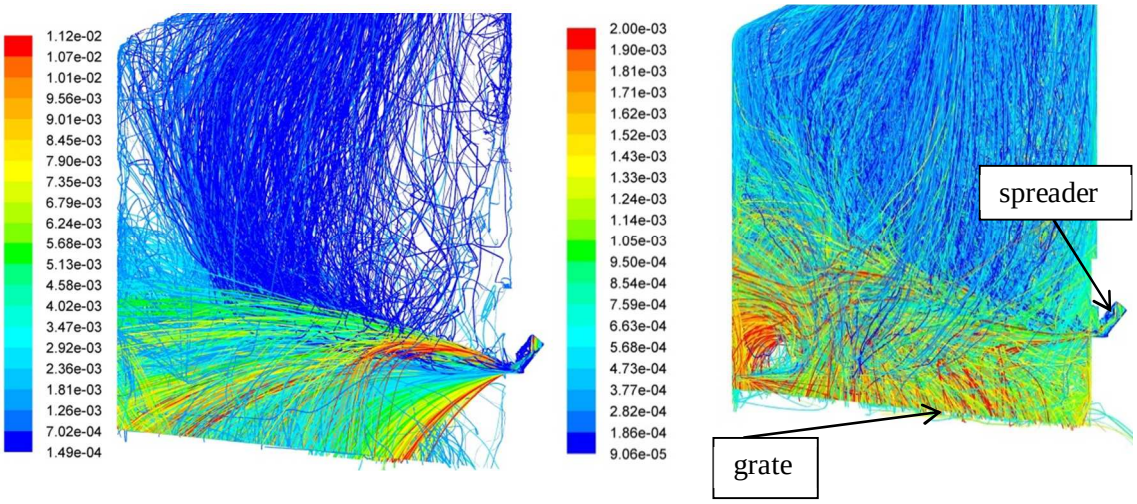

Figure 6.2: Particle tracks to illustrate the effect of particle size distribution, sizing in meters

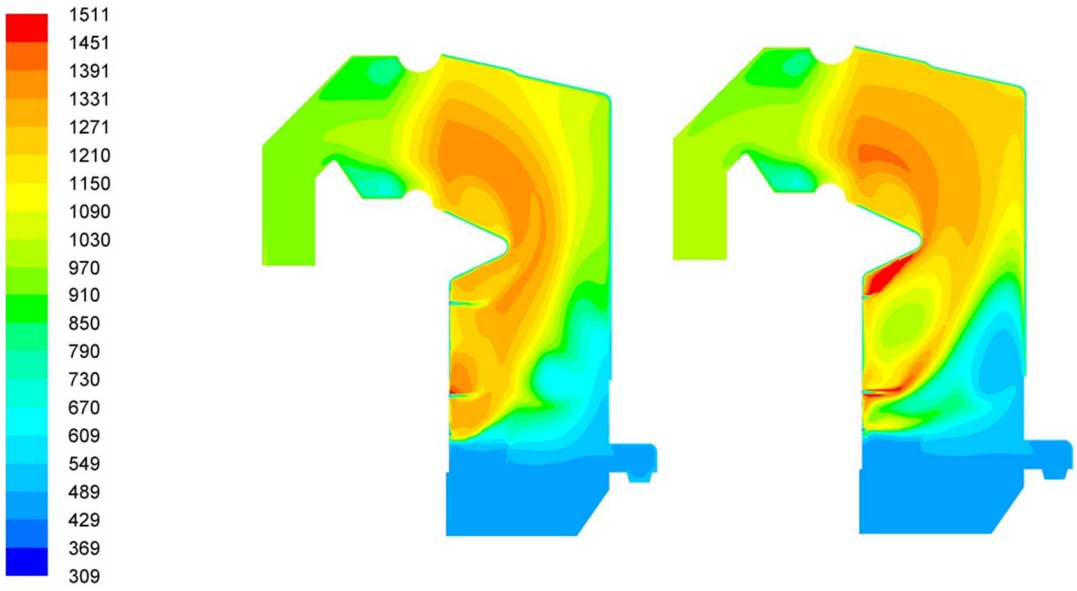

Figure 6.3: Temperature contours in Kelvin to illustrate the effect of particle size distribution

The sensitivity of the results from the model to particle shape factor was tested by changing the shape factor to spherical. As can be seen on the right hand side of Figure 6.4, the spread of the particles changed significantly. The lower drag resulted in more particles on the grate. The bulk of the spread was also closer to the front of the boiler.

The change in spread resulted in more concentrated energy lower down in the furnace and closer to the front wall. The overall temperature was also higher. Refer to the right hand side of Figure 6.5.

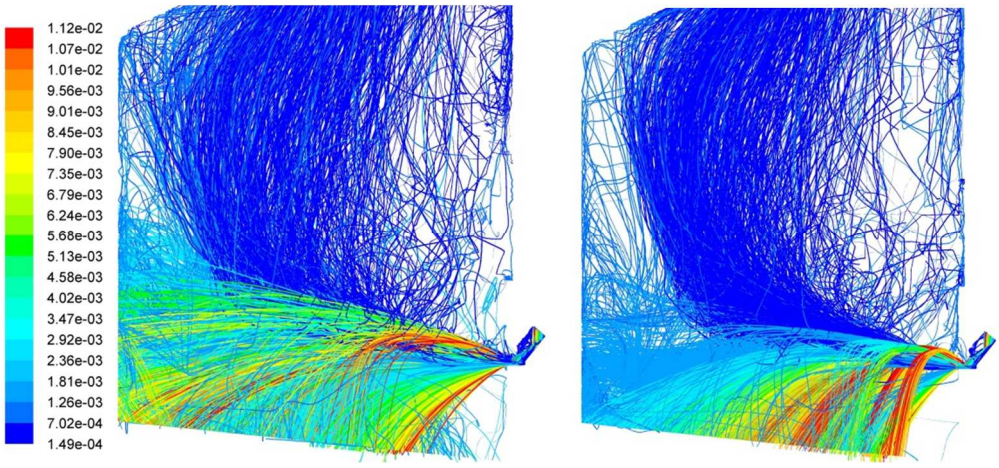

Figure 6.4: Particle tracks to illustrate the effect of particle shape factor, sizing in m

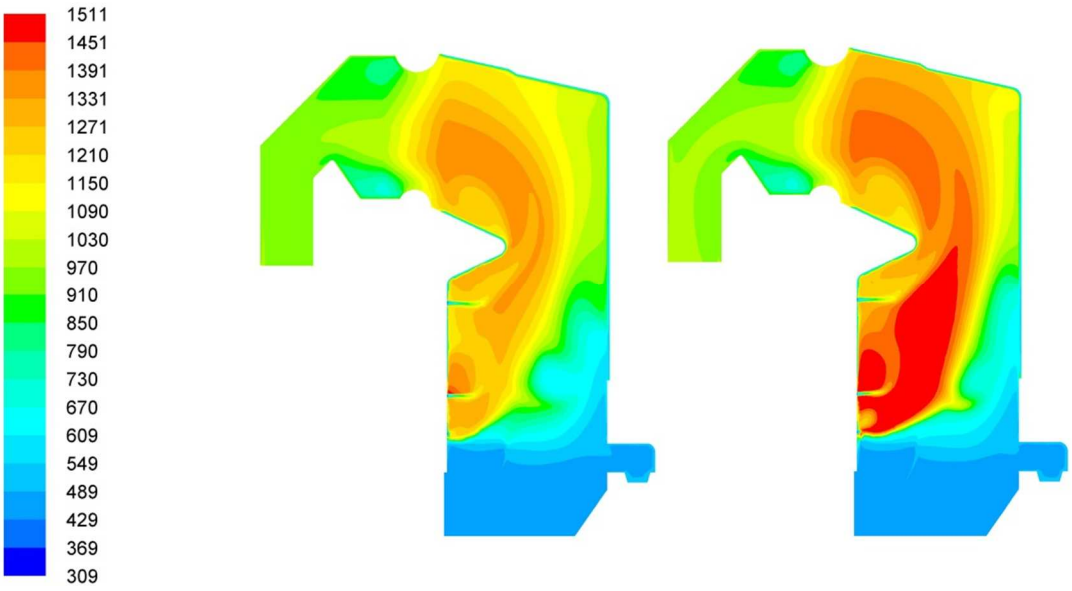

Figure 6.5: Temperature contours in Kelvin to illustrate the effect of particle shape factor

Water droplet heat transfer model

Half of bagasse consists of water and modelling of the water droplet is thus very important. Initially only diffusion heat transfer was considered in the water vaporisation model. The resulting temperature profiles showed a higher concentration of energy released lower down closer to the rear of the boiler (see the right hand side of Figure 6.6).

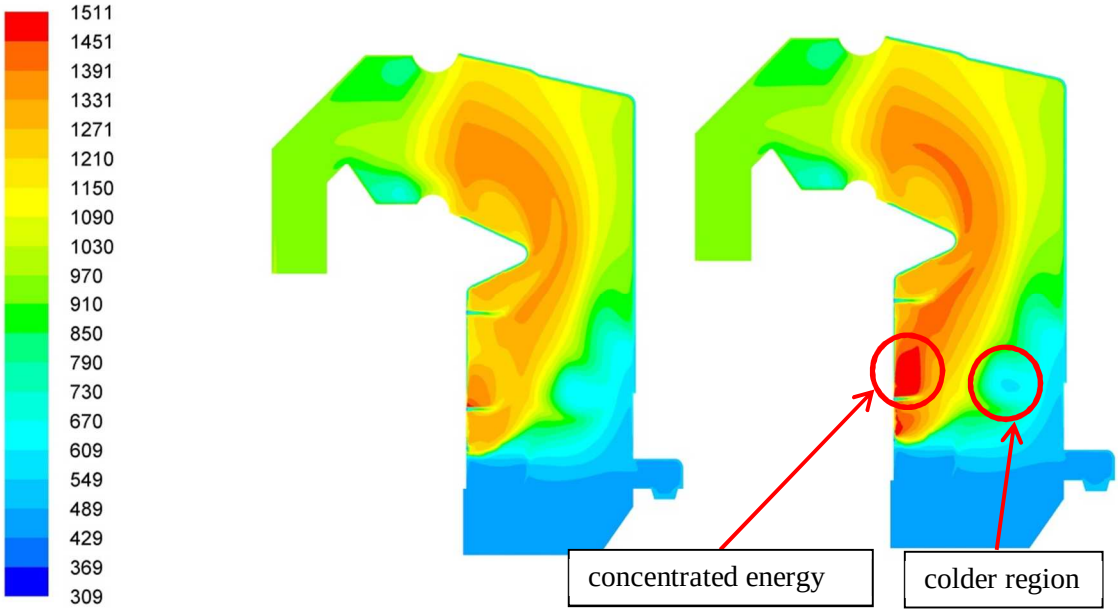

Figure 6.6: Temperature contours in kelvin to show the effect of water vaporization heat transfer

From these results it was concluded that the bagasse dried out slower, decelerating the onset of combustion. Therefore a higher concentration of water evaporated close to the rear wall (see the right hand side of Figure 6.7).

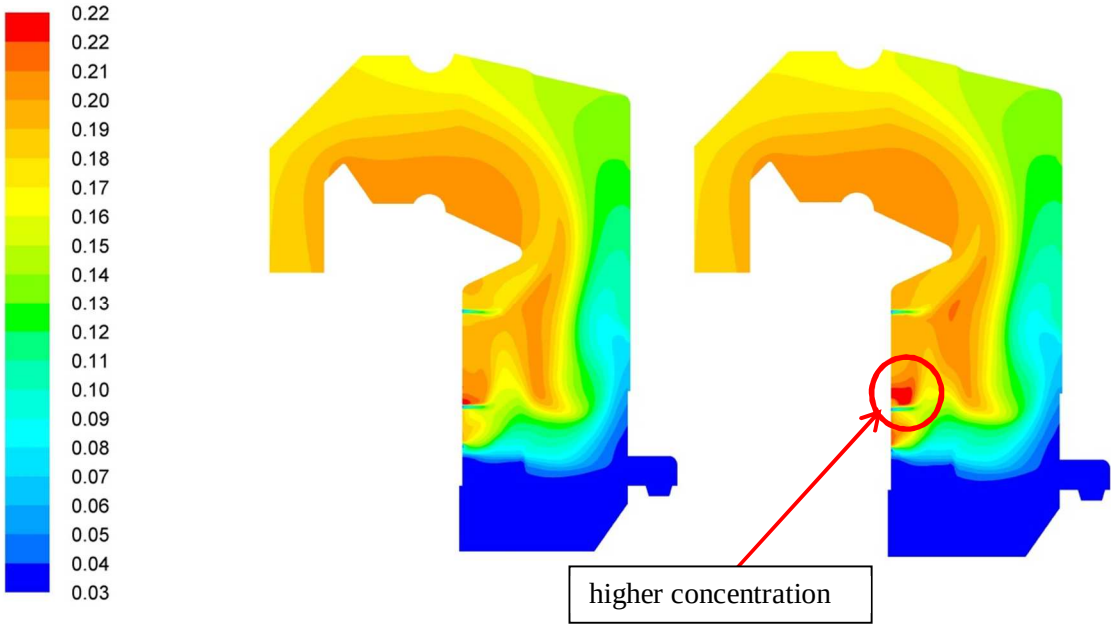

Figure 6.7: Water species mass fraction contours to illustrate the effect of water vaporization heat transfer model

The delay in combustion can also be seen as a colder spot at the front of the furnace on the right hand side of Figure 6.6 for the model considering diffusion only.

Since the vaporisation rate of the water in the boiler is very high, convection heat transfer need to be considered as recommended by (Miller, Harstad & Bellan 1998) and (Sazhin 2006). Therefore it was implemented as described by equation (72) in Chapter 4 for the final model settings. The results can be seen on the left hand side of Figures 6.6 and 6.7 indicating less combustion intensity close to the rearwall.

Devolatilisation model and parameters

A constant devolatilisation rate was used based on the work of (Baum & Street 1971). Since the onset of devolatilisation occurs at a set temperature and a constant value, the volatiles distributes more evenly in the lower volume of the furnace (see the right hand side of Figure 6.8).

This affects the combustion and temperature profiles directly with a diffusive characteristic, similar to first order discretisation. See Figure 6.9, where a more uniform temperature distribution is shown close to the front wall of the boiler on the right hand side with a constant devolatilisation rate.

The contours of the final model settings on the left hand side show a cold spot in this area using a devolatilisation rate of the Arrhenius form. Although the constant rate approach increases numerical stability and accelerates convergence, it is not realistic since the devolatilisation has been proven to be temperature dependent for all fuels.

However the results achieved using a constant rate compared to the rate of the Arrhenius form were close to the temperature measurements on the gas and steam side discussed in Chapter 10.

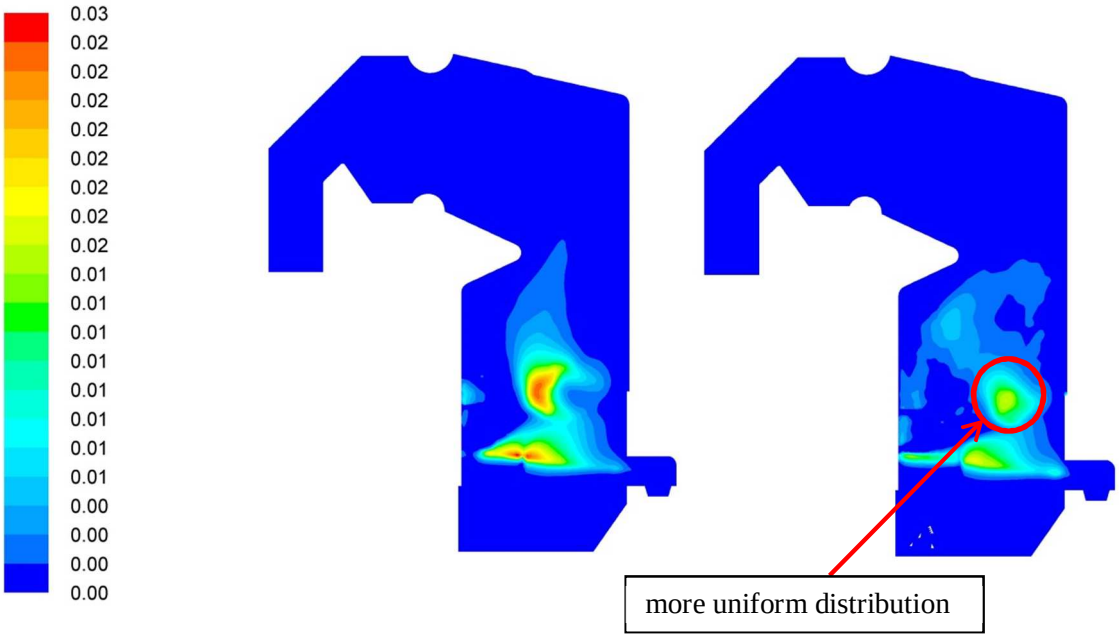

Figure 6.8: Volatile species mass fraction contours to illustrate the effect of a constant devolatilisation rate

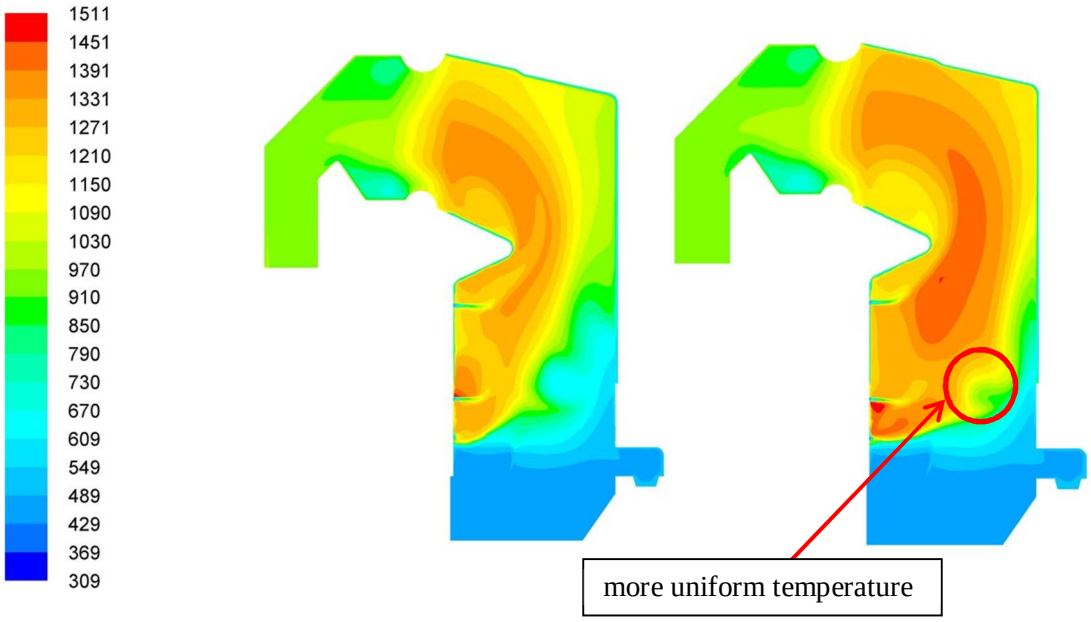

Figure 6.9: Temperature contours in Kelvin to illustrate the effect of constant devolatilisation rate

A single rate devolatilisation approach of the Arrhenius form delivered more concentrated temperature profiles than the constant rate. Rates from three different publications were investigated namely (Gera et al. 1999), (Drummond & Drummond 1996) and (Stubington & Aiman 1994) in order from fastest to slowest rate.

The rate of (Gera et al. 1999) produced concentrated combustion lower down in the furnace and closer to the rear wall. The temperature peak was also the highest of the rates implemented.

The rates of (Drummond & Drummond 1996) and (Stubington & Aiman 1994) delivered a cold region in most of the lower furnace volume. Combustion was delayed, resulting in a higher

temperature concentration on the rear wall and more combustion higher up in the furnace into the superheater. These were the initial effects on the simulation, but as the model converged the combustion extinguished completely in the furnace. Energy was only released after the mainbank, which is totally unrealistic.

See Figures 6.10 and 6.11 illustrating the effect of the rate of (Gera et al. 1999) on the left and (Stubington & Aiman 1994) on the right hand side.

The difference between these rates is that (Gera et al. 1999) determined the pre-exponential factor and activation energy in a pilot plant and the other two authors with TGA tests. Since only the rate of (Gera et al. 1999) produced realistic results, it was concluded that the model combinations in ANSYS® Fluent for bagasse firing require pilot plant testing and modelling rather than TGA testing to determine devolatilisation rates.

The authors from the SRI that used the TGA rates implemented it in FURNACE as mentioned in Chapter 2. The resultant temperature contours of these authors were close to the TSB Komati results using ANSYS® Fluent with the rate of (Gera et al. 1999).

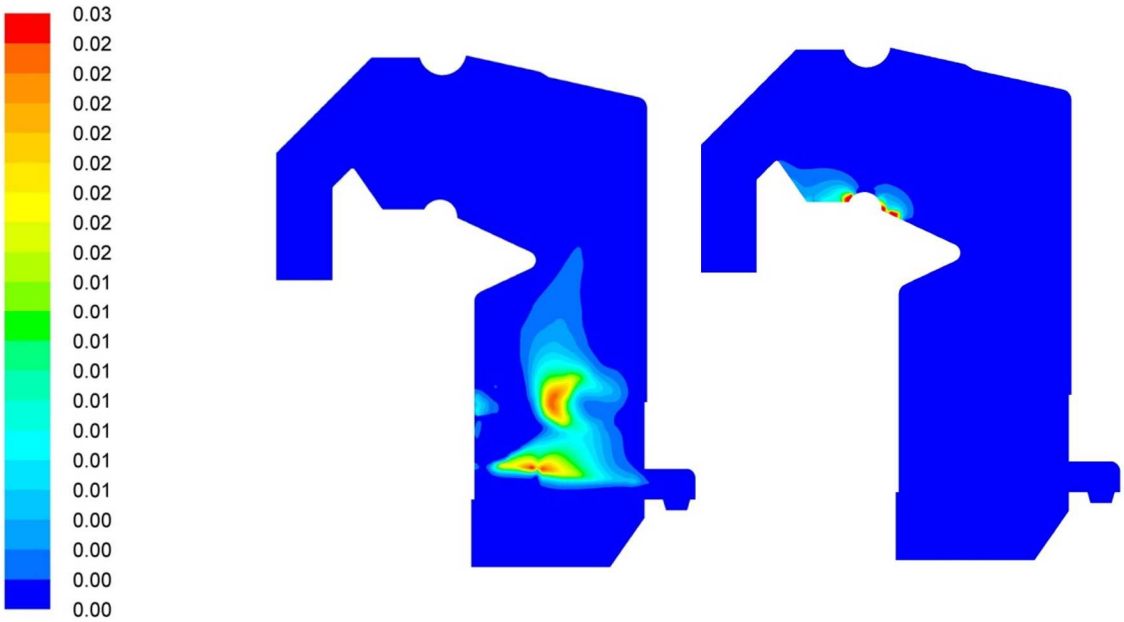

Figure 6.10: Volatile species mass fraction contours to illustrate the effect of devolatilisation rate as determined by (Stubington & Aiman 1994)

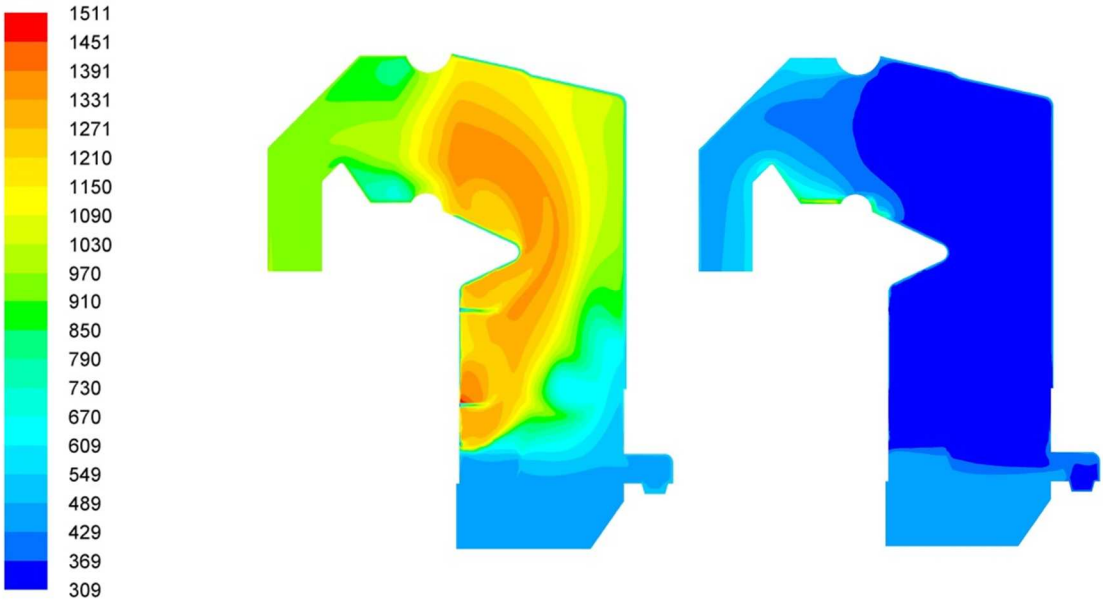

Figure 6.11: Temperature contours in Kelvin to illustrate the effect of devolatilisation rate as determined by (Stubington & Aiman 1994)

(Shanmukharadhya 2007), (Shanmukharadhya & Sudhakar 2007), (Shanmukharadhya & Sudhakar 2008) and (Shanmukharadhya & Sudhakar 2007) used the rates determined by TGA testing in FLUENT, but for a completely different combustion system utilising tangential over fire air and the results are therefore not comparable. The rate of (Gera et al. 1999) was chosen for the final model settings.

Char combustion model and binary diffusivity

Since a diffusion limited char combustion model was used as described in Chapter 4, it was very sensitive to the binary diffusivity of the bagasse particle. See equation (53) in Chapter 4.

A temperature dependent function for the binary diffusivity from (Gera et al. 1999) produced higher char combustion than using a constant rate from (de Souza-Santos 2004). The char conversion was 96.6 % and 89.5% respectively. This increased the energy released in the combustion gas with higher absolute value temperature profiles. Since the carbon loss measured for bagasse firing is 3 % on average, the binary diffusivity of (Gera et al. 1999) was chosen for the final model settings.

Volatile kinetic rate and constants of (Magnussen & Hjertager 1976)

A high number of studies are concerned with the kinetics of reactions related to combustion. The modeller therefore has various choices and (de Souza-Santos 2004) recommends the following steps:

1) Find the range of temperature, pressure and concentrations of reactants at which the kinetics was determined to check compatibility.
2) Study the methodology of the experiments.
3) Compare the various rates at the conditions in question. Deviations of 50 % are common. It is also reasonable practice to choose a rate around the average.

Volatile kinetic rates used by two authors for biomass combustion modelling with ANSYS® Fluent were investigated, namely (Yin et al. 2009) and (Miltner et al. 2006). Only the rate of (Yin et al. 2009) was found suitable for the setup of the Komati model since a two-step global mechanism was used. (Miltner et al. 2006) included more reactions necessary for NO_x formation modelling.

The rate of (Yin et al. 2009) was implemented to check the sensitivity of the volatile kinetic rate on the results of the simulation. The combustion was delayed with a temperature concentration on the rear wall of the boiler, similar to the effect of the devolatilisation rates determined by TGA tests. After subsequent iterations the same effect as in Figures 6.7 and 6.8 were seen. Therefore the final model settings were adjusted to mixing-limited for the volatile chemical reaction. It was concluded that pilot plant testing is required to determine the volatile kinetic rate of bagasse in the boiler.

For biomass the “mixed-is-burnt” approach is a reasonable assumption (Turns 2011). (Scharler, Fleckl & Obernberger 2003) also assumed fast kinetics for the volatile reaction used in the modelling of a biomass grate furnace. Since the reaction was set to mixing limited it is very sensitive to the constants of (Magnussen & Hjertager 1976). See Chapter 4 for the description of the Eddy-Dissipation turbulence chemistry interaction model based on the work of (Magnussen & Hjertager 1976) and (Spalding 1970). Equations (42) and (43) illustrate the A and B constants.

Setting these parameters faster concentrated the combustion at higher temperatures lower down in the furnace with the opposite effect at slower values. The most realistic temperature profiles compared to the measurements discussed in Chapter 10 were achieved at the values for the constants determined by (Magnussen & Hjertager 1976) for pulverised coal. These were the final model settings of 4 and 0.5 for the A and B constant respectively.

CO kinetic rate and constants of (Magnussen & Hjertager 1976)

The same procedure recommended by (de Souza-Santos 2004) and discussed for the volatile kinetic rate was followed for the CO kinetic reaction. Rates from Hottel, Howard, Dryer, Yetter and Villienski from (de Souza-Santos 2004) were compared. The rate of (Dryer 1972) was used by (Yin et al. 2009) to model a biomass pilot plant. The rate of (Howard, Williams & Fine 1973) was used by (Scharler, Fleckl & Obernberger 2003) to model a grate fired biomass furnace. Therefore these two rates were implemented in the Komati model and best results were achieved with the rate of (Howard, Williams & Fine 1973).

The rate of (Howard, Williams & Fine 1973) correlates well when extrapolated over the temperature range and compared with various other authors as per Figure 6.12 from (Howard, Williams & Fine 1973).

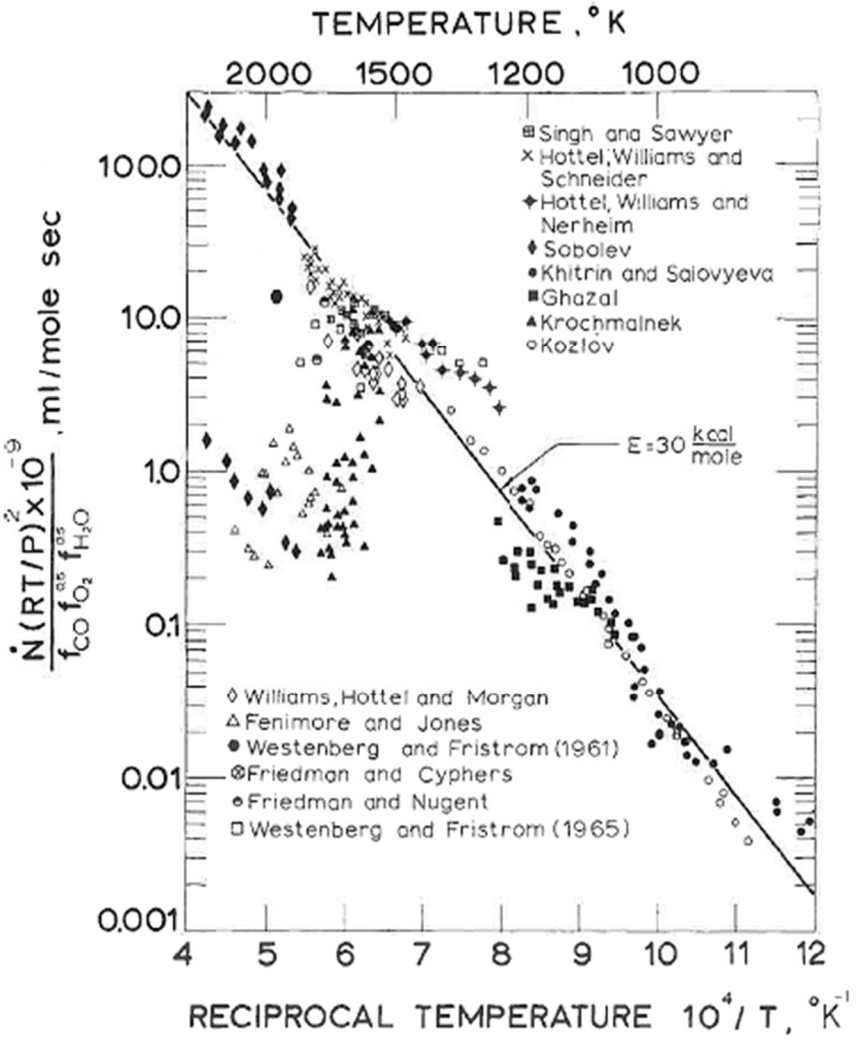

Figure 6.12: Comparison of CO kinetic rates of various authors, (Howard, Williams & Fine 1973)

It also follows the mean of the rates compared from (de Souza-Santos 2004) and was thus chosen for the final model settings. When this CO kinetic rate was implemented on the Komati model the results indicated a high sensitivity of the simulation to this parameter.

On the right hand side of Figures 6.13 and 6.14 it can be seen that a similar effect than using a constant devolatilisation rate is achieved when the CO reaction rate is set to mixing-limited, but the effect is less pronounced.

The combustion is more uniform in the lower furnace volume. The most noticeable difference is that the cold spot visible on the left hand side with the CO kinetics is not visible on the right with the mixing limited model. Figure 6.13 also indicates reduced combustion in this area for the final model settings with a CO kinetic rate.

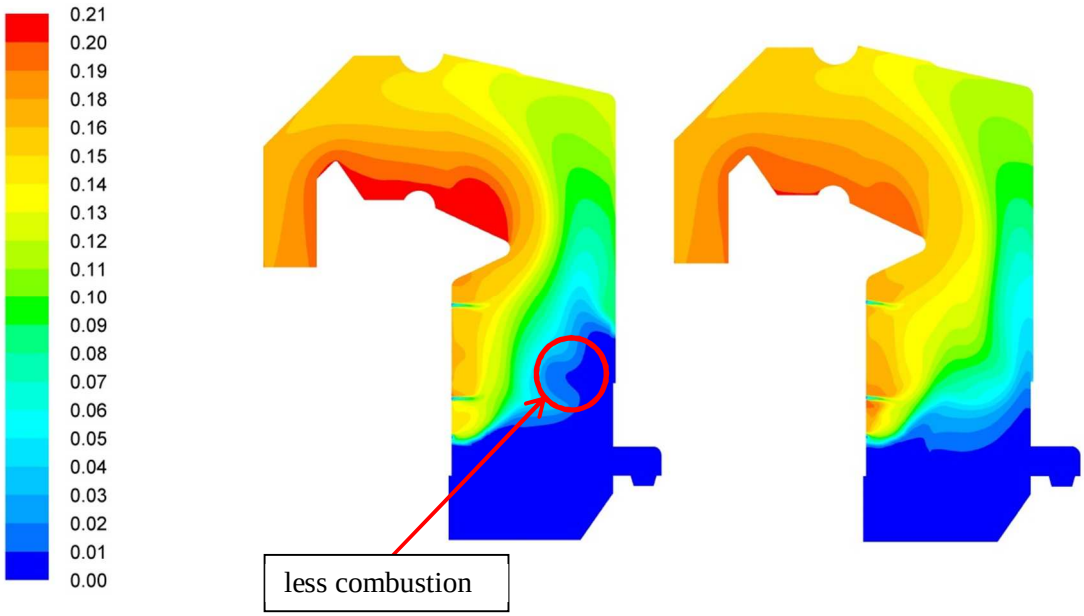

Figure 6.13: CO_2 species mass fraction contours to illustrate the effect of CO kinetic rate

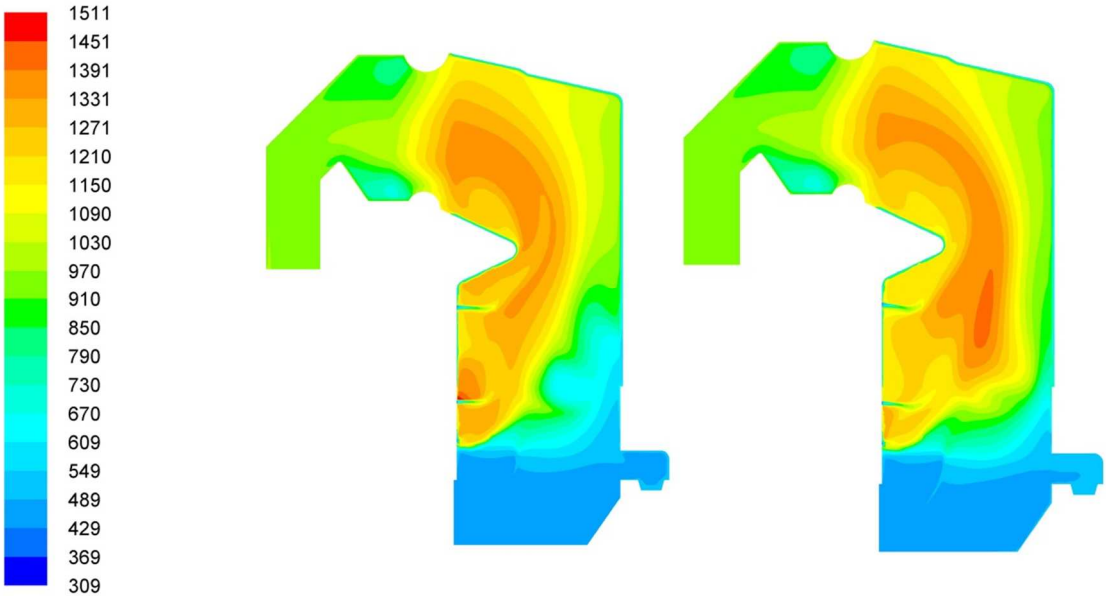

Figure 6.14: Temperature contours in Kelvin to illustrate the effect of CO kinetic rate

It was determined that the constants of (Magnussen & Hjertager 1976) have an even larger effect on the model results. Adjusting the constants to the values as determined by (Magnussen & Hjertager 1976) for pulverised coal (A = 4 & B = 0.5), increased the concentration of combustion and temperature lower down in the furnace (see the right hand side of Figures 6.15 and 6.16).

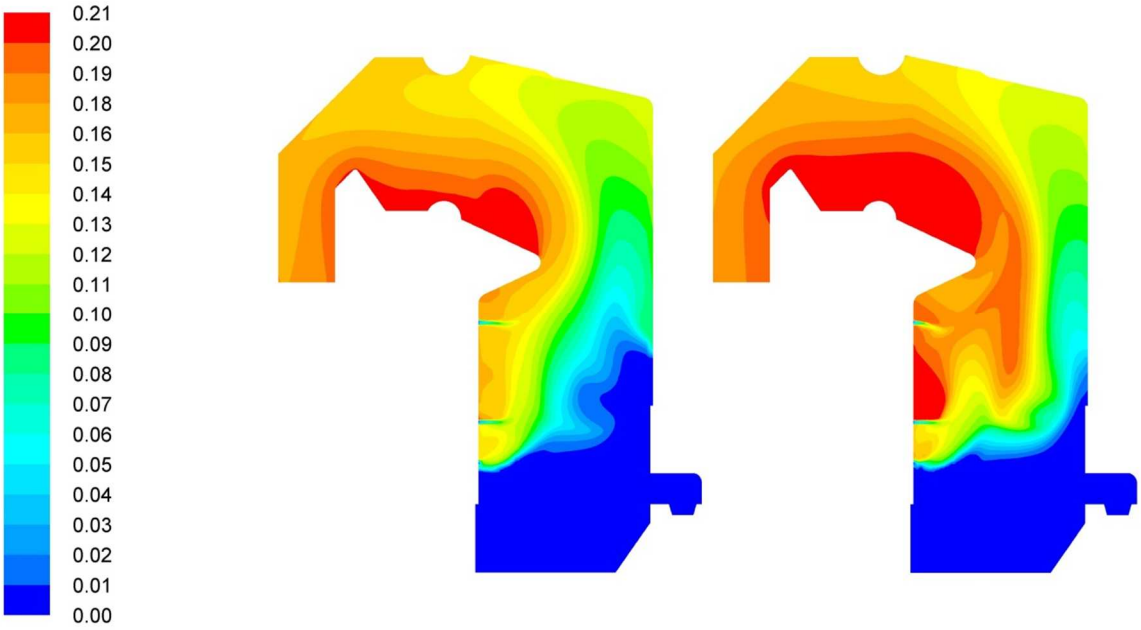

Figure 6.15: CO_2 species mass fraction contours to illustrate the effect of the constants determined by (Magnussen & Hjertager 1976) for the CO reaction rate

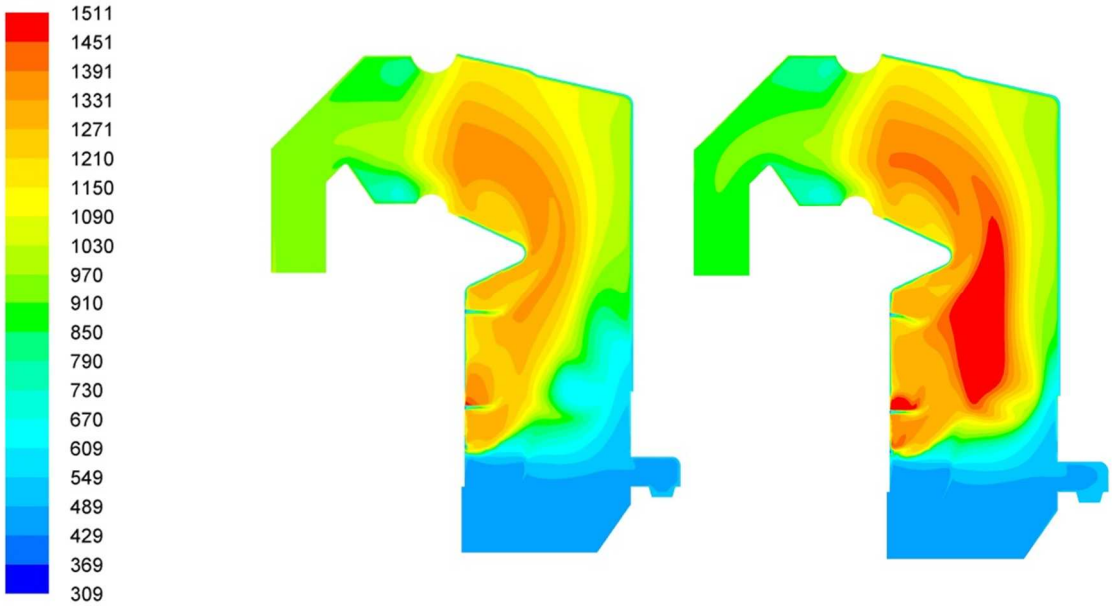

Figure 6.16: Temperature contours in Kelvin to illustrate the effect of the constants determined by (Magnussen & Hjertager 1976) for the CO reaction rate

However the CO profiles were not realistic compared to the measured values after the superheater. These measurements are shown in Figure 10.10 of Chapter 10.

Therefore adjustments were made to these constants as recommended by (Scharler, Fleckl & Obernberger 2003). The A constant was set to 0.6 and the B constant to 1e+20.

These settings delivered realistic CO and temperature profiles compared to the measurements discussed in Chapter 10. It was therefore chosen for the final model settings. See the left hand side of Figures 6.15 and 6.16 for the results.

Turbulence model

Three different turbulence models were tested namely, standard k-ε, realizable k-ε and the LRN model of (Chang, Hsieh & Chen 1995). The results using standard k-ε was similar than using the model of (Chang, Hsieh & Chen 1995).

The realizable k-ε model predicted a similar effect than using a constant devolatilisation rate or a mixing-limited CO kinetic rate, but it was more pronounced. More combustion was seen lower down in the furnace and closer to the front wall (see Figure 6.17). The results from the LRN model are on the left and realizable k-ε on the right.

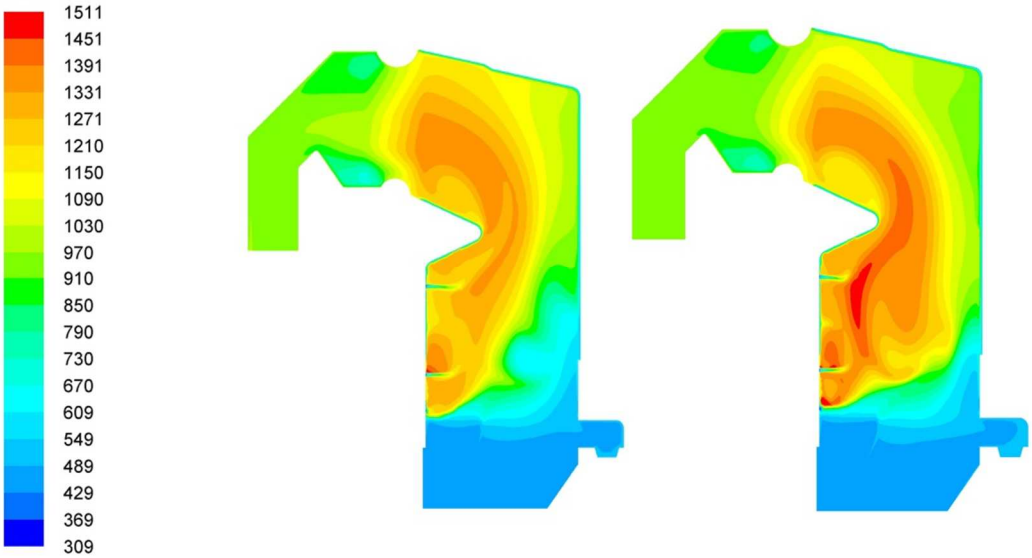

Figure 6.17: Temperature contours in kelvin to illustrate the effect of Realizable k-ε turbulence model

The realizable k-ε model was expected to produce different results than the other two turbulence models since it is the only approach preventing the normal Reynolds stress from becoming negative at high velocity gradients and violation of the Schwarz inequality, as discussed in Chapter 4. The difference in turbulence intensity can be seen in Figure 6.18 with the results of realizable k-ε on the right hand side.

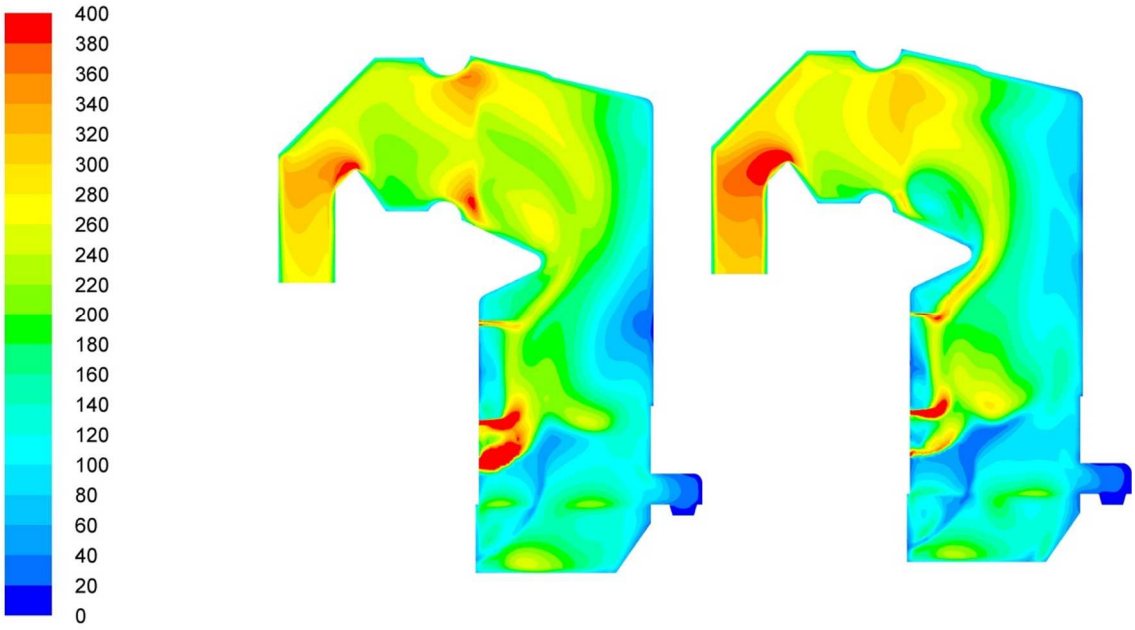

Figure 6.18: Turbulence intensity contours to illustrate the effect of Realizable k-ε turbulence model

The LRN turbulence model of (Chang, Hsieh & Chen 1995) was chosen for the final model settings due to reasons explained in Chapter 7.

Conclusions from investigating the effect of model parameters on combustion

The effects discussed were tested on the mesh including the superheater. From this investigation it can be concluded that the combustion has a major effect on the heat transfer to the superheater if the modelling parameters are producing unrealistic results e.g.:

- A devolatilisation rate that is too slow increases the steam temperature due to more combustion in the superheater region, unless the flame is extinguished.
- A char binary diffusivity that is too low leads to incomplete combustion and decreases the steam temperature, since less energy is released from the fuel.
- A volatile or CO kinetic rate that is too slow increases the steam temperature due to combustion in the superheater, unless the flame is extinguished.
- A volatile or CO mixing rate that is too slow increases the steam temperature due to combustion in the superheater, unless the flame is extinguished. If the rate is too fast it decreases the steam temperature, since more heat is absorbed in the furnace from the increase in combustion intensity lower down in the boiler.

However when these parameters are selected or adjusted based on applicable published values, realistic effects is achieved comparing the results of the simulation to site measurements.

The turbulence model, devolatilisation rate and CO kinetic rate warrants further investigation if the current model is to be used to investigate combustion related phenomena lower down in the furnace. A higher level turbulence model could be used to check for inaccuracies due to anisotropic turbulent effects, e.g. the Reynolds Stress Model. Devolatilisation rates from pilot plant testing can be investigated. A CO kinetic rate validated at lower temperatures (from 500 K to 1000 K) can also be considered. These model changes have to be validated with tests on the boiler lower down in the furnace.

7. Validation of modelling techniques for tube bank convection heat transfer

The focus of this thesis is the heat transfer to the superheater. The metal of the superheater tubes is heated by radiation and convection on the outside surface. Conduction transports the energy through the metal to the inside of the tubes where the steam is heated by radiation and convection.

Of these modes of heat transfer, convection plays the largest role and therefore a study was conducted to verify the accuracy of the CFD results with regards to convective heat transfer using different grids and turbulence models.

The geometry of published tube bank experiments by (Murray 1993) and (Zukauskas 1972) were used since the experimental data is available to compare to the CFD results. The geometry of the TSB Komati tube bank was also simulated, because the tube size and pitch differed quite substantially from the published experiments. Calculations according to the VDI Warmte Atlas (Stephan 2010) using the empirical correlations of (Gnielinski 1979) were performed for the TSB Komati geometry to compare to the CFD results and also for the other geometries as added verification.

2D simulations were performed since the flow was straightened at an angle perpendicular to the tube axis at the inlet of the tube banks in the experiments. The empirical correlations of (Gnielinski 1979) were also determined for the same angular flow conditions.

Wall functions, a two layer method and LRN models were used with all the geometries studied. The accuracy with regards to pressure drop was also compared against experimental results. The goal of this study was to establish a mesh resolution and turbulence model that could be used to accurately predict convection heat transfer in isolation from the other complex combustion phenomena inside the boiler. Computational expense had to be kept to a minimum.

In this body of work the heat transfer to the tube bank in the TSB Komati boiler is investigated. The simulations of the published experiments of (Murray 1993) and (Zukauskas 1972) were performed to verify the consistency of the results with different geometries and are therefore included only as background information in Appendix C.

TSB Komati Superheater

The same tube bank geometry as the Komati boiler model was simulated in 2D plan view. The tube size, transversal tube pitch and longitudinal tube pitch was identical. The mesh resolution shown in Figure 7.1 is the final choice.

Ambient air flows over the tube bank and a constant tube surface temperature of 100°C was modelled. These conditions differ from what the boiler tube bank is exposed to, but are typical conditions in tube bank experiments for which the empirical correlations of (Gnielinski 1979) are valid. Effects such as radiation heat transfer and chemical reactions in boundary layers are avoided.

From the lumped parameter model of Komati, Appendix B, the average Reynolds number is 4000 for the tube bank in the boiler simulation at full load. Thus the Reynolds number range from 1000 to 10000 was chosen for the evaluation in order to cater for variations in the flow field and future simulations of slightly different geometries or boiler loads. The velocity at the inlet of the 2D simulations was varied to determine data points for this Reynolds number range.

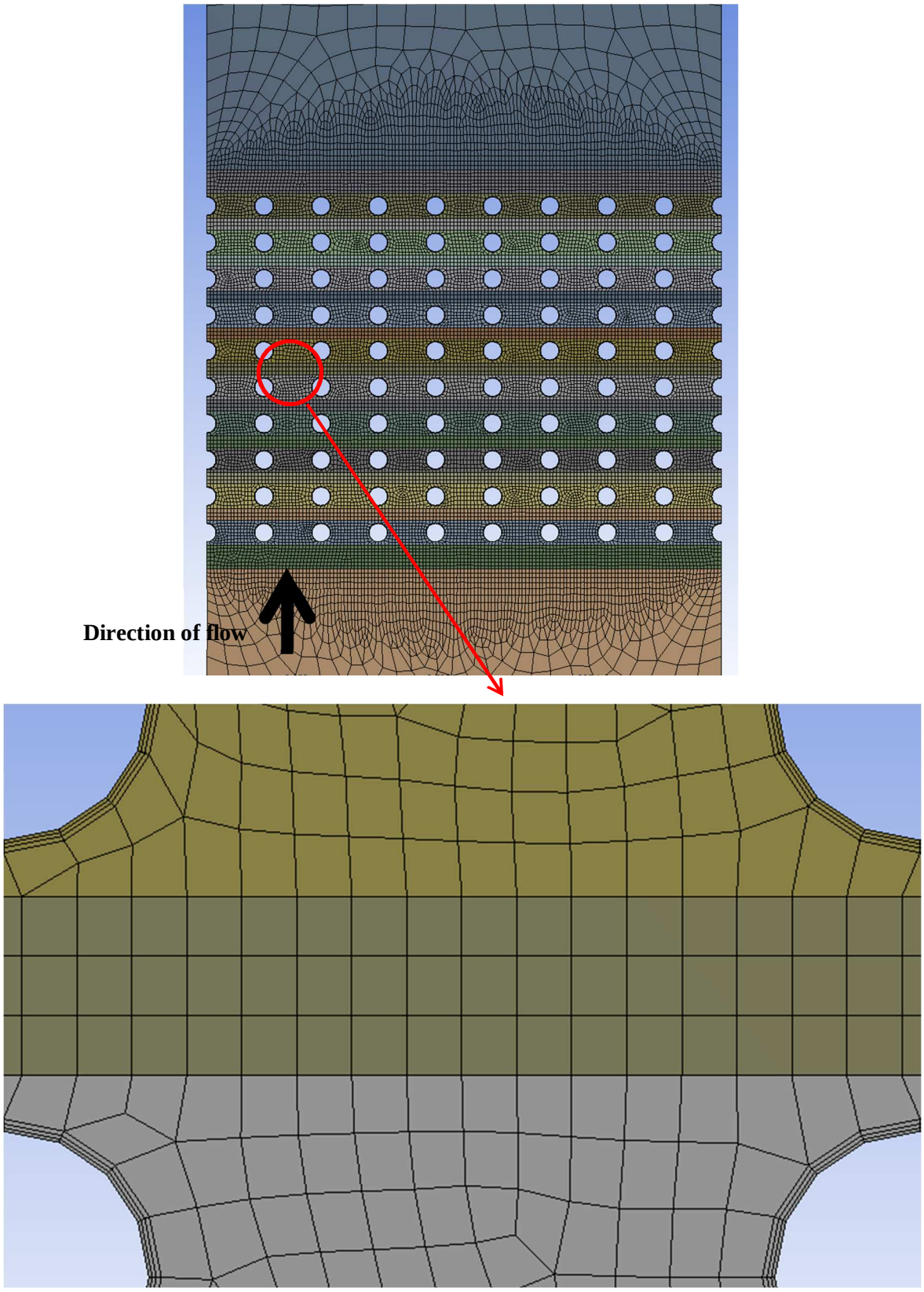

Figure 7.1: 2D mesh used for TSB Komati simulations with 50.8 x 200 x 127 mm for the tube diameter, transversal pitch and longitudinal pitch

7.1. Wall functions

The numerically determined heat transfer values for Komati using different wall function formulations were compared to the empirical correlations of (Zukauskas 1972) and (Gnielinski 1979) from the VDI (Stephan 2010).

It was found in the simulations of the experiments done by (Murray 1993) and (Zukauskas 1972) that the heat transfer rate is very sensitive to y^+-value. See Appendix C. It was also concluded that the blended wall functions of (Kader 1981) performed better than standard wall functions. Therefore tests using the blended wall functions of (Kader 1981) with pressure gradient and heat transfer correction for compressible flows by (White & Christoph 1971) and (Huang, Bradshaw & Coakley 1993) with different y^+-values were conducted.

Non-equilibrium wall functions by (Kim, Choudhury & Patel 1997) were also evaluated. The Realizable k-ε turbulence model was implemented with all wall functions.

Since a Reynolds number range was evaluated for reasons stated before, from here on reference will be made to the average y^+-value at a Reynolds number of 4000 and first layer thickness (FLT) of the mesh, although the y^+-value varies for the Reynolds number range, around the tubes and throughout the bank.

The FLT refers to the height of the cells adjacent to the tube walls. The same mesh was used across the Reynolds number range per curve presented.

The following equations from (Zukauskas 1972) were used to plot the emperical values for the Reynolds number range evaluated:

$$Nu_f = 0.27 Re_f^{0.63} Pr_f^{0.36} \left(\frac{Pr_f}{Pr_w}\right)^{0.25} \tag{83}$$

$$K_f = Nu_f Pr_f^{-0.36} \left(\frac{Pr_f}{Pr_w}\right)^{-0.25} \tag{84}$$

Where reference is made to the global heat transfer rate of the entire tube bank, the results were calculated based on the total heat flux of all the tubes. The mass-weighted air temperature at the outlet of the bank was used for these calculations.

The results using the traditional recommended y^+-value range of 30 to 300 and the wall functions of (Kader 1981) did not correlate well with the empirical correlations. The flow phenomena in the tube bank deviate substantially from flat plate flow (for which wall functions were developed) due to the non-equilibrium characteristics of impingement, separation and reattachment as shown in Appendix C. Therefore wall functions are not suitable and the aim of this study was to establish if it could be considered by evaluating the error made for the computational saving.

A 5mm FLT with a y^+-value of 3.9 delivered the best results with the wall functions of (Kader 1981). However the trend of K_f vs. Reynolds number for the results of a 5 mm FLT (see Figure 7.2) differed from the correlations of (Zukauskas 1972) and (Gnielinski 1979) and the heat transfer rate on a global scale of the entire bank was under predicted by 37 %. The heat transfer per row was also investigated and it was found that the first row was over-predicted compared to the experimental evidence of (Zukauskas 1972) which indicates a 20 % lower heat transfer than the in-bank rows for all the geometries that he investigated.

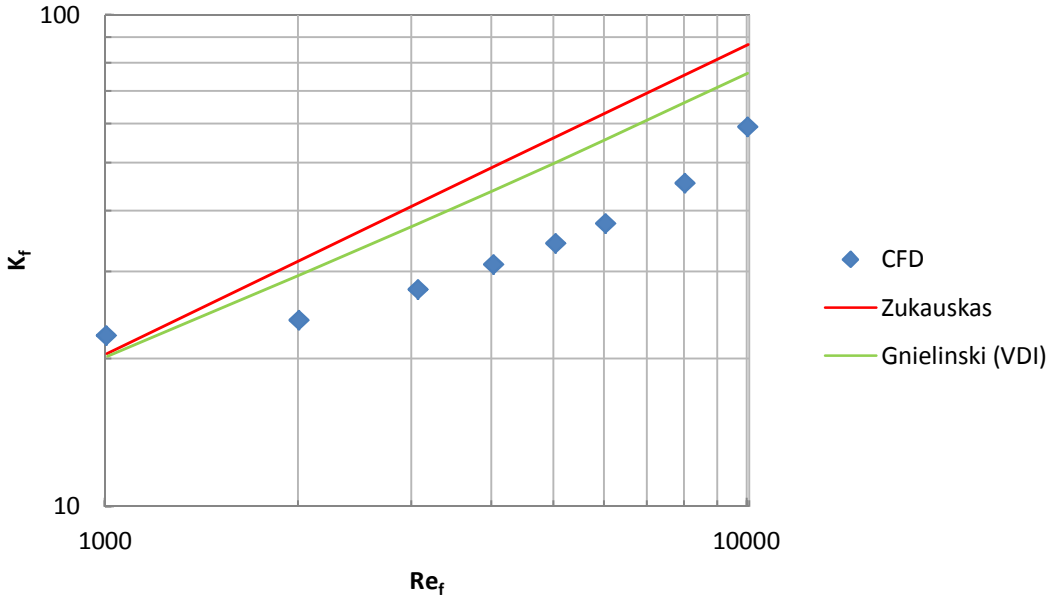

Figure 7.2: Comparison of CFD results using blended wall functions of (Kader 1981) (5 mm FLT) to empirical correlations

Non-equilibrium wall functions were developed for flow involving separation, reattachment and impingement, (ANSYS Inc. 2013). Experiments with different FLT and number of layers in the mesh around the tubes yielded 0.35 mm FLT at a y^+-value of 0.8 and 5 layers as the best configuration.

This trial and error approach was again used since (Kim, Choudhury & Patel 1997) used a wide range of y^+-values during validation as discussed in Chapter 4. The back step validation study was the closest to the current tube bank configuration. The y^+-value range was 13 to 22 for the back step simulation.

The non-equilibrium wall functions delivered better results compared to the wall functions of (Kader 1981). The trend of K_f vs Reynolds number was closer to the empirical correlations of (Zukauskas 1972) and (Gnielinski 1979). The absolute values also compared very well with the experimental correlations. This produced results in between the empirical correlations of (Zukauskas 1972) and (Gnielinski 1979) at a Reynolds number of 4000.

Correlations of (Grimison 1937) and (Kuznetsov et al. 1973) also compared very well to the (Gnielinski 1979) correlation used in the VDI method (see Figure 7.3).

The heat transfer per row was also investigated with non-equilibrium wall functions and the first row was over-predicted. After simulations with different combinations of FLT on the first and in-bank rows the correct heat transfer distribution could be captured as with the Zukauskas geometry discussed in Appendix C. The resulting mesh presented challenges when implemented in 3D on the boiler simulation and was not pursued.

The heat transfer rate locally around the tube circumference at a Reynolds number of 4000 was also verified using non-equilibrium wall functions and found to correspond to published trends by (Zukauskas 1972).

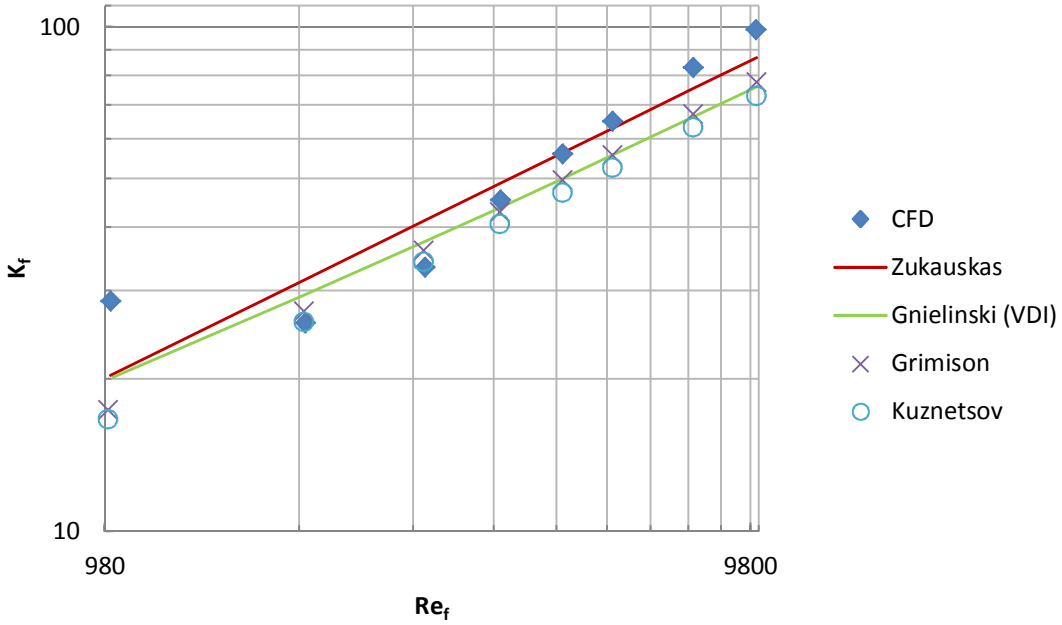

Figure 7.3: Comparison of CFD results using non-equilibrium wall functions (0.35 mm FLT) to empirical correlations

The pressure drop over the bank was verified against the correlations of (Zukauskas 1972) and (Gnielinski 1979). It was found within 6 % accuracy at a Reynolds number of 4000 and 24 % for Reynolds numbers of 3000 and 5000 respectively. This was deemed acceptable since pressure drop is not critical in the superheater.

Due to the low gas-side velocity and the fact that the bank is not very deep, the pressure drop is very low and has minor effects on the flow compared to e.g. temperature gradients. From the study on the Zukauskas geometry in Appendix C, increasing the grid resolution would improve the accuracy considerably although it was not feasible on this scale mesh, where the count was already in excess of 25 million cells for the TSB Komati boiler using the current resolution as seen in Figure 7.1.

The effect of turbulence intensity on the 2D tube bank heat transfer rate was verified. Specifying 100 % turbulence intensity at the inlet of the 2D domain increased the heat transfer rate by 86 % using non-equilibrium wall functions and only 13 % and 25 % using blended and standard wall functions respectively.

This indicated that the heat transfer is very sensitive to turbulence intensity and non-equilibrium wall functions are much more sensitive than other wall functions.

(Lowery & Vachont 1974) investigated the effect of turbulence on heat transfer from heated cylinders. They concluded from experiments and other studies that increases in heat transfer rate up to approximately 60 % can be obtained at the highest values of turbulence intensity for the stagnation point and laminar boundary layer. It was also found that the increase reaches an asymptotic maximum value.

(Lowery & Vachont 1974) also investigated the overall heat transfer around the cylinder and found that increases in turbulence can decrease the heat transfer in the wake, depending on the turbulence length scale. Figure 7.4 indicates that a maximum increase in overall heat transfer of approximately 47 % can be expected at the highest levels of turbulence intensity.

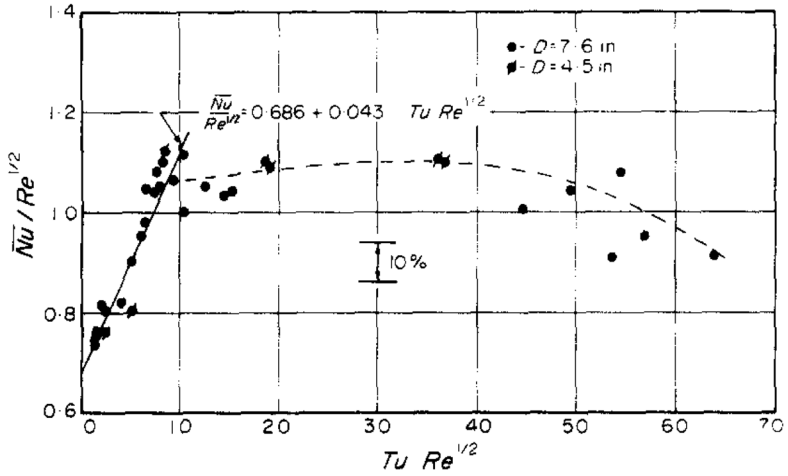

Figure 7.4: Effect of turbulence intensity on overall heat transfer, (Lowery & Vachont 1974)

Therefore it was concluded that non-equilibrium wall functions are over-predicting heat transfer due to turbulence intensity, since the 86 % increase achieved in the 2D experiments is not physically possible according to (Lowery & Vachont 1974).

The change in heat transfer rate of the tube bank with the flow at different angles of attack was verified against the results of (Zukauskas 1972). This was tested by extruding the 2D mesh to 3D at an economical mesh resolution to be applied in the full boiler simulation. The flow was channelled at different angles over the tubes. It was found that the trend of Figure 7.5 by (Zukauskas 1972) could be captured with the final resolution chosen using non-equilibrium wall functions. The results were also mesh independent. See Figure 7.6 where the data labelled 90 degrees is for flow perpendicular to the tube axis. For a Reynolds number of 4000 the correction factor is 0.846 and 0.625 for the CFD results at 45 and 10 degrees respectively.

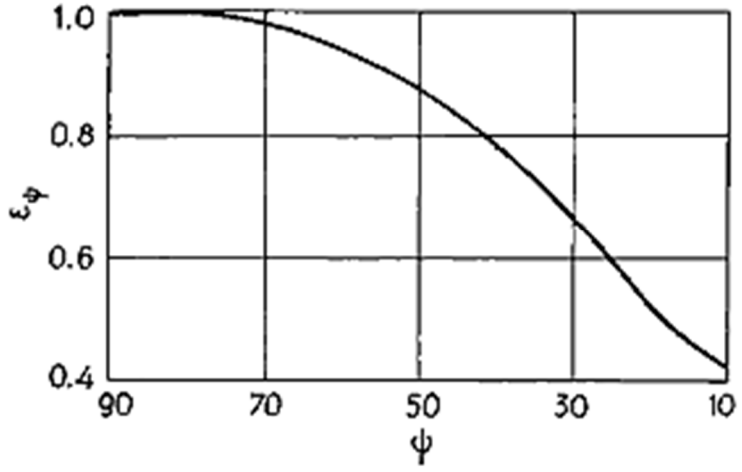

Figure 7.5: Dependence of heat transfer of banks on the angle of attack, ϕ with correction factor ε_ϕ

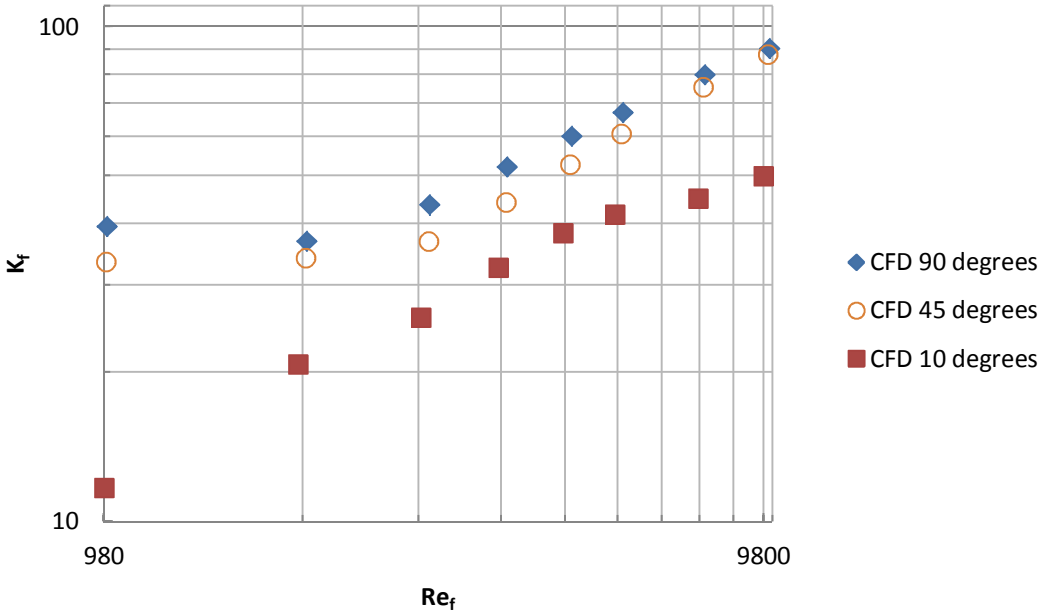

Figure 7.6: Comparison of CFD results using non-equilibrium wall functions at different angles of attack

Non equilibrium wall functions were also implemented on the 3D TSB Komati boiler model. The results indicated that the heat transfer to the superheater and resulting steam temperature is very sensitive to FLT and wall function. E.g. changing to the blended wall functions by (Kader 1981) in the boiler simulation nearly halved the convective heat transfer, as predicted by the 2D study.

The steam temperature was unrealistically high using non-equilibrium wall functions. The turbulence intensity at the inlet to the superheater was 180 %, which should increase the heat transfer by 47 % at most according to (Lowery & Vachont 1974).

However the 2D results indicate that the effect of turbulence intensity on the heat transfer rate using non-equilibrium wall functions can be an 86 % increase. Therefore it was concluded that the high steam temperature is attributed to the over-prediction of heat transfer with turbulence intensity.

7.2. Two-layer zonal model

The two-layer near wall treatment approach of (Wolfshtein 1969) with the Realizable k-ε turbulence model was evaluated using the 2D TSB Komati tube bank geometry.

A y^+-value of less than 4 is recommended with at least 10 cells in the viscosity-affected near-wall region, as described in Chapter 4. Different FLT values (corresponding to y^+-values within the recommended range) and amount of cells in the near-wall-region were evaluated.

The best combination resulted in a 57 % under-prediction of heat transfer rate at a Reynolds number of 4000 (see Figure 7.7). The FLT value was 0.15 mm with 15 layers at a y^+-value of 0.2.

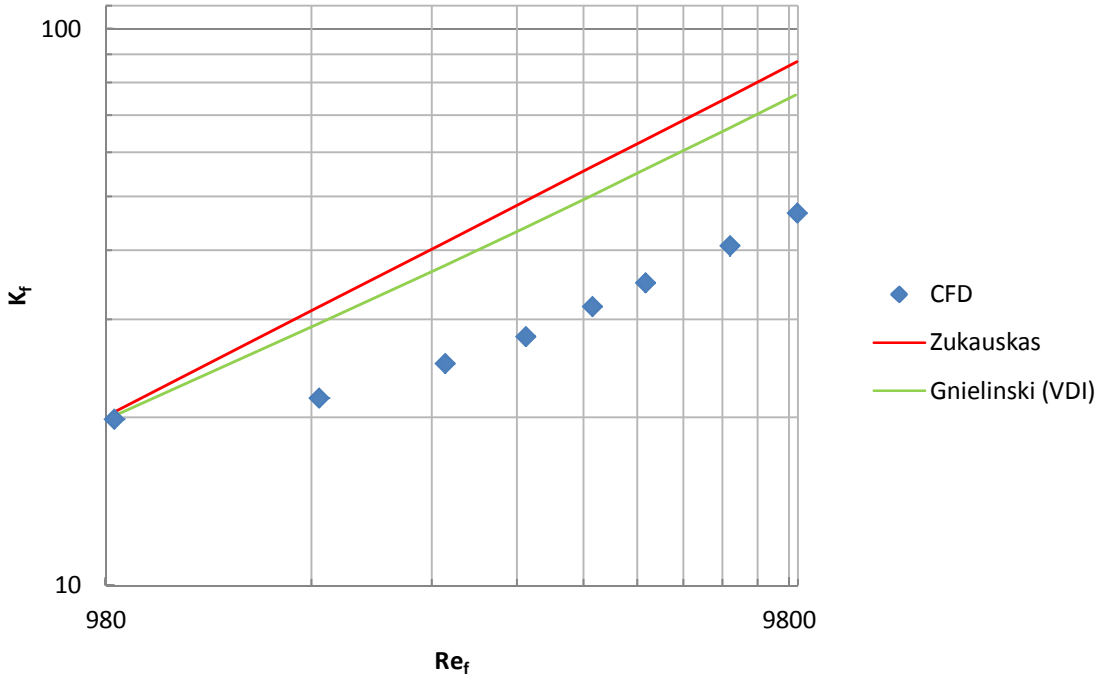

Figure 7.7: Comparison of CFD using the two-layer model of (Wolfshtein 1969) to empirical correlations

Due to the fact that the two-layer model of (Wolfshtein 1969) is part of the suite of models called "enhanced wall treatment" which alternates between wall functions and the two-layer model, a combination of these two approaches was tested at y^+-values higher than 1.

The best performance was achieved with a FLT of 0.75 mm and 5 layers at a y^+-value of 1.3. However the heat transfer was under-predicted by 53 %.

Due to the poor global performance of this model, no further detailed analysis was done. It also delivered a much lower steam temperature compared to the wall functions and LRN models when implemented on the boiler simulation as expected from the 2D results.

7.3. Low-Reynolds-Number (LRN) k-ε turbulence models

Low-Reynolds-number (LRN) k-epsilon turbulence models were evaluated with the 2D Komati mesh. LRN turbulence models are superior to high-Reynolds-number k-ε formulations with regards to near wall effects and can also capture streamline curvature, rotation and jets.

A y^+-value of less than 4 is recommended with at least 10 cells in the viscosity-affected near-wall region, as described in Chapter 4. Different FLT values (corresponding to y^+-values within the recommended range) and amount of layers were tested.

A 0.35 mm FLT with a y^+-value of 0.7 delivered the best results.

Globally the total heat transfer rate using LRN models were slightly less than using non-equilibrium wall functions.

The pressure drop over the bank was verified against the correlations of (Zukauskas 1972) and (Gnielinski 1979). The accuracy at a Reynolds number of 4000 was 9 %. At Reynolds numbers of 3000 and 5000 it was 25 % and 1 % respectively. This was deemed acceptable since pressure drop is not critical in the superheater.

The effect of heat transfer rate per row and locally around the circumference of the tubes was superior to using non-equilibrium wall functions.

Most importantly the increase on heat transfer due to 100 % turbulence intensity was 53 % in-line with the findings of (Lowery & Vachont 1974).

The disadvantages of using LRN models are the resolution required at the walls and the numerical stiffness due to the damping functions.

The mesh resolution around the tubes used for non-equilibrium wall functions was found suitable for using LRN k-ε models as well. Since the recommendation for using LRN models is 10 layers of finer mesh on the wall, a comparison with 10 layers to 5 layers was performed.

As can be seen in Figures 7.8 to 7.11, for the global heat transfer rate- over the bank, per row and around the tube respectively, 5 layers is sufficient using the LRN model of (Chang, Hsieh & Chen 1995). An improvement on pressure drop accuracy at a Reynolds number of 4000 from 9 % to 2 % was noted with 10 layers, but not worth the computational effort as pressure drop is not critical.

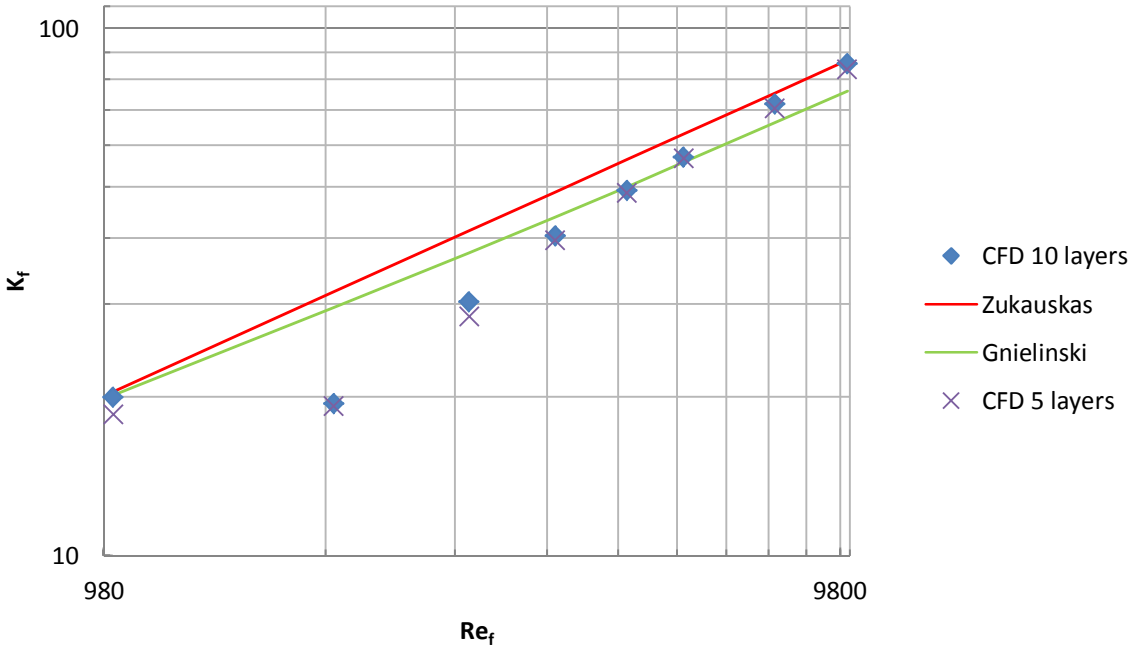

Figure 7.8: Comparison of CFD using the LRN model of (Chang, Hsieh & Chen 1995) to empirical correlations

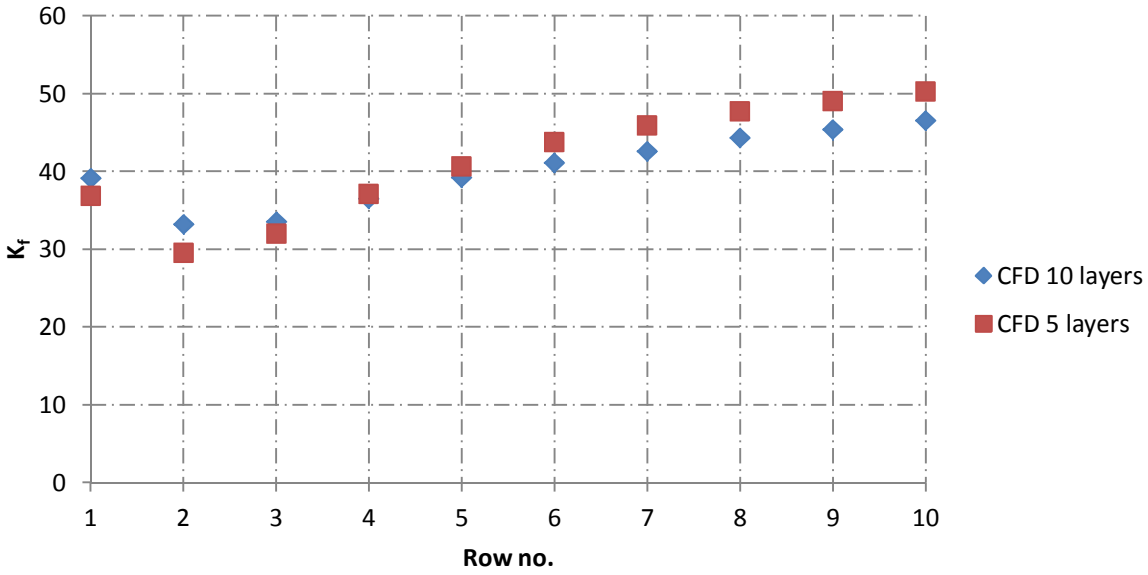

Figure 7.9: CFD results of heat transfer per row using the LRN model of (Chang, Hsieh & Chen 1995)

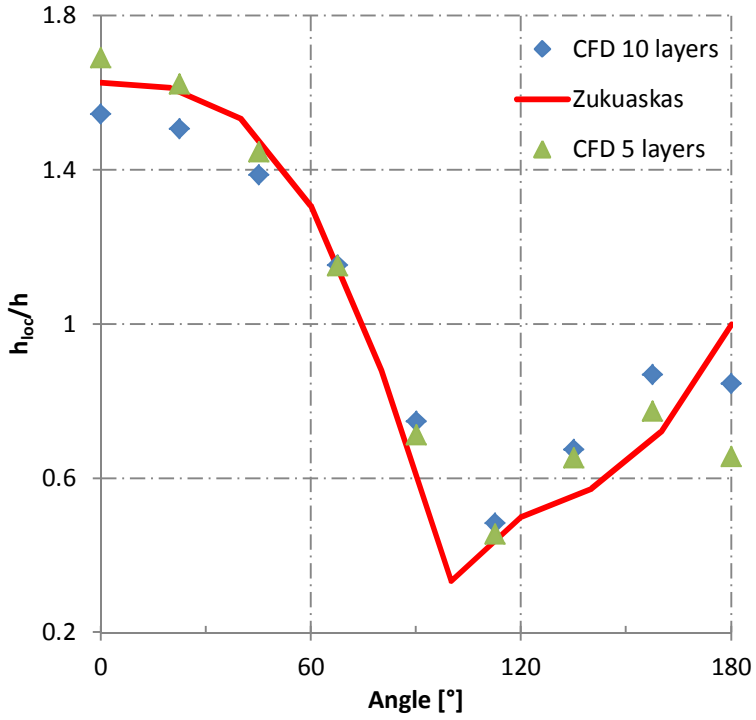

Figure 7.10: Comparison of CFD using the LRN model of (Chang, Hsieh & Chen 1995) to Zukauskas experiments for heat transfer coefficient around first tube (0° at front of tube)

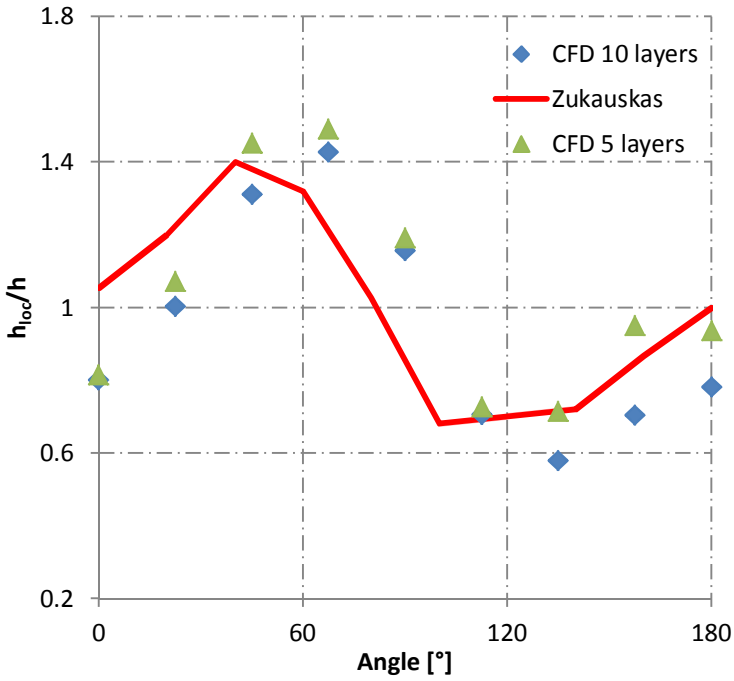

Figure 7.11: Comparison of CFD using LRN model of Chang-Hsieh-Chen to Zukauskas experiments for heat transfer coefficient around in-bank tube (0° at front of tube)

The heat transfer of the tube bank with the flow at different angles of attack was verified using the model of (Chang, Hsieh & Chen 1995). As with non-equilibrium wall functions it was found that the trend was captured with the final resolution chosen. The results were also mesh independent. Comparing Figure 7.12 to 7.5 at a Reynolds number of 4000, the correction was 0.8 for an angle of attack of 45 degrees.

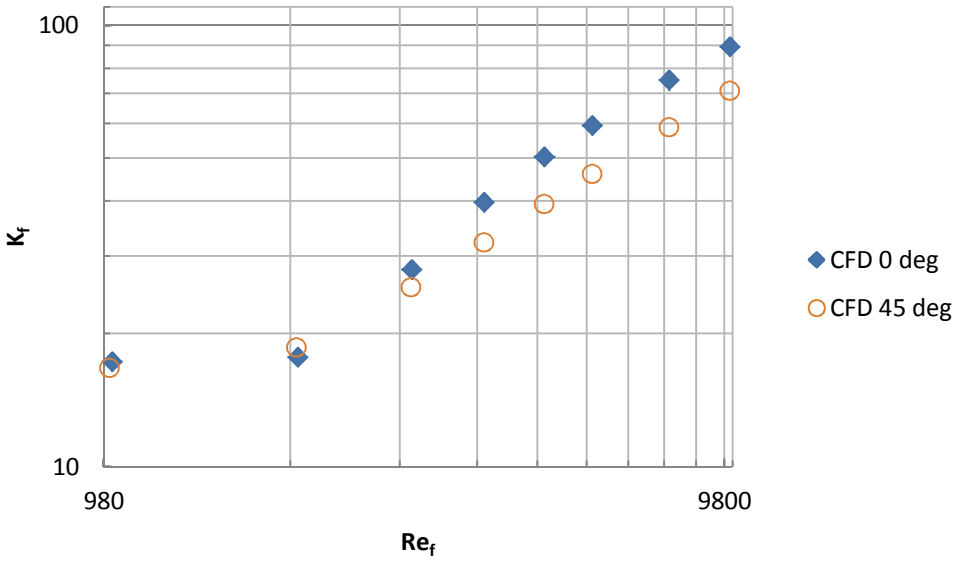

Figure 7.12: Comparison of CFD results using LRN model of Chang-Hsieh-Chen (0.35 mm FLT) at different angles of attack

From the 5 LRN k-ε turbulence models available in ANSYS® the models of (Abid 1991), (Launder & Sharma 1974) and (Chang, Hsieh & Chen 1995) correlated the best with the global empirical correlations in 2D.

These three models were implemented in the TSB Komati boiler simulation and resulted in a substantial decrease in steam temperature compared to using non-equilibrium wall functions; however the results using the model of (Launder & Sharma 1974) were 20 °C higher than the two other LRN models.

The model of (Chang, Hsieh & Chen 1995) was chosen above the model of (Abid 1991) due to superiority with regards to numerical stability and convergence observed in the 2D and 3D tube bank simulations.

This model was specifically developed for near wall phenomena of flow separation. The performance in the near-wall region of the re-attachment point was validated for recirculating flow in a pipe expansion. Since the majority of the heat transfer takes place at the flow re-attachment points on the sides of the tubes in the superheater bank, this model is ideally suited.

Numerical instabilities were noted in the Komati simulation compared to using Realizable k-ε and non-equilibrium wall functions. This problem was solved by applying relaxation to the energy equation.

The resulting steam temperature of the Komati model was 30 °C above the measured value on site.

7.4. Conclusions from using different turbulence near-wall treatment

Considering the three turbulence wall treatment approaches evaluated, the most accurate overall results were achieved using the LRN k-ε turbulence model of (Chang, Hsieh & Chen 1995).

It was found that FLT had the largest effect on the heat transfer rate results. Mesh independence for heat transfer rate was reached at the final mesh resolution chosen, see Figure 7.1. A higher resolution had an impact on pressure drop only which was not important for the focus of the current study.

Globally looking at the heat transfer over the entire tube bank, the non-equilibrium wall functions of (Kim, Choudhury & Patel 1997) performed the best of all the wall functions compared to the empirical correlations. The CFD results were between the correlations of (Zukauskas 1972) and (Gnielinski 1979) at a Reynolds number of 4000.

The two-layer near wall treatment approach of (Wolfshtein 1969) under predicted the heat transfer by 57 %. The LRN k-ε turbulence model of (Chang, Hsieh & Chen 1995) produced results with 10 % lower heat transfer at a Reynolds number of 4000. See Figure 7.13 for a comparison of the three near-wall treatment approaches.

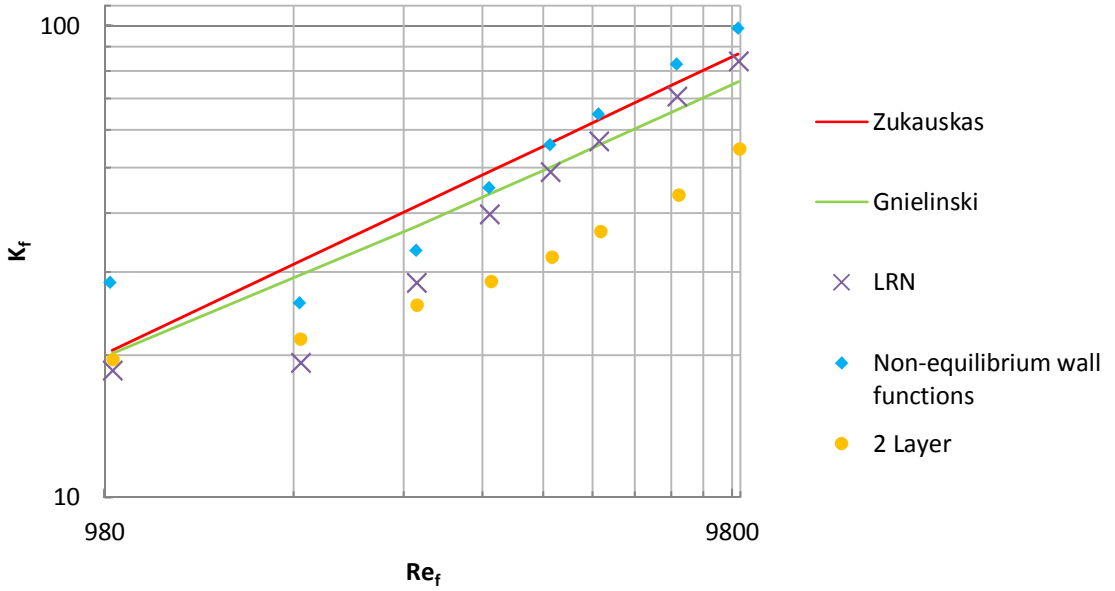

Figure 7.13: Comparison of CFD results using the LRN model of (Chang, Hsieh & Chen 1995), non-equilibrium wall functions of (Kim, Choudhury & Patel 1997) and the 2 layer model of (Wolfshtein 1969) to empirical correlations

The heat transfer per tube row could be captured realistically using the LRN k-ε turbulence model of (Chang, Hsieh & Chen 1995) only. The wall functions and 2 layer models required a different FLT on the first tube row which was not feasible for the boiler simulation.

The CFD results of heat transfer coefficient plotted around the circumference of a tube was the closest to experimental results using the LRN k-ε turbulence model of (Chang, Hsieh & Chen 1995).

The effect of turbulence intensity on tube bank heat transfer could be realistically modelled using the LRN k-ε turbulence model of (Chang, Hsieh & Chen 1995) only. Due to the high level of turbulence at the inlet of the superheater, it has a large impact on the steam temperature of the boiler model, making the LRN approach the only viable option.

The 3D effects varying the angle of attack of the flow over a tube bank could be captured using non-equilibirum wall functions of (Kim, Choudhury & Patel 1997) and the LRN k-ε turbulence model of (Chang, Hsieh & Chen 1995).

The LRN approach is the only method that delivered consistent accurate results for all the geometries tested and heat transfer phenomena evaluated. Refer to Appendix C for the other geometries. The (Chang, Hsieh & Chen 1995) turbulence model was therefore chosen as the most appropriate for the boiler simulation specifically considering tube bank heat transfer.

The convective heat transfer on the inside of the tubes was also verified in a similar manner as explained in this chapter. However the heat transfer coefficient is 20 times higher than the outside; see the lumped parameter model calculations in Appendix B. Therefore it is of minor importance and not discussed.

8. Radiation, fouling and effect on heat transfer

The model settings that produced the best results in the preceding 2 chapters delivered a steam temperature that is higher than measured in the boiler when combined in the composite boiler model. Therefore other mechanisms that could reduce the heat transfer to the superheater were explored.

The only relevant model parameters with respect to radiation heat transfer that could be changed were the choice of radiation model, the emissivity of the surfaces and radiation model angular discretisation.

The DO radiation model used is the most comprehensive from the choices available in ANSYS® Fluent, as discussed in Chapter 4, and was thus not altered. The emissivity of the surfaces was set to 0.95 for the tube walls and 0.6 for the superheater pipes. Altering these values to reduce the heat transfer rate to the superheater would be unrealistic based on the research of (Furmański 1995).

More radiation heat transfer to the furnace and less to the superheater would require a higher emissivity on the tube walls and lower value on the superheater tubes. The mat black value of 0.95 corresponds to the furnace tube wall colour and values that are higher would be unrealistic. The value of 0.6 of the superheater tubes is typical for boiler tubes with a light coloured ash layer and lower values would also be unrealistic. Therefore only a finer angular discretisation was tested with negligible effects.

The conclusion from the preceding 2 chapters is that there is a thermal resistor in the system resulting in a 30°C drop on steam temperature which is unrelated to tube bank convection heat transfer, radiation and combustion, since these aspects of the simulation have been verified.

John Thompson has been including fouling factors in heat transfer calculations for years. Fouling resistances are also widely documented for heat exchangers (Mills 1995). (Baxter 1998) stated that even a small amount of ash on a heat transfer surface can decrease the local heat transfer by a factory of 3 or more. Therefore the thermal conductivity of ash deposits on boiler tubes was investigated.

Studies from (Ots 2011), (Richter, Payne & Heap n.d.), Baxter, (Robinson et al. 2001) and (Furmański 1995) were compared. Figure 8.1 from (Furmański 1995) summarizes the findings. The thermal conductivity of boiler ash deposits ranges from 0.03 to 3 W/m.K. It can be classified into four main groups, loose and weakly bound deposits – 0.1 W/m.K, bound and sintered deposits – 1 W/m.K, slag deposit – 2 W/m.K and iron rich slag deposit – 3W/m.K.

Bagasse fired boilers have loose and weakly bound deposits on the superheaters as can be seen in Figure 8.2 of Komati. The picture was taken from the left hand side of the boiler between the superheater and mainbank. It shows the rear end of the tube bank where the least amount of fouling takes place. This phenomenon was also witnessed when the suction pyrometer fouled during the temperature measurements in front of the superheater.

The data in Figure 8.1 indicated with the arrow corresponds to the temperature of the superheater tube metal surface and also the type of deposit. Therefore a value of 0.2 W/m.K for the thermal conductivity of the ash deposit was used in the simulation. A thickness of 0.675 mm resulted in the steam temperature measured on site. This thickness is realistic from years of boiler inspection experience within John Thompson. The resulting fouling resistance of 0.0034 m^2.K/W also corresponds to values measured for coal of 0.0035 m^2.K/W by (Allmon & Watson 1991) which is also similar to values in (Mills 1995) for heat exchanger with dirty gasses.

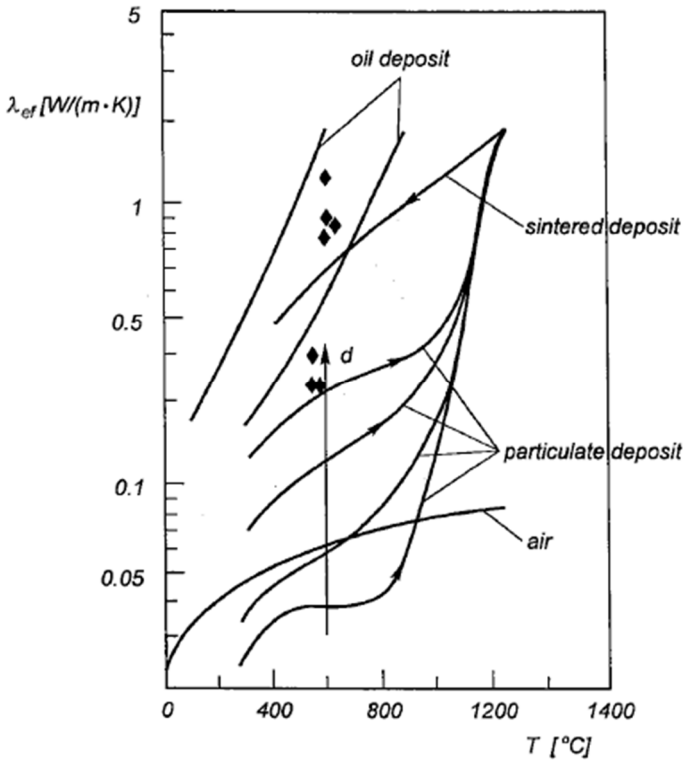

Figure 8.1: Dependence of the effective thermal conductivity of the ash-deposit on temperature and grain size d. ♦ - results for ash-deposits from Polish coal-fired boilers (Furmański 1995)

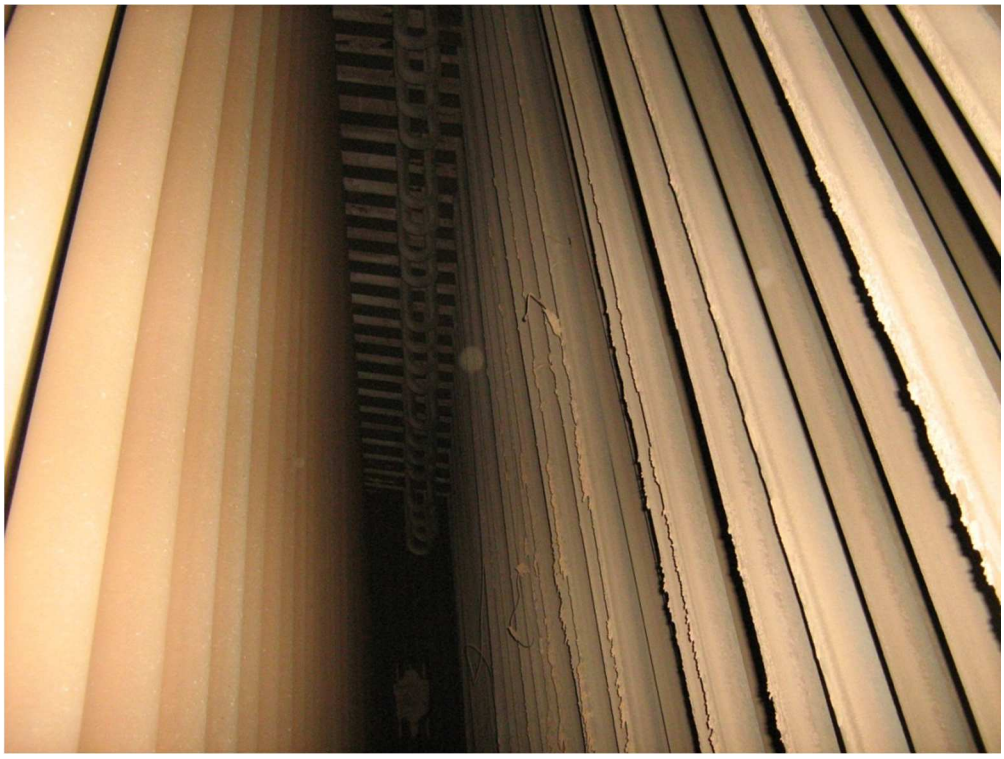

Figure 8.2: Ash-deposits on TSB Komati superheater

9. Composite numerical model

The geometry and physics involved with modelling combustion in an industrial scale boiler is complicated and the size of the domain very large. Therefore assumptions were made while maintaining enough features and resolution to capture the areas of interest.

9.1. Geometry

The first major assumption was that the domain and physics are symmetrical about the centre line of the boiler.

It was found that the air flow profile is symmetrical about the centre of the grate and only half of the boiler needed to be modelled saving vast computational expense. See Chapter 5.

Meshing

The physical size of the geometry resulted in a very large cell count due to the high resolution in the superheater region where accurate modelling of convective heat transfer was required.

Therefore a hexahedral mesh was constructed in order to use the minimum number of elements while maintaining a high quality. The furnace section between the grate and the superheater was simulated with a relatively coarse mesh at a maximum cell edge size of 0.1 m since the dominant heat transfer mechanism is radiation.

The section between the superheater and outlet of the domain was also at the coarse global sizing. It only ensures that the flow patterns in the superheater tube bank due to the pressure drop and heat exchange in the mainbank are not neglected. The effect of the flow curvature at the boiler outlet was also accounted for by including the ducting (see Figure 9.1).

The fuel spreaders were modelled in detail in order to capture the aerodynamics of the spreader plate and air slot. The chute above was included to ensure a more realistic injection of the fuel particles into the domain. The interaction of the fuel particles with the air jet over the plate is therefore accounted for as it drops down the chute.

In order to capture the conical shape of the rear secondary air jets, a finer resolution tetrahedral mesh was used. This is the only area where a hexahedral mesh was not used. The variation in mesh resolution of the superheater section can be seen in Figure 9.1. The rest of the mesh is identical to Figure 6.1 in Chapter 6. The total cell count was 25 million for a domain extending 15m high, 10m deep by 4 m wide.

A smaller sizing of the grid was used to capture the air jet of the spreaders. The grid was aligned on certain faces to ensure that a good quality hexahedral mesh with a low cell count could be aligned with the flow (see Figure 9.2).

The secondary air jets were captured similarly with a finer resolution mesh. The tetrahedral mesh ensured a cylindrical growth from a finer to a coarser resolution grid, corresponding to the shape of the jet (see figure 9.3).

The superheater tube bank consists of 40 elements pitched at 200 mm across the width of the boiler. Each element consists of 8 tubes bent and welded together in a serpentine configuration forming 4 loops along the direction of gas flow.

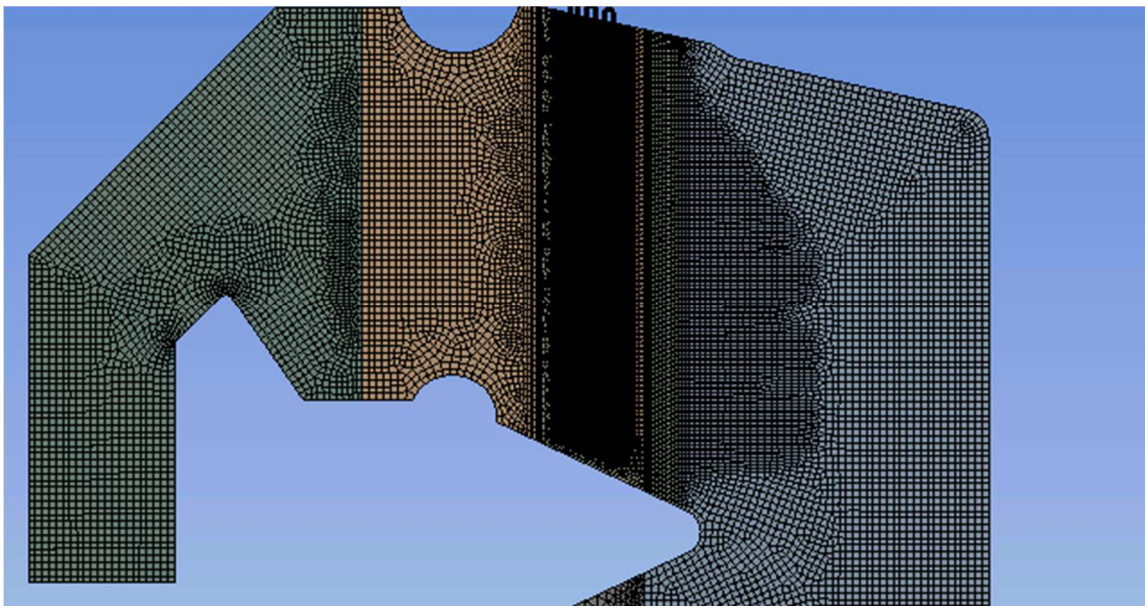

Figure 9.1: Side view of top part of mesh

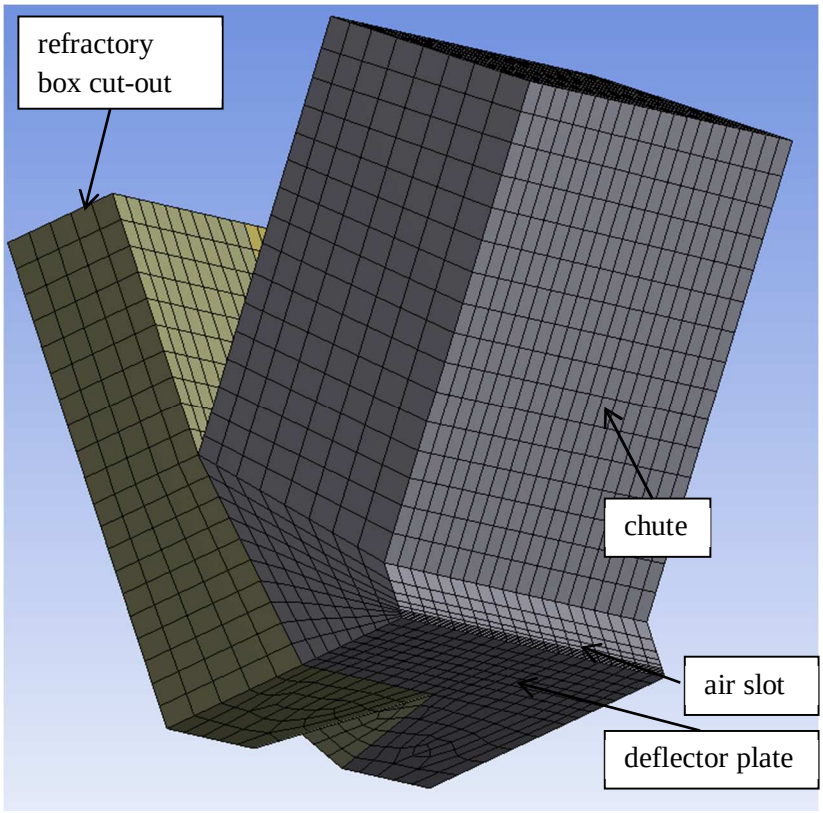

Figure 9.2: Spreader mesh

The mesh of the superheater tubes were swept along the profile of the elements, starting with the steam volume, the metal and then the gas. Around the metal the gas was divided into 4 sections along the width of the boiler and a “jacket” per loop. A finer mesh resolution was used on the inside and outside of the tubes with a first layer thickness of 0.35 mm on the outside and 1 mm on the inside to ensure the correct y^+-value (see Figure 9.4).

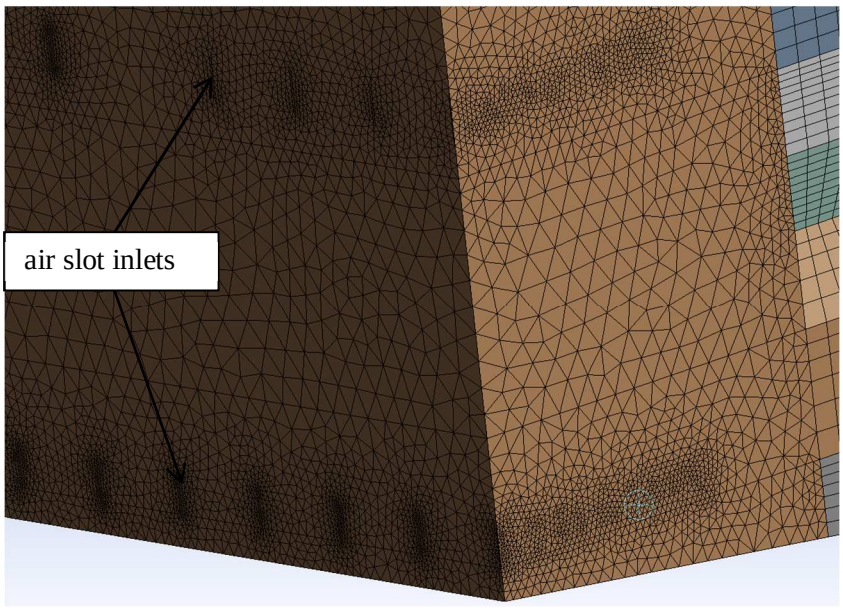

Figure 9.3: Secondary air mesh

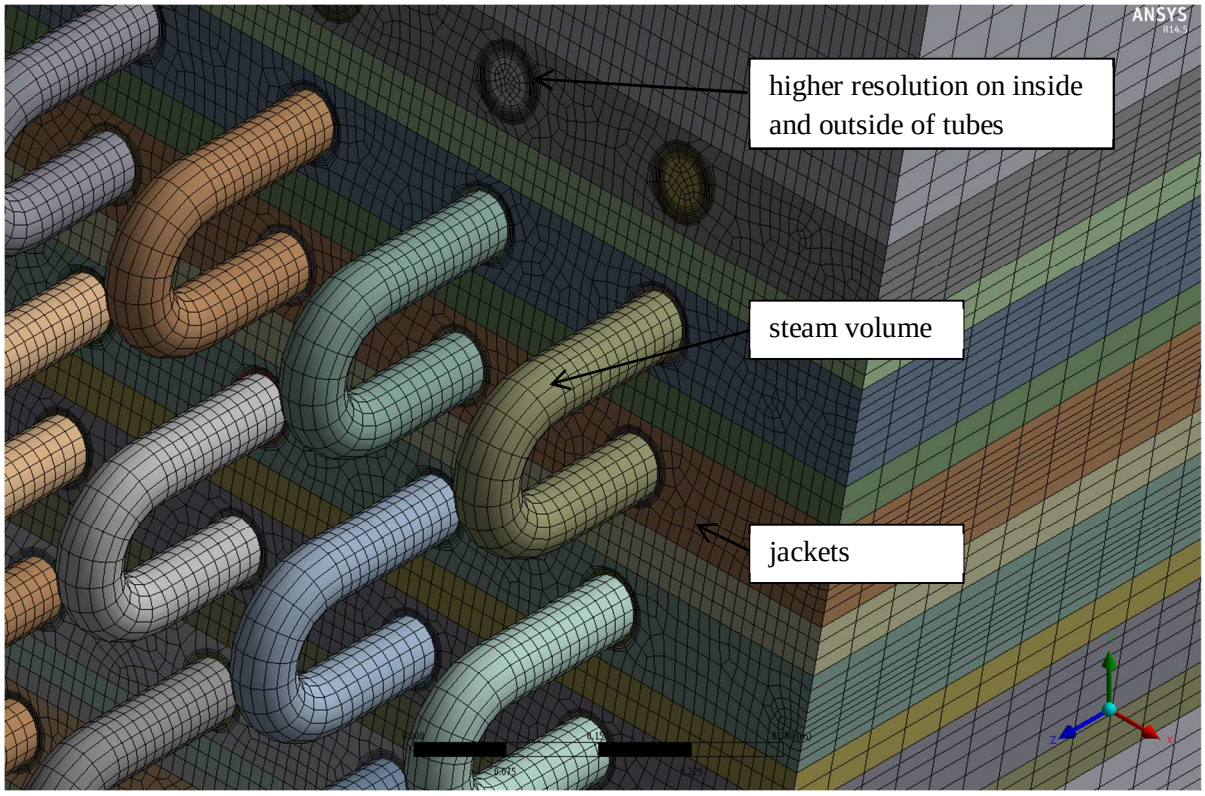

Figure 9.4: Isometric view of superheater mesh

The average y^+- value was 0.25 on the gas side around the tube circumference. On the steam side the y^+- value varied in the range from 30 to 300. The turbulence models used in the simulation patch empirical functions from the first node to the walls or solve the turbulence transport equations right up to the walls with damping functions. Therefore the y^+- value is critical in simulating the boundary layers of the tubes correctly. Both these approaches require calibration by changing the y^+- value, as discussed in Chapter 4.

The meshing sequence was from the superheater section outwards to the outlet ducting in the one direction and to the grate in the other direction. The secondary air sections were meshed last.

9.2.Model settings

The pressure based solver was used since the flow is incompressible. A steady state simulation was run. Gravity was taken into account since it is required for the particle dynamics. It is also needed for buoyancy effects resulting from the large temperature gradients in the combustion gas

Heat exchanger

The section downstream of the superheater, namely the mainbank, consists of an array of tubes that would increase the cell count substantially if modelled similar to the superheater, therefore it was accounted for by utilising a "Heat Exchanger Model" available in ANSYS® Fluent.

This software feature calculates energy and momentum sources in a volume based on user input of a heat exchanger to simulate the heat transfer and pressure loss. Site data from TSB Komati was used for the setup.

Since this section of the boiler has a small effect on the flow patterns over the superheater upstream and a small amount of radiation passes through the superheater bank, it was deemed acceptable considering the computational expense of a more detailed modelling approach.

Fuel

Similar to the "Heat Exchanger Model" described before, ANSYS Fluent incorporates a "Coal Calculator" which determines the homogeneous reactions based on the volatile molar mass, proximate and ultimate analysis of the fuel.

The volatile molar mass was based on pyrolysis experiments of bagasse done by (Zanzi, Sjostrom & Bjornbom 1995). An average value from different size ranges at the combustion temperature in the boiler furnace was calculated. The proximate and ultimate analysis of bagasse samples taken at the time of the tests done at TSB Komati was used.

Materials

Most of the materials were available in the ANSYS® Fluent database. Some specific to the boiler industry had to be defined e.g. the tube metal, refractory, steam and the bagasse particle.

The tube metal and refractory properties were based on material data sheets.

To save computational expense, the steam properties as a function of temperature only for the pressure in the superheater were determined with polynomial fits using functions by (Spang 2002). The effect of pressure change due to the losses associated with the friction and bends inside the superheater tubes were accounted for.

Boundary conditions

The boundary conditions were based on the indirect efficiency calculation of BS845 (British Standards Institution 1987), the fuel analysis and site data from TSB Komati. Sample calculations from a spread sheet can be found in Appendix A.

The most important parameters are the following:

1) Operating conditions

2) Fuel flow

3) Airflow

4) Steam flow conditions

5) Conditions at the walls

The operating conditions were based on the site data at the time of the tests on the boiler. The trends were analysed and the fuel and air flow calculated based on the output of the boiler. These calculations consist of a global combustion reaction calculation based on the fuel analysis to determine the amount of air per fuel to achieve specified oxygen content in the flue gas at the boiler exit. The amount of fuel burnt is calculated from an energy balance using an indirect efficiency based on the final gas temperature after the last boiler heat recovery exchanger and the composition of the fuel.

A constant temperature equal to saturated water at the steam drum pressure during nucleate boiling was specified on the outside of the parts of the domain subjected to water cooling. Conduction heat transfer was calculated from this temperature to determine the furnace tube wall and refractory temperature based on the material thickness and properties specified. Thus the water cooled wall temperatures or hot face temperature exposed to the combustion gas was higher than the water temperature.

The emissivity of the furnace tubes, refractory and superheater tubes were based on the work done by (Furmański 1995) on thermal and radiative properties of boiler heat transfer surfaces.

Solution methodology

A solution methodology was followed due to the complexity and coupled nature of the simulation. At first the model was run to convergence using first order discretization without the discrete phase. Constant value fluid properties were also used to improve stability.

Next the discrete phase was added and relaxation applied. Again the simulation was run to convergence changing the relaxation back to the default values with progressive incremental steps except for the discrete phase.

In the next step the radiation model was activated without particle radiation interaction at first and with relaxation applied.

After reaching stable, near-converged results, the simulation was switched to second order discretisation and again run to convergence. The last step was adding temperature dependent functions for the material properties.

The standard convergence criteria of a decrease in residuals by three orders of magnitude except the energy residual of six orders were used. Plots of all the important variables namely O_2 content in the combustion gas at the outlet, CO content in combustion gas at the outlet, combustion gas temperature at the outlet, steam temperature, heat flux to superheater and heat flux to furnace were also monitored until no changes were seen.

10. Comparison of boiler measurements to composite model

Three sets of tests were conducted on TSB Komati boiler no.3 in September 2012, July 2013 and September 2013. The duration was a week each. The experimental equipment and procedure are discussed Chapter 3. The objective of these tests was to validate the CFD model in the region of the superheater.

The measurements taken during these tests were compared with the results from the composite CFD model as described in Chapter 9 set up for the conditions during the test.

During the second site visit only a single temperature traverse was taken. The location was at the bottom sootblower access port behind the superheater as seen in Figure 3.6 of Chapter 3.

The measurements were slightly lower than the CFD predictions, as can be seen in Figure 10.1.

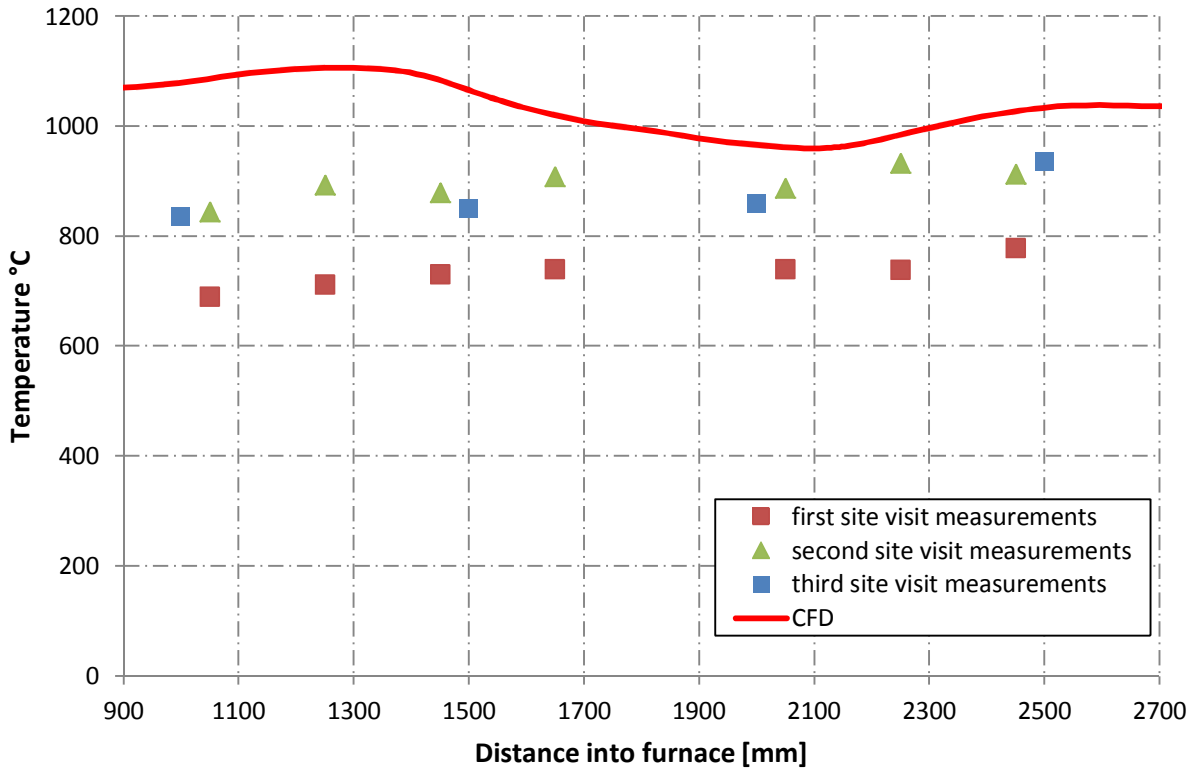

Figure 10.1: Temperature profile across width of boiler

However the difference is 15 % on average and given the difficult testing conditions, the agreement is good.

The Durag camera also measured a temperature of 900 °C on average at the same time in the same location as the suction pyrometer, giving confidence in these two instruments. See Figure 10.2.

A consultant was used during the first site visit due to the fact that John Thompson did not own the correct equipment to measure temperatures in excess of 450 °C at the time.

It is interesting to note that the suction pyrometer with the low gas velocity used during the first site visit, read consistently lower by about 160 °C, as expected. This resulted in an error of 17 %.

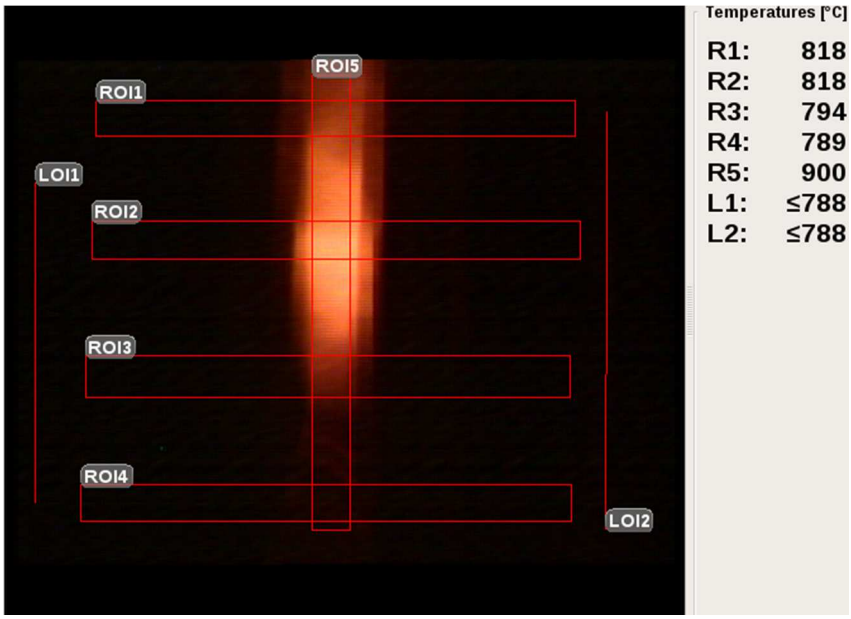

Figure 10.2: Screenshot from Durag camera of image taken from sootblower access

Similarities in the temperature contours of the CFD and thermal camera were seen (refer to Figure 10.3). It was also encouraging to measure the same temperatures with the camera and suction pyrometer as can be seen in Table 10.1.

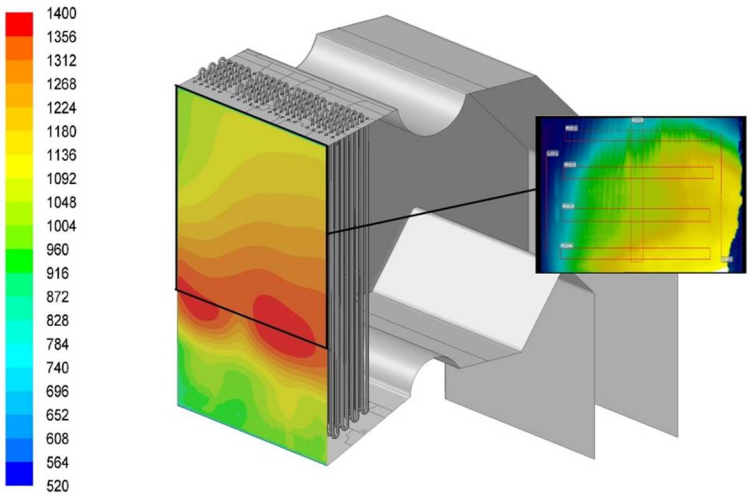

Figure 10.3: Temperature contours of thermal camera compared to CFD

Table 10.1: Comparison of CFD results, suction pyrometer measurements and thermal camera images.

	CFD	Suction pyrometer	Thermal camera (R1)
Upper level temperature in front of superheater [°C]	1020	1040	1055

Images taken with the Durag camera from the front wall towards the superheater showed the same flame profile as predicted by the CFD model with regards to temperature, shape and height (refer to Figure 10.4).

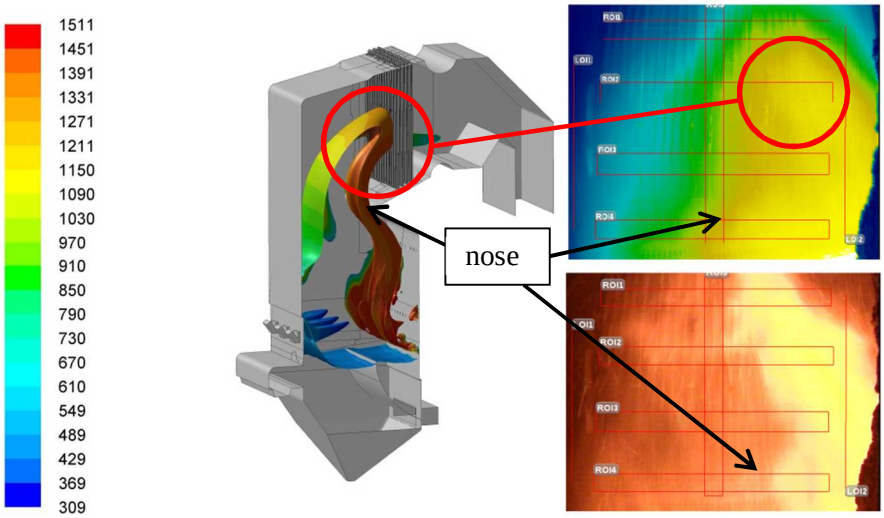

Figure 10.4: Flame profile of thermal camera compared to CFD

The flame is depicted as an iso-surface of 20 000 ppm carbon monoxide content in the combustion gas, as recommended by ANSYS. The gas temperature contours were then plotted on this surface. Images taken at grate-level indicate the same combustion intensity and temperatures on the rear wall at the lower secondary air nozzles in line with the spreaders (refer to Figure 10.5).

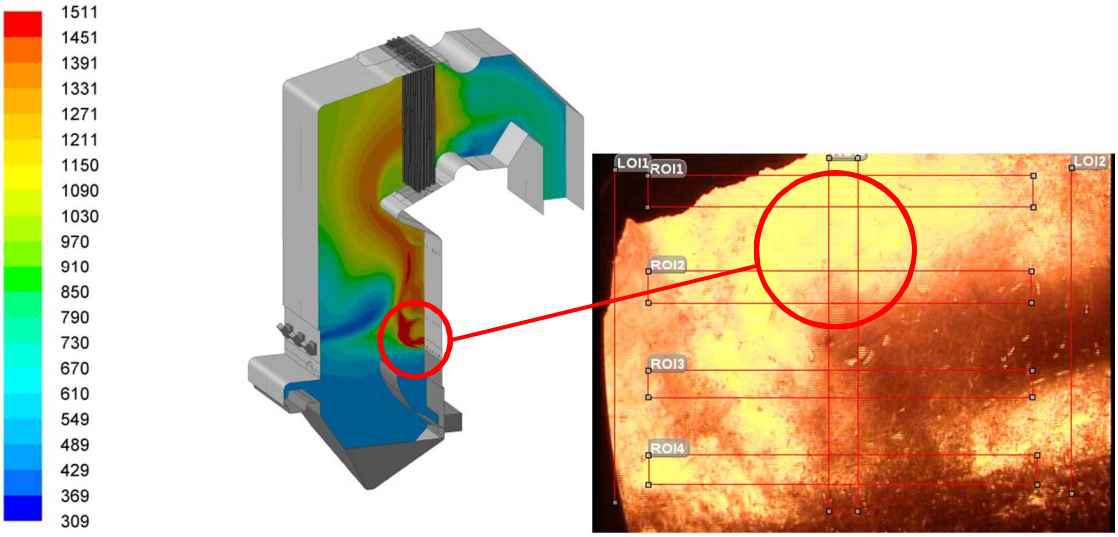

Figure 10.5: Thermography at grate-level vs CFD results

Drying of the bagasse takes place in front of the spreaders delaying de-volatilisation and combustion. There is a high level of turbulence due to the secondary air at the rear of the furnace. This results in more intense combustion with higher heat release and temperatures.

The focus of the third site visit was using the suction pyrometer for temperature traverses across the width of the boiler. These measurements corresponded well with the CFD results (see Figure10.6 and 10.7).

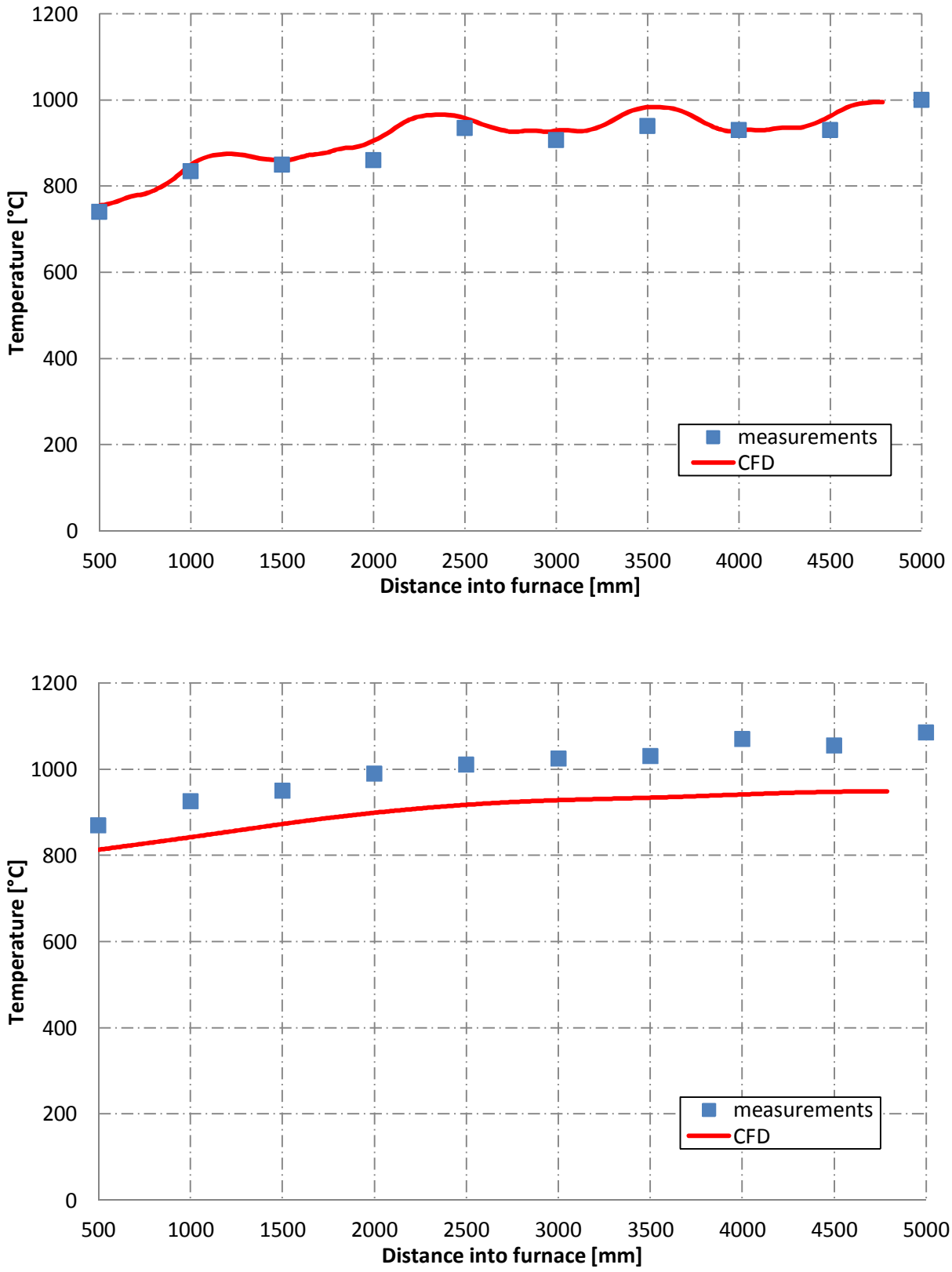

Figure 10.6: Temperature traverses taken across the width of boiler at top elevation before and after the superheater (graph at the top is behind the superheater)

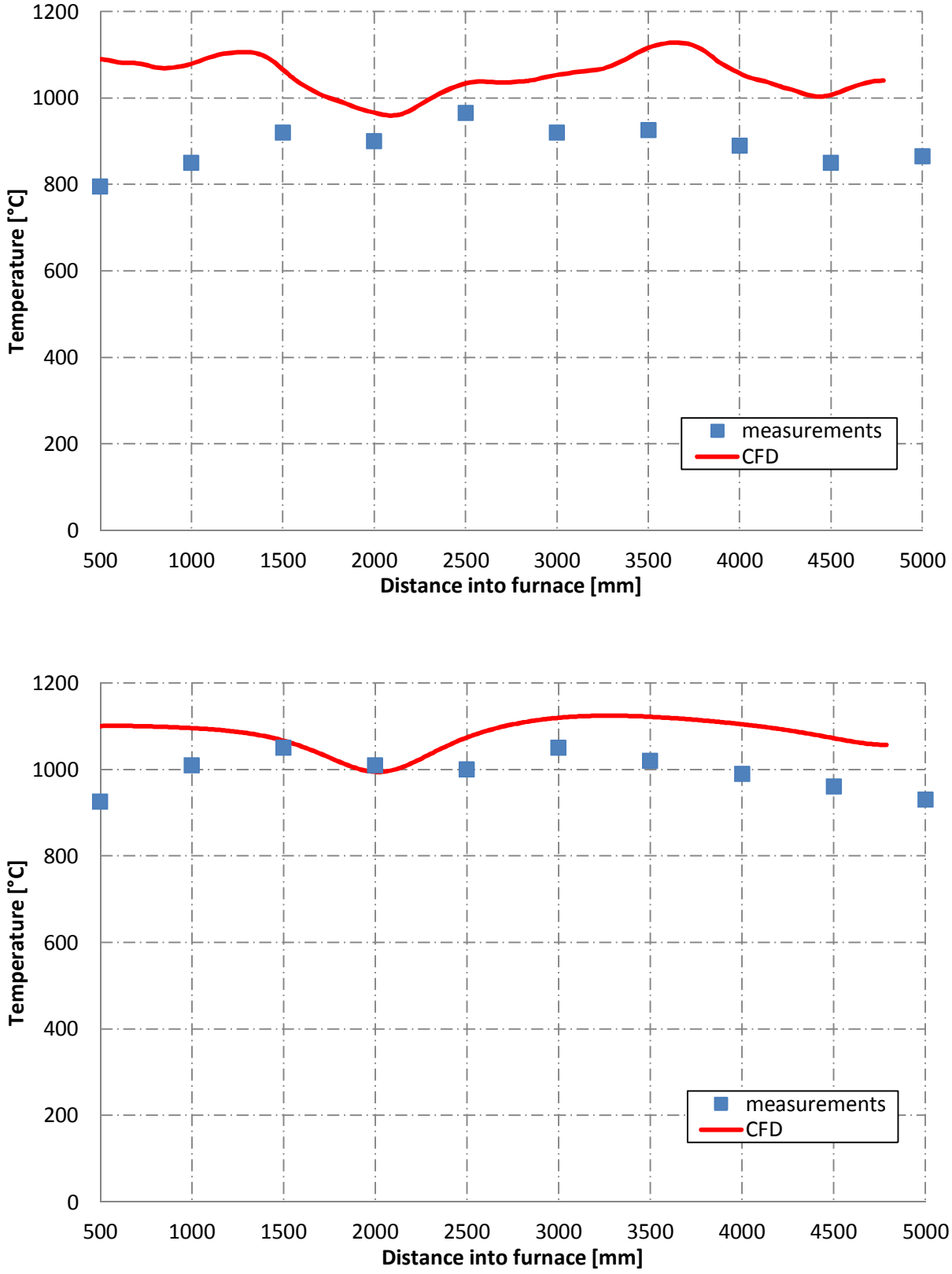

Figure 10.7: Temperature traverses across the width of boiler at bottom elevation before and after the superheater (graph at the top is behind the superheater)

In Figure 10.6 and 10.7 the measurements follow the trend of the CFD results well. The superheater elements are pitched at 200 mm, but at 3 locations there are gaps of 400 mm where the gas bypasses. At these locations the CFD predicts peaks which were also measured behind the superheater. In Figure 10.8 the image from the John Thompson camera was processed. This data also corresponds well with the peak flame temperature predicted by the CFD model.

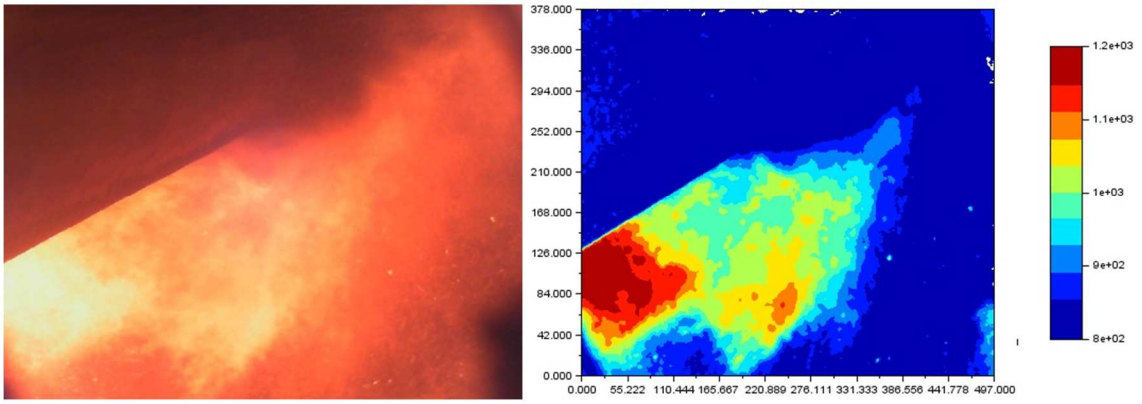

Figure 10.8: Image of JT camera from bottom soot blower access in front of superheater down onto flame ball

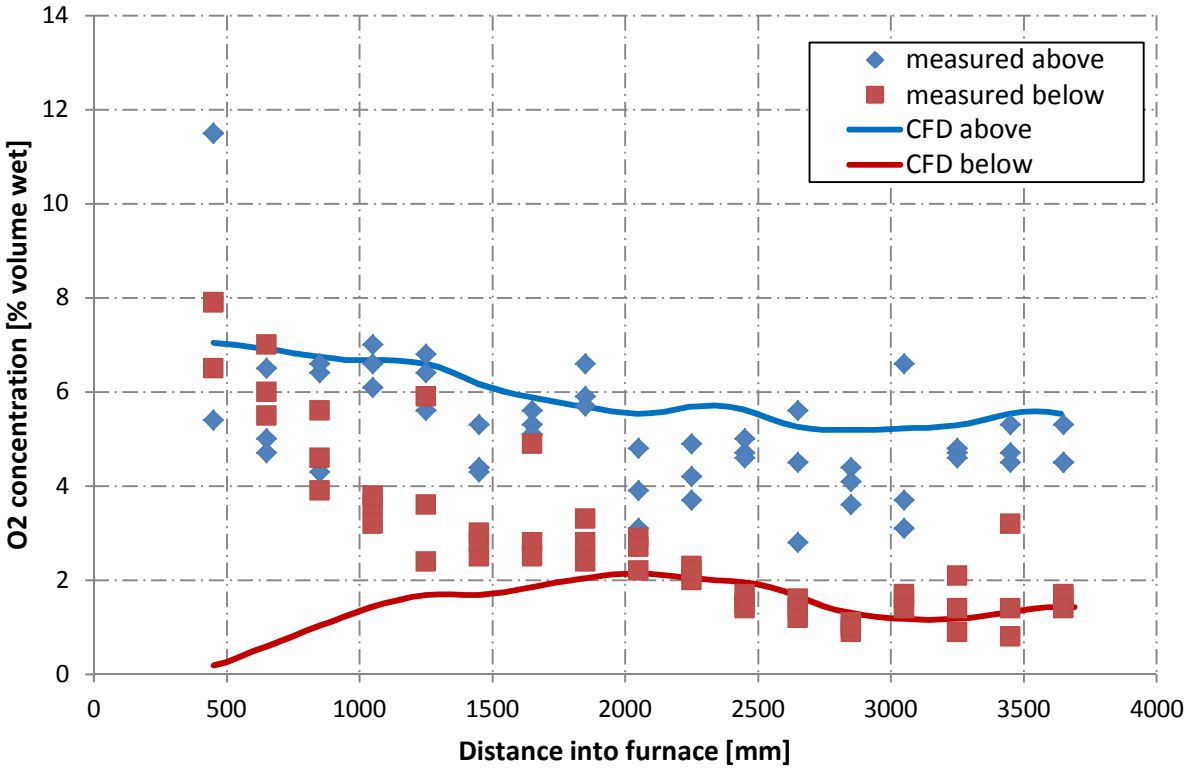

Figure 10.9: Oxygen concentration in the combustion gas at the top and bottom elevation behind the superheater

Considering the difficulty in measurement of the gas species and the fact that the CFD is a steady state average of transient phenomena, the comparison between the measured gas species and CFD

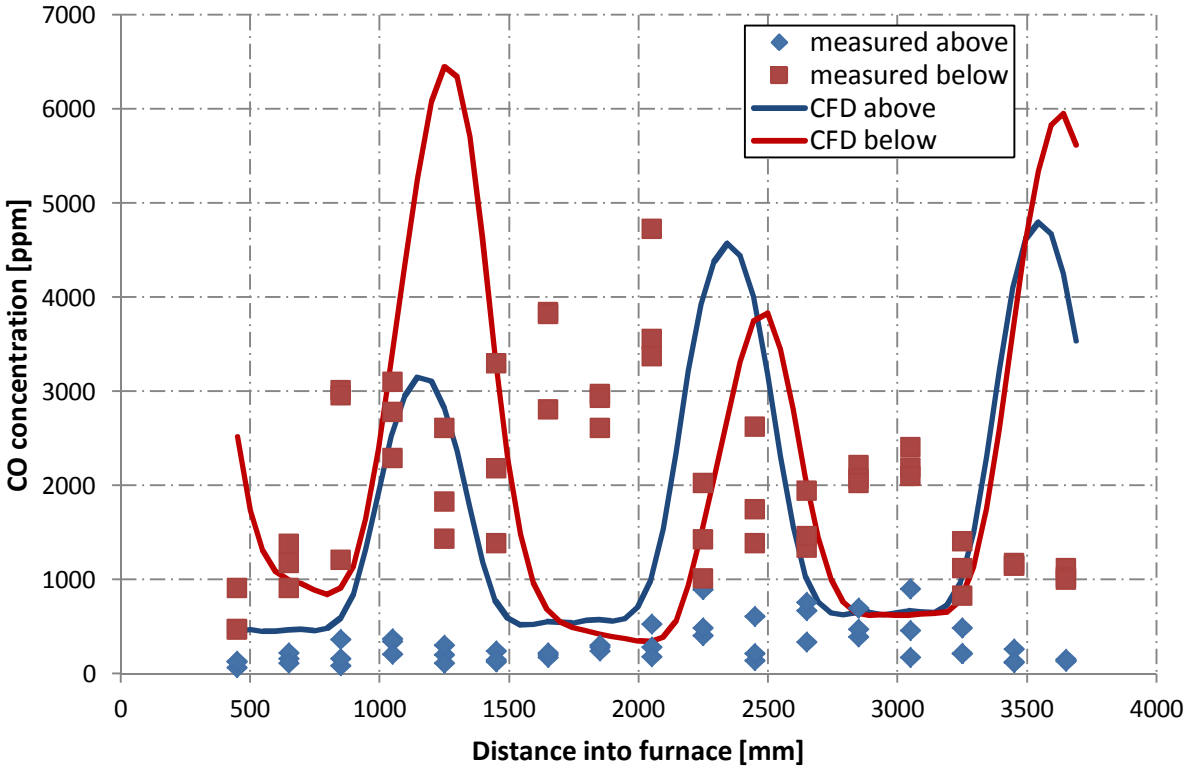

Figure 10.10: Carbon monoxide concentration at the top and bottom elevation behind the superheater

values is also good. See Figures 10.9 and 10.10 for the species measurements and CFD results in the location behind the superheater.

Prediction of steam temperature

As mentioned before, the main focus of the study was to predict the steam temperature accurately. A few important parameters are compared in Table 10.2. The steam temperature prediction from the CFD model was calibrated to the measured value by adjusting the fouling layer thickness. The combustion gas temperature at the mainbank outlet is slightly lower than the prediction of the CFD model, indicating that the heat exchanger model can be adjusted slightly.

Since the combustion of bagasse is very unstable, the CO varies. Bearing this in mind the CFD model predicts steady state combustion which corresponds well to the average value measured on site after the mainbank. The particle mass carry over measured by isokinetic sampling corresponds well with the CFD results, which indicates that the particle dynamics are good enough for the present study of superheater performance which focuses on heat transfer around the superheater.

Table 10.2: CFD vs site data, important parameters

		Measurements	CFD
Superheater steam temperature	[°C]	399	399
Combustion gas temperature at mainbank outlet	[°C]	422	426
Combustion gas CO concentration at mainbank outlet	[ppm]	200-1500	1202
Particle Mass Carry Over at mainbank outlet	[mg/Nm3]	6000-12000	6589

Comparison of results with the lumped parameter model

The CFD results were compared with the lumped parameter model in Appendix B. This is a very important part of the work as the lumped parameter model outputs are the basis of critical aspects of the boiler design e.g. grate area, furnace volume, furnace height, refractory arrangement, panel wall construction, superheater geometry, mainbank layout and heat recovery stack design.

If the accuracy of metal temperatures and heat fluxes could be improved it can lead to performance improvements considering e.g. natural circulation of the two-phase flow steam/water circuit or cost savings considering e.g. the pressure part design.

An initial comparison of the energy absorbed in the furnace, superheater and mainbank indicated that an unrealistically small amount of heat is absorbed by the furnace tube walls. This warranted a detailed mass and energy balance over the complete system in the CFD simulation. The outcome was that 38% of the total energy that need to be absorbed to reach the combustion gas outlet conditions could not be accounted for. This was reported to ANSYS® and after a substantial period of testing they confirmed an error with the software.

The error resulted in twice the energy reduction from the combustion gas due to the latent heat of evaporation. Since bagasse contains 50 % water it has a substantial effect for this case study. A work-around was implemented which resulted in the correct energy balance, an increase in steam temperature of 28°C and an overall increase of 235 °C when considering the contour plots of combustion gas temperature before and after the superheater. Therefore the effect of this error in ANSYS® Fluent is substantial for biomass containing large fractions of moisture. The error was corrected in version 15.0.7. All the results presented in this thesis include the work-around. Table 10.3 illustrates the difference between the CFD results and lumped parameter model with regards to important parameters.

Table 10.3: Comparison of CFD to lumped parameter analysis

		L Model	CFD
Energy :			
Heat absorbed in furnace	[kW]	21533	12107
Heat absorbed in superheater	[kW]	9167	9032
Convective heat transfer	[%]	58	67
Radiative heat transfer	[%]	42	33
Heat absorbed in superheater cavity	[kW]	254	1132
Heat absorbed in mainbank	[kW]	22173	29605
Sum Total	[kW]	53 127	51876
Temperature:			
Furnace gas outlet temperature	[°C]	977	966
Superheater gas outlet temperature	[°C]	825	951
Mainbank gas outlet temperature	[°C]	396	426
Superheater steam inlet temperature	[°C]	240	240
Superheater steam outlet temperature	[°C]	403	399
Velocity:			
Gas velocity superheater inlet	[m/s]	7	9

The amount of heat absorbed in the furnace of the CFD simulation is substantially lower than the lumped parameter model, indicating incomplete combustion at this point in the CFD model, since the lumped parameter model assumes complete combustion in the furnace.

However the furnace gas exit temperature is similar for both models. Therefore the difference in superheater gas outlet temperature between the two models is due to the energy release of the combustibles in the flue gas from the furnace outlet to the mainbank outlet. This heat of reaction can be quantified by the difference in heat absorbed between the mainbank and superheater cavity of the two models, a value of 8.3 MW. The fact that the boiler outlet conditions of the combustion gas are similar for both models confirms it.

The flame position of Figure 10.4 and CO measurements in Figure 10.10 correspond to the fact that there is still chemical reaction taking place. This is an important discovery for future designs involving heat fluxes on boiler components downstream from the furnace, since it could not be quantified in the past.

The fraction of convection heat transfer in the superheater of the CFD model is also higher than the lumped parameter model. This affects the performance of the superheater with load and is very important in the design of steam temperature control for future larger units at higher pressures.

There is considerably more heat absorbed in the superheater cavity in the CFD model compared to the lumped parameter model due to the chemical reactions taking place. This needs to be taken into consideration for high heat flux natural circulation furnace designs to prevent burn-out.

The higher velocity at the superheater inlet of the CFD model corresponds to the position of the flame which is not considered in the lumped parameter model and is important for fouling and erosion analysis.

This superficial comparison is limited by the information that can be extracted from the lumped parameter model; however a few important discoveries have already been made illustrating the benefits of the more detailed CFD model. Once the aspects of consideration from the CFD have been validated the information could potentially redefine boiler design.

Model sensitivity

As stated before, the primary objective of this study is to develop a physically consistent model that can predict the steam temperature from an industrial watertube boiler reliably. It must take all the aspects that influence this result into account with the corresponding sensitivity.

It was decided that the effect of boiler load on steam temperature is a good sensitivity test. This is a major shortcoming of the lumped parameter model and requires various correction factors depending on fuel, boiler geometry and load.

The results from the CFD model are compared with site data in Figure 10.11. Boiler data at various loads are scarce and tests cannot be conducted since it will disrupt the sugar mill production. Therefore substantial historical data had to be analysed in order to capture stable periods at reasonable combustion conditions. This resulted in a scatter of data.

It is clear from Figure 10.11 that the model captures the effect of boiler load on steam temperature both qualitatively and quantitatively. These part load results give confidence that the model can be applied to different size boilers at different firing conditions burning bagasse.

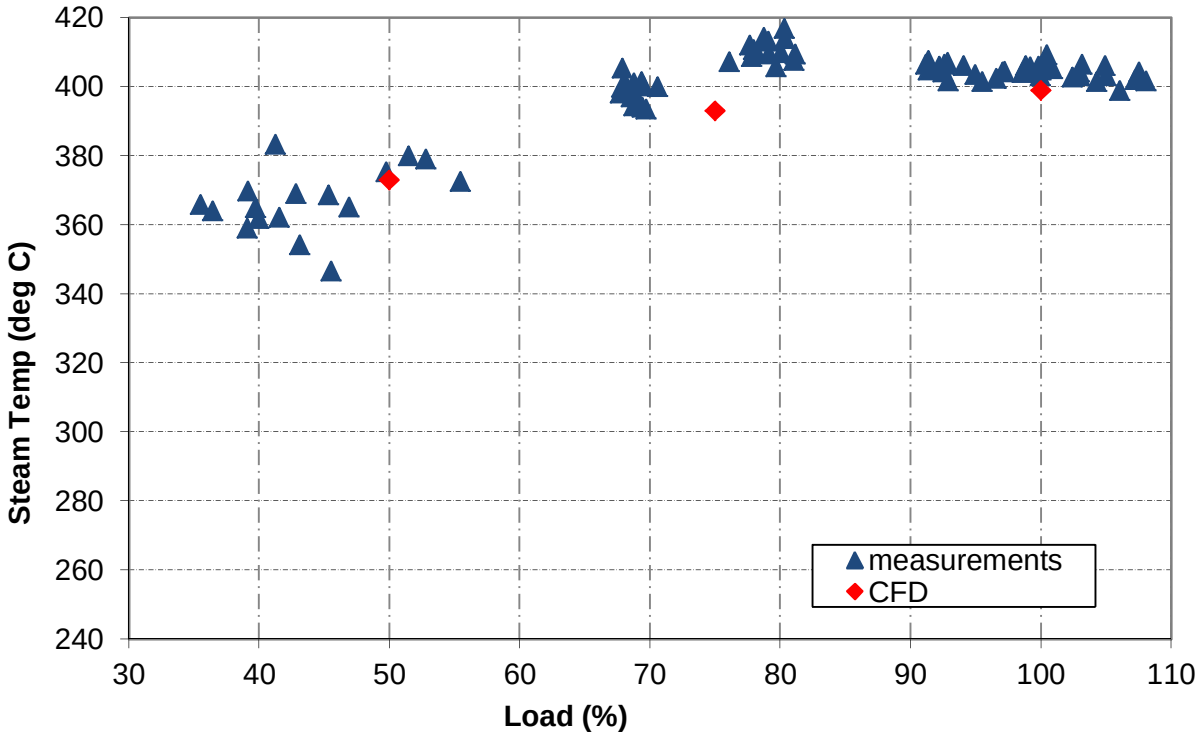

Figure 10.11: Steam temperature vs. load

This is seen as a major step forward for new superheater designs as an accurate prediction of load characteristic will result in substantial cost savings. It is common practice to oversize superheaters and control the steam temperature with e.g. water injection in order to maintain a constant characteristic. Using the CFD model the size of the superheater can be fine-tuned. At higher pressures where more exotic alloys are used, the size of controlled superheaters becomes even more important.

Practical implications of results from model

The traditional boiler design assumes complete combustion before the superheater. It has been shown that a considerable amount of heat is still released at this point in the boiler and even after the superheater. This can be seen in Chapter 6.

In the past the nose of the boiler has been designed taking only the water circulation into account considering angles, size and layout. The CFD model has shown the importance of the shape and size of the nose with regards to the flow.

There is a large re-circulation zone above the nose, as can be seen in Figure 10.12. Colder combustion gas from the rear is circulated back into the superheater, impacting the performance negatively. This is an important factor to consider especially for larger units at higher pressure as discussed in Appendix D.

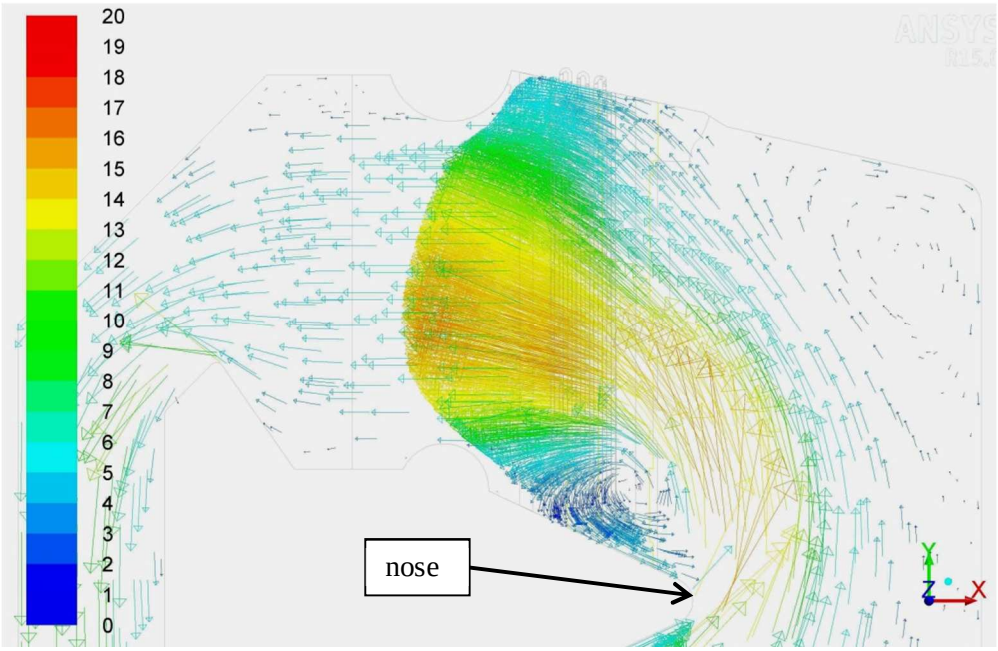

Figure 10.12: Velocity contours in m/s showing the recirculation zone above the boiler nose

In the past water circulation studies were conducted using average constant heat fluxes on the tube walls from the lumped parameter model. The CFD model has shown the distribution of heat on the walls following the shape of the flame (see Figure 10.13).

The heat flux distribution can now be used to assess water circulation much more accurately. Peak values are of concern when overheating is evaluated.

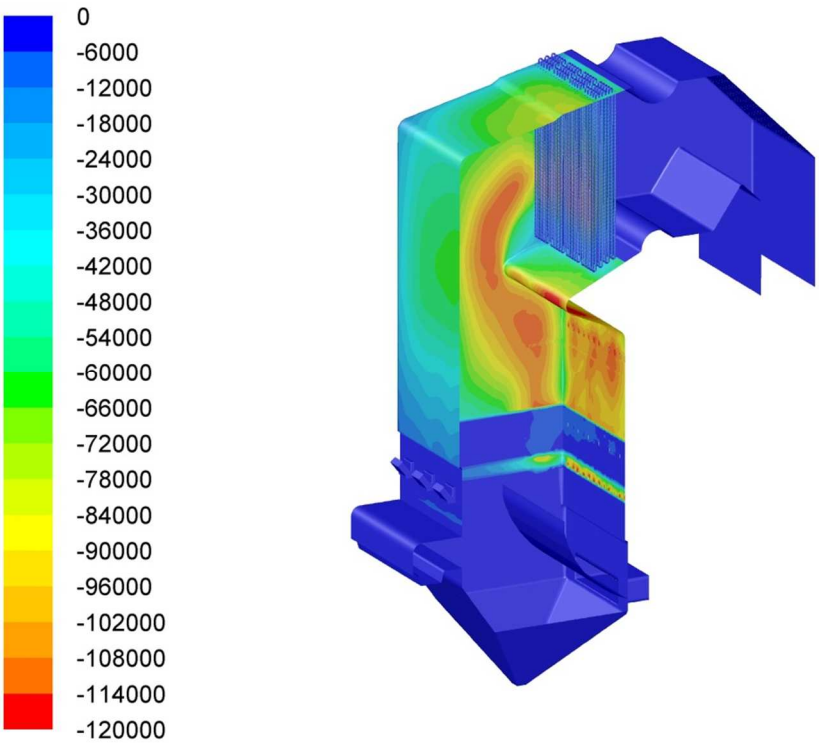

Figure 10.13: Heat flux distribution in boiler in kW/m^2

Secondary air systems were traditionally designed by trial and error following the basic guidelines of combustion namely enhancement of residence time, temperature and turbulence. The CFD model has shown that there is considerable room for improvement with regards to e.g. secondary air nozzle penetration into the furnace as shown in Figure 10.14.

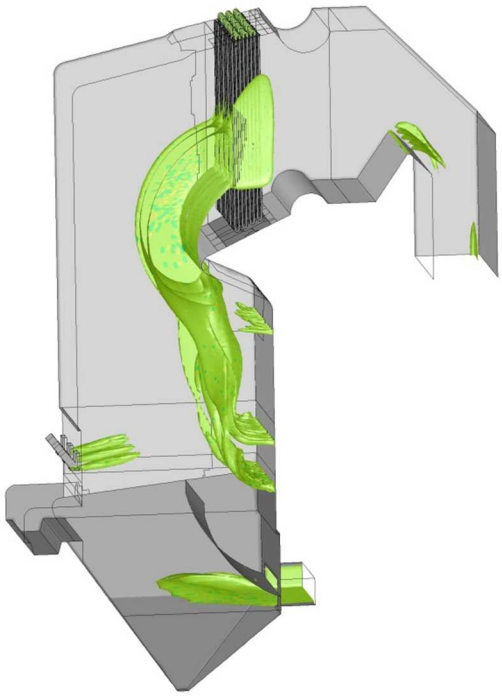

Figure 10.14: Secondary air jet furnace penetration at an iso-surface of 10 m/s

The residence time of the furnace was calculated in the past based on the gas volume flow only. The CFD model indicates that the particles spend a considerable larger amount of time in the furnace.

The benefits from the more detailed CFD model are clear from the new discoveries discussed. The first direct application of the model was to analyse a new superheater design.

As mentioned before, the current co-generation drive in the RSA led to the need for higher pressure, more efficient boilers. This presents challenges with e.g. new superheater designs and thus more detailed modelling is needed as steam temperature is critical in order to achieve the required turbine performance.

The methodology discussed in this thesis was applied to a new superheater design for an 80 bar pressure, 525°C steam temperature industrial boiler, discussed in Appendix D.

11. Conclusions and recommendations

11.1. Conclusions

CFD modelling of boilers have been done extensively although only a few research groups focused on bagasse firing exclusively.

While qualitative effects in boilers have been studied by numerous groups, quantitative results e.g. heat exchanger performance, are scarce due to the vast computational expense of implementing the complex physics on such a large scale at the required mesh resolution.

This thesis differs from what was done previously by focusing on quantitative results. Care was taken to achieve a balance between using empirical correlations to reduce cell count while at the same time capturing enough of the physical detail to achieve the required accuracy.

The total cell count of 25 million primarily due to the superheater region is the highest from the studies found in literature.

A physically consistent model of a bagasse fired boiler using the commercial CFD software package, ANSYS® Fluent, was developed. The heterogeneous and homogenous combustion with species transport after chemical reaction and associated heat transfer were accounted for.

The meshing scheme and resolution in the areas of interest was sufficient to capture enough detail for accurate heat transfer in the superheater region. The selection of turbulence model wall treatment and y^+ -value used on the superheater pipes are critical for convection heat transfer.

The Low-Reynolds-Number k-ε model of (Chang, Hsieh & Chen 1995) with a y^+ of 0.7 on the gas side tube wall produced the most accurate results compared to the empirical correlations of tube bank heat transfer.

The emissivities of the surfaces are also important as radiation accounts for 30 % of the heat transfer. Values based on the work of (Furmański 1995) produced realistic results.

A fouling thermal resistance had to be applied to correlate the model with actual conditions considering steam temperature. Using a thermal conductivity based on (Furmański 1995), the thickness of the layer applied was deemed realistic from years of experience in John Thompson.

An experimental campaign delivered measurements that corresponded well with the CFD results. The average CO and PM emissions in the combustion gas at the boiler outlet compared well with measurements. Locally temperature traverses in the combustion gas in front of and behind the superheater at 2 elevations captured the same trends and were close to the absolute values as predicted by the CFD results. It was determined that using a suction pyrometer is essential and standard thermocouples can deliver errors of 17 % in this application. CO and O_2 traverses in the combustion gas after the superheater indicated reasonable correlation to the CFD results.

Images from a thermal camera also corresponded well to the CFD results with regards to flame height and shape on superheater and grate level. The absolute values of temperature from the images also compared well to the CFD results and suction pyrometer data.

A comparison with the lumped parameter model revealed that more heat is absorbed in the mainbank of the CFD model and thus less in the furnace. The ratio of convection to radiation heat transfer in the superheater region is also higher for the CFD results. This has implications on the

natural circulation of the water side in the furnace and mainbank. It also influences the metal selection of the superheater.

Boiler load changes reacted realistically in the model, proving that the model is sensitive to the correct physics. The model can therefore capture detailed operational changes previously neglected by the lumped parameter methods.

The modelling methodology was used to design a new high pressure superheater. See Appendix D.

11.2. Recommendations

The bagasse particle drag and size distribution can be improved by incorporating the work of (Bernhardt 1993) on shape factors and (Rasul, Rudolph & Carsky 1999) on drag coefficients.

The grate nozzles can be modelled in detail to improve the accuracy of the bed model in terms of particle lift off and combustion.

Combustion kinetics of devolatilisation and homogenous gas phase reactions need to be verified with pilot plant testing. This is however of more importance to future work focusing on combustion involving e.g. ignition, extinction and lower temperature zones.

A LRN turbulence model capturing the same effects as Realizable k-ε in the core flow away from walls is required. This could result in more realistic results of combustion lower down in the boiler model, but also resolve the boundary layers of the superheater tubes accurately. The benefits of such an approach need to be confirmed with tests lower down in the boiler furnace.

Currently the model was calibrated using the site data available which are mainly the steam temperature, combustion gas temperature and species traverses in front of and behind the superheater at 2 elevations and mainbank gas exit conditions. The emissivity values were changed within realistic limits. Further testing, e.g. heat flux measurements can improve the realism of the heat distribution by determining the true emissivity values.

References

Abid, R 1991, 'A Two-Equation Turbulence Model for Compressible Flows', AIAA, Honolulu.

'Air Quality Act (ACT no. 39)' 2004, Department of Enviromental Affairs, South African Goverment.

Allmon, BA & Watson, GB 1991, 'Fouling and Cleaning of a Staggered, Finned Tube Bundle Under Coal-Fired Conditions', Research and Development Division, Babcock and Wilcox Company, Minneapolis.

ANSYS Inc. 2013, *FLUENT documentation*.

ASME 1974, *ASME PTC 4.1: Power test code - 4.1: Steam generating units*, ASME.

Baum, MM & Street, PJ 1971, 'Predicting the Combustion Behavior of Coal Particles', *Combust. Sci. Tech. 3(5)* , pp. 231–243.

Baxter, LL 1998, 'Influence of ash deposit chemistry and structure on physical and transport properties', Sciencedirect, Livermore.

Bernhardt, HW 1993, 'Shape factors of bagasse particles', *The South African Sugar Technologists Association*, Durban.

Boyd, RK & Kent, JH 1986, 'Three-dimensional furnace computer modelling', *21st Symp. (Int'l.) on Combustion. The Combustion Institute.*

British Standards Institution 1965, *BS 1339: Definitions, formulae and constants relating to the humidity of the air*, British Standards Institution, London.

British Standards Institution 1987, *BS 845-1: Methods for assessing thermal performance of boilers for steam , hot water and high temperature heat transfer fluids. Concise procedure*, BSI, London.

Buffalo Forge Company 1983, *Fan Engineering: An Engineer's Handbook on Fans and Their Applications*, 8th edn, Buffalo Forge.

Cengel, YA & Boles, MA 1994, *Thermodynamics An Engineering Apprach*, 2nd edn, McGraw-Hill, New York.

Chang, KC, Hsieh, WD & Chen, CS 1995, 'A Modified Low-Reynolds-Number Turbulence Model Applicable to Recirculating Flow in Pipe Expansion', *Journal of Fluids Engineering*, pp. 417-423.

Chen, HC & Patel, VC 1988, 'Near-Wall Turbulence Models for Complex Flows Including Separation', *AIAA Journal*, vol 26 , no. 6, pp. 641–648.

'Computational Fluid Dynamics In Waste-to-Energy Technology' 2003, Combustion Systems, Babcock & Wilcox Volund ApS, Esbjerg.

De Soete, GG 1975, 'Overall reaction rates of NO and N2 formation from fuel nitrogen', *Fifteenth Symposium (International) on Combustion, The Combustion Institute*, Pittsburgh.

de Souza-Santos, ML 2004, *Solid Fuels Combustion and Gasifiaction - Modeling, Simulation, and Equipment Operation*, Marcel Dekker, New York.

Dixon, TF 1994, 'SRI Internal Report'.

Dixon, T, A, M, Hobson, P, Plaza, F & Pennisi, S 2003, 'Application of CFD in the sugar industry', *Third International Conference on CFD in the Minerals and Process Industries*, Melbourne.

Dixon, TF, Mann, AP, Plaza, F & Gilfillan, WN 2005, 'Development of advanced technology for biomass combustion – CFD as an essential tool', *Fuel 84*.

Drummond, AF & Drummond, IW 1996, 'Pyrolysis of sugar cane bagasse in a wire-mash reactor', *Ind. Eng Chem Res*, pp. 1263-1268.

Dryer, FL 1972, 'High temperature oxidation of carbon monoxide and methane in a turbulent flow reactor', Arlington.

Fatehi, M & Kaviany, M 1994, 'Adiabatic reverse combustion in a packed bed', *Combustion Flame 99*, pp. 1-17.

Furmański, P 1995, 'Thermal and radiative properties of ash deposits on heat transfer surfaces of boilers', *Journal of power technologies. Vol 79*.

Gera, D, Mathur, M, Freeman, M & Robinson, A 1999, 'A Numerical Study of the Effects of Biomass Coal Cofiring on Unburnt Carbon and NOx Emissions', *American Flame Research Committee (AFRC) Fall Symposium*, San Francisco..

Gnielinski, V 1979, 'Equations for calculating heat transfer in single tuberows and banks of tubes in transverse flow', *Int Chem Eng 19(3)*, pp. 380–390.

Grimison, ED 1937, 'Correlation and utilization of new data on flowresistance and heat transfer for cross flow of gases over tube banks', *Trans. ASME 59*.

Haider, A & Levenspiel, O 1989, 'Drag Coefficient and Terminal Velocity of Spherical and Nonspherical Particles', *Powder Technology 58.*, pp. 63–70.

Henkes, RAWM, van der Flugt, FF & Hoogendoorn, CJ 1991, 'Natural Convection Flow in a Square Cavity Calculated with Low-Reynolds-Number Turbulence Models', *Int. J. Heat Mass Transfer. 34*, pp. 1543–1557.

Hossain, M, Lu, G & Yan, Y 2012, 'Measurement of Flame Temperature Distribution Using Optical Tomographic and Two-color Pyrometric Techniques', IEEE, Canterbury.

Howard, JB, Williams, GC & Fine, DH 1973, 'Kinetics of cabon monoxide oxidation in postflame gases', *14th Symposium on Combustion*, Combustion Institute (Ed.), Pittsburgh.

Huang, P, Bradshaw, P & Coakley, T 1993, 'Skin Friction and Velocity Profile Family for Compressible Turbulent Boundary Layers', *AIAA*, vol 31, no. 9, pp. 1600-1604.

Incropera, FP & De Witt, DP 1986, *Fundamentals of Heat and Mass Transfer*, John Wiley and Sons, New York.

Kader, B 1981, 'Temperature and Concentration Profiles in Fully Turbulent Boundary Layers', *Int. J. Heat Mass Transfer*, vol 24, no. 9, pp. 1541–1544.

Kim, SE, Choudhury, D & Patel, B 1997, 'Computations of Complex Turbulent Flows Using the Commercial Code ANSYS FLUENT', *The ICASE/LaRC/AFOSR Symposium on Modeling Complex Turbulent Flows*, Hampton, Virginia.

Kuo, KK 1986, *Principles of Combustion*, John Wiley and Sons, New York.

Kuznetsov, NW, Mitor, WW, Dubovski, IE & Karasina, ES 1973, 'Standards for Thermal Calculations of Power Boilers', *Energia.*

Launder, BE & Sharma, BI 1974, 'Application of the Energy Dissipation Model of Turbulence to the Calculation of Flow Near a Spinning Disk', *Letters in Heat and Mass Transfer*, vol 1, pp. 131-138.

Liptak, BG 1993, 'Pneumatic and Suction Pyrometers'.

Liu, G, Higgins, B, Sami, M & Kuehlert, K 2005, 'CFD modelling of an advanced overfired air system to reduce CO and NOx emission from a stoker-fired boiler'.

Lowery, GW & Vachont, RI 1974, 'The effect of turbulence on heat transfer from heated cylinders', *Int. J. Heat Mass Transfer*, pp. 1229-1242.

Luo, M & Stanmore, B 1992, 'Combustion Characteristics of Bagasse', *Australian Society of Sugar Cane Technologists*, St. Lucia.

Magnussen, BF & Hjertager, BH 1976, 'On mathematical models of turbulent combustion with special emphasis on soot formation and combustion', *16th Symp. (Int'l.) on Combustion. The Combustion Institute*.

Mann, AP 2012, 'Predicting the effects of fuel properties on combustion performance', *Conference of the Australian Society of Sugar Cane Technologists*, Bundaberg.

Mann, AP, Dixon, TF, Plaza, F & Joyce, A 2005, 'Oppertunities for Improving the Performance and Reducing the Costs of Bagasse-Fired Boilers', *XXV Congress of the International Society of Sugar Cane Technologists.*, Hogarth.

Mann, AP & O'Hara, MI 2012, 'Predicting the effects of bagasse depithing operations on boiler combustion performance', *34th Conference of the Australian Society of Sugar Cane Technologists*, Cairns.

McIntosh, MJ 1976, 'Mathematical model of drying in a brown coal mill system.1.Formulation of model', *Fuel 55*, pp. 47-52.

Miller, RS, Harstad, K & Bellan, J 1998, 'Evaluation of Equilibrium and Non-Equilibrium Models for Many Droplet Gas-Lquid Flow Simulations', *International Journal of Multiphase Flow* , pp. 1025-1055.

Mills, AF 1995, *Heat and mass transfer*, Irwin.

Miltner, M, Makaruk, A, Harasek, M & Friedl, A 2006, 'CFD-modelling for the combustion of solid baled biomass', *Fifth International Conference on CFD in the Process Industries*, Melbourne.

Murray, DB 1993, 'A Comparison of Heat Transfer in Staggered and Inline Banks with a Gas-Particle Crossflow ', *Experimental Thermal and Fluid Science*, no. 6, pp. 177-185.

Naude, DP, McIntyre, PJ & Field, J 1993, 'The design and operation of boiler plant utilising furfural residue as a fuel', *The South African Sugar Tecnologists Association.*.

Nebra, SA & Macedo, IC 1988, 'Bagasse particle shape and size and their free settling velocity', *Int. Sugar Journal 90*, p. 1077.

Ots, A 2011, 'Thermophysical properties of ash deposit on boiler heat exchange surfaces', *International Conference on Heat Exchanger Fouling and Cleaning*, Crete.

Paul Gothe 2013, 'Manual for Pyrometer', Bochum.

Rainey, T, O'hara, I, Mann, A, Bakir, H & Plaza, F 2012, 'Effect of depithing on the safety and inviromental aspects of bagasse stockpiling', *Process Safety and Enviromental Protection*.

Ranz, WE & Marshall, WR 1952, 'Evaporation from Drops, Part I and Part II', *Chem. Eng. Prog. 48(4)*, pp. 173–180.

Ranz, WE & Marshall, WR 1952, 'Vaporation from Drops, Part I ', *Chem. Eng. Prog. 48(3)*, pp. 141–146.

Rasul, MG, Rudolph, V & Carsky, M 1999, 'Physical properties of bagasse', *Fuel 78*, pp. 905-910.

Richter, W, Payne, R & Heap, MP, 'Influence of thermal properties of wall deposits on performance of P.F. fired boiler combustion chambers', Irvine.

Robinson, AL, Buckley, SG, Yang, N & Baxter, LL 2001, 'Exprimental measurements of the thermal conductivity of ash deposits: Part 2. Effects of Sintering and Deposit Microsctructure', *Energy & Fuels 15*, pp. 75-84.

Rogerson, JW, Kent, JH & Bilger, RW 2007, 'Conditional moment closure in a bagasse-fired boiler', *The Combustion Institute 31*.

Sazhin, SS 2006, 'Advanced Models of Fuel Droplet Heating and Evaporation', *Progress in Energy and Combustion Science*, pp. 162–214.

Scharler, R, Fleckl, T & Obernberger, I 2003, 'Modification of a Magnussen Constant of the Eddy Dissipation Model for biomass grate furnaces by means of hot gas in-situ FT-IR absorption spectroscopy', *Progress in Computational Fluid Dynamics, Vol. 3, No.s 2-4*.

Schiller, L & Nauman, AZ 1933, , *Ver. Deut. Ing 77*, pp. 318-320.

Shanmukharadhya, KS 2007, 'Simulation and Thermal Analysis of the Effect of Fuel Size on Combustion in an Industrial Biomass Furnace', *Energy & Fuels 21*, pp. 1895-1900.

Shanmukharadhya, KS & Sudhakar, KG 2007, 'Effect of Fuel Moisture on Combustion in a Bagasse Fired Furance', *Transactions of the ASME Vol 29*, pp. 248-253.

Shanmukharadhya, KS & Sudhakar, KG 2007, 'Experimental investigations for the location of reaction zones in a bagasse fired furnace', *Journal of Thermal Analysis and Calorimetry Vol 90*, pp. 299-306.

Shanmukharadhya, KS & Sudhakar, KG 2008, 'Experimental and numerical investigation of vortex-induced flame propagation in a biomass furnace with tangential over fire registers', *The Canadian journal of chemical engineering Vol 86*, pp. 43-52.

Sharan, H 1963, 'Correlations for heat transfer by non-luminous radiation between boiler flue gases and grey walls', *Fuel*, vol 36, pp. 263-272.

Shih, TH, Liou, WW, Shabbir, A, Yang, Z & Zhu, J 1995., 'A New k-epsilon Eddy-Viscosity Model for High Reynolds Number Turbulent Flows - Model Development and Validation', *Computers Fluids. 24(3)*, pp. 227–238.

Smith, IW 1982, 'Nineteenth Symposium (International) on Combustion. The Combustion Institute', Pittsburgh.

Spalding, DB 1970, 'Mixing and chemical reaction in steady confined turbulent flames', *13th Symp. (Int'l.) on Combustion. The Combustion Institute*.

Spang, B 2002, 'Excel Add-in for Properties of Water and Steam in SI-units ', Hamburg.

Stephan, P 2010, *VDI Heat Atlas*, Springer, Darmstadt.

Stubington, JF & Aiman, S 1994, 'Pyrolysis kinetics of bagasse at high heating rates', *Energy and Fuels 8*, pp. 194-203.

Tabakoff, W & Sugiyama, Y 1980, 'Experimental method of determining particle restitution coefficients', *Engineering Technology Conferences*, ASME.

Turns, SR 2011, *An Introduction to Combustion - Concepts and Applications*, McGraw-Hill, New York.

Versteeg, HK & Malalasekera, W 2007, *An Introduction to Computational Fluid Dynamics - The Finite Volume Method*, Pearson Education Limited, Essex.

White, F & Christoph, G 1971, 'A Simple New Analysis of Compressible Turbulent Skin Friction Under Arbitrary Conditions', AFFDL.

Wolfshtein, M 1969, 'The Velocity and Temperature Distribution of One-Dimensional Flow with Turbulence Augmentation and Pressure Gradient', *Int. J. Heat Mass Transfer*, vol 12, pp. 301–318.

Woodfield, PL, Kent, JH & Dixon, TF 2000, 'Computational modelling of combustion instability in bagasse-fired furnaces', *Experimental Thermal and Fluid Science 21*, pp. 17-25.

Woodfield, P, Kent, J, Vasily, N & Terry, D 1999, 'Prediction of unstable regimes in the operation of bagasse fired furnaces ', *Second International Conference on CFD in the Minerals and Process Industries* , Melbourne.

Yin, C, Kaer, SK, Rosendahl, L & Hvid, SL 2009, 'Modeling of pulverised coal and biomass co-firing in a 150kW swirling-stabilised burner and experimental validation', *International Conference on Power Engineering-09 (ICOPE-09)*, Kobe.

Zanzi, R, Sjostrom, K & Bjornbom, E 1995, 'Rapid Pyrolysis of Bagasse at High Temperature', *Third Asia-Pacific International Symposium on Combustion and Energy Utilisation*, Hong Kong.

Zukauskas, A 1972, 'Heat Transfer from Tubes in Crossflow', *Advanced Heat Transfer 8*, pp. 93-160.

Appendices

Appendix A: Boundary conditions calculations

The two major parameters required to specify the boundary conditions of the simulation are the fuel and air flow into the boiler at the specified operating conditions. The first step is to calculate the amount of air required per fuel burnt to reach the oxygen content measured in the flue gas. The stoichiometric amount of air per fuel is calculated using global combustion chemical reactions based on the fuel analysis. The excess air amount is increased until the required oxygen content is reached iteratively using a spread sheet. The amount of fuel burnt is calculated using an indirect efficiency method and the output of the boiler. The indirect efficiency is based on the fuel analysis; the oxygen content and temperature of the combustion gas measured after the last heat recover section in the boiler. Other constant factors taken into account are radiation and unburnt carbon losses. The output of the boiler is based on the steam flow at the pressure and temperature measured.

A.1 Basis

TSB Komati boiler #3

Fuel: Bagasse

Steam conditions:

Evaporation:	152 550 kg/h
Final steam pressure:	3163 kPa
Final steam temperature:	399 ^{o}C
Feed water temperature:	112 ^{o}C

Site conditions

Altitude	205 masl
Ambient air temperature	36 ^{o}C
Relative humidity	80 %

Bagasse fuel analyses

Proximate analysis (% by mass)

Moisture	47.06 %
Ash	3.41 %

Calorific values

Gross calorific value	9890 kJ/kg
Nett calorific value	8092 kJ/kg

Ultimate analysis (% by mass)

Carbon	24.07	%
Hydrogen	2.97	%
Oxygen	22.49	%
Moisture	47.06	%
Ash	3.41	%
	100	%

Brix = 0.02 kg/kg

A.2. Combustion reactions

Only global chemical reactions are considered. The equations indicate what substances are involved in the reaction and show the molecular proportions in which they take part. Each molecule has a molar mass. This molar mass is the sum of the atomic weights of the atoms composing the molecule. C, has a molar mass of 12.011; oxygen, O_2, has a molar mass of 2x15.999 = 31.999; hydrogen has a molar mass of 2x1.008 = 2.016; carbon dioxide, CO_2, has a molar mass of 12.011 + 2x15.999 = 44.010 and water, H_2O has a molar mass of 2x1.008+15.999=18.015

The following illustrates the two global chemical reactions involved in bagasse combustion:

	12.011kg		31.999kg		44.010kg	
Carbon	C	+	O_2	⟶	CO_2	+ Heat
			31.999/12.011		44.010/12/011	
	1kg		=2.664kg		=3.664kg	33MJ
	4.032kg		31.999kg		36.03kg	
Hydrogen	$2H_2$	+	O_2	⟶	2 H_2O	+ Heat
			31.999/4.032		36.03/4.032	
	1kg		=7.936kg		=8.936kg	142MJ

It is summarized in Table A.1.

Combustible	Reaction	kg O_2/ kg fuel	Products kg/kg fuel		Heat Release MJ/kg fuel
			CO_2	H_2O	
Carbon	$C+O_2 \rightarrow CO_2$	2.664	3.664	---	33
Hydrogen	$2H_2+O_2 \rightarrow 2H_2O$	7.936	---	8.936	142

Table A.1. Combustion reactions

The carbon loss for a wide range of moisture contents can be taken as 0.61 % by mass. Hence : Nett carbon = 24.07-0.61 = 23.46 % by mass. From Table A.1. the stoichiometric air required and products of combustion is calculated in Table A.2.

Constituent	Parts by mass [kg/kg]	Oxygen [kg/kg]	Product	Product mass [kg/kg]	Dry volume [m^3@ NTP]
Nett carbon	0.2346	0.62497	CO2	0.8596	0.4378
Carbon loss	0.0061	0	-		
Hydrogen	0.0297	0.2357	H2O	0.2654	
Sulphur	0	0	SO2	0	0
Nitrogen	0	0	N2	2.1040	1.6835
Oxygen	0.2249	0	-		
Moisture	0.4706	0	H2O	0.4706	
Ash	0.0341	0	-		
Total	1	0.86067		3.6996	2.1212

Table A.2. Stoichiometric oxygen required and products of combustion

Important values:

Mass of air required: $M_{air} = \frac{0.86067 - 0.2249}{0.232}$ = 2.740 kg/kg fuel

Mass of N_2 introduced = 2.74*0.768 = 2.104 kg/kg fuel

Theoretical flue gas mass produced = 3.6996 kg/kg fuel

From the Ideal Gas Law (PV=RT) and the universal gas constant R=8.314472 J/^{o}Kmol, it can be shown that the density at NTP (101.32 kPa and 0 ^{o}C) can be calculated from:

$$density = \rho = \frac{Mol.Wt.}{22.414} \qquad \text{kg/m}^3$$

We can thus determine the densities of the products of combustion at NTP:

$$\rho_{CO_2} = \frac{44.010}{22.414} = 1.9635 \text{ kg/m}^3 \qquad \rho_{H_2O} = \frac{18.015}{22.414} = 0.8037 \text{ kg/m}^3$$

$$\rho_{SO_2} = \frac{64.059}{22.414} = 2.8580 \text{ kg/m}^3 \qquad \rho_{N_2} = \frac{28.013}{22.414} = 1.2498 \text{ kg/m}^3$$

$$\rho_{air} = \frac{28.013(1-0.232) + 31.999(0.232)}{22.414} = 1.2911 \text{ kg/m}^3$$

Gas density @NTP = $\frac{3.6996}{2.1212 + \frac{0.2654 + 0.4706}{0.8037}} = 1.218$ kg/m^3

Mass of water produced = 0.2654+0.4706 = 0.736 kg/kg fuel

Mass of fuel converted to gaseous products = $1 - 0.0061 - 0.0341 = 0.9598$ kg/kg fuel

Excess air table

Barometric pressure at 205 masl = $P = 1.2 \times 10^{-11} \times (288 - 0.0065 \times 205)^{5.256} = 98.892$ kPa

Source: Kempes Engineers Year Book 1974 Vol II Page 222

Saturation pressure at specified 36 ^{o}C = 5.979 kPa (from steam tables)

Air moisture content may also be calculated from:

$$M_{H_2OInAir} = \frac{RH}{100} \times 0.622 \times \frac{P_s}{(P_{atm} - P_s)} \qquad \text{kg } H_2O\text{/kg dry air}$$

Where:	$M_{H_2OInAir}$	= Moisture content in air	kg H_2O/kg dry air
	RH	= Relative humidity	%
	P_{atm}	= Barometric pressure	kPa absolute
	P_s	= saturation pressure of water vapour at dry bulb temperature	kPa abs

Note: 0.622 = ratio of molar mass of water and dry air = $\frac{18.015}{28.963}$

(British Standards Institution 1965) and (Buffalo Forge Company 1983)

Specified relative humidity = 80 %

H2O content in air = $M_{H_2OInAir} = \frac{80}{100} \times 0.622 \times \frac{5.979}{(98.892 - 5.979)} = 0.032$ kg H_2O/kg dry

Furnace

XS air = 32.8 %

Mass of dry air = $M_{DryAir} = 1.328 \times 2.74 = 3.638$ kg/kg fuel burnt

Mass of moisture with dry air = $M_{H_2OAir} = 3.638 \times 0.032 = 0.116$ kg/kg fuel burnt

Mass of wet product = $M_{Wet\,Prod} = 0.9598 + 3.638 + 0.116 = 4.7138$ kg/kg fuel burnt

Volumetric % of O_2 on dry basis = $V_{O_2Dry} = 21 \times (1 - \frac{1}{1.328}) = 5.19$ % V/V

Volume of theoretical flue gas mass = $V_{Theo} = \frac{3.6996}{1.218} = 3.0374$ m^3/kg fuel burnt

Volume of moisture in theoretical dry air = $V_{H_2OInAir} = \frac{0.032 \times 2.74}{0.8037} = 0.109$ m^3/kg fuel burnt

Volume of excess dry air = $V_{XSAir} = \frac{\frac{32.8}{100} \times 2.74}{1.2911} = 0.696$ m^3/kg fuel burnt

Volume of moisture in excess air = $V_{H_2O} = \frac{32.8}{100} \times 0.109 = 0.0358$ m^3/kg fuel burnt

Volume of O_2 in excess air = $V_{O_2} = 0.696 \times 0.21 = 0.1462$ m^3/kg fuel burnt

Volumetric % of O_2 on wet basis = $V_{O_2Wet} = 100 \times \frac{0.1462}{3.0374 + 0.109 + 0.696 + 0.0358} = 3.77$ % V/V

Mainbank

XS air = 32.8 % + 2 % = 34.8 % (infiltration allowance of 2%)

Mass of dry air = $M_{DryAir} = 1.348 \times 2.74 = 3.694$ kg/kg fuel burnt

Mass of moisture with dry air = $M_{H_2OAir} = 3.694 \times 0.032 = 0.118$ kg/kg fuel burnt

Mass of wet product = $M_{Wet\,Prod} = 0.9598 + 3.694 + 0.118 = 4.7718$ kg/kg fuel burnt

Volumetric % of O_2 on dry basis = $V_{O_2Dry} = 21 \times (1 - \frac{1}{1.348}) = 5.42$ % V/V

Volume of theoretical flue gas mass = $V_{Theo} = \frac{3.6996}{1.218} = 3.0374$ m^3/kg fuel burnt

Volume of moisture in theoretical dry air = $V_{H_2OInAir} = \frac{0.032 \times 2.74}{0.8037} = 0.109$ m^3/kg fuel burnt

Volume of excess dry air = $V_{XSAir} = \frac{\frac{34.8}{100} \times 2.74}{1.2911} = 0.739$ m^3/kg fuel burnt

Volume of moisture in excess air = $V_{H_2O} = \frac{34.8}{100} \times 0.109 = 0.038$ m^3/kg fuel burnt

Volume of O_2 in excess air = $V_{O_2} = 0.4952 \times 0.21 = 0.155$ m^3/kg fuel burnt

Volumetric % of O_2 on wet basis = $V_{O_2 Wet} = 100 \times \frac{0.155}{3.0374 + 0.109 + 0.739 + 0.038} = 3.95$ % V/V

The value of 3.95% above corresponds with average measurements on site after the mainbank during the duration of the test. Therefore the mass of air injected into the furnace is 3.754 kg/kg fuel. The same calculations are performed for the airheater and economizer sections and summarized in the excess air Table A.3. below:

Area	Excess air ratio	Mass of Dry Air [kg/kg]	Mass of H_2O with air [kg/kg]	V/V % Dry O_2	Mass of wet product [kg/kg]	V/V % Wet O_2
Furnace	1.328	3.638	0.116	5.19	4.714	3.77
Mainbank	1.348	3.694	0.118	5.42	4.772	3.95
Economiser	1.368	3.748	0.12	5.65	4.83	4.13

Table A.3. Excess air and corresponding O_2

A.3. Heat load

Final steam conditions: 399 °C at 3163 kPa
Feedwater conditions: 112 °C at 4500 kPa
From steam tables:

Enthalpy steam = $h_s = 3224.8$ kJ/kg

Enthalpy water = $h_w = 473.05$ kJ/kg

Heat load at 152 550 kg/h = $M = \frac{152550 \cdot (3224.8 - 473.05)}{3600 \cdot 10^3} = 116.605$ MW

A.4. Efficiency calculation

The final gas temperature after the last heat recovery section of the boiler measured on site is 191 °C. From the combustion reactions and the excess air table at the final gas condition after the economiser, the gas composition (in mass percentages) can be calculated:

$CO_2 = \frac{0.8596}{4.83} = 0.178$ $N_2 = \frac{2.1040}{4.83} = 0.4356$ $H_2O = \frac{0.856}{4.83} = 0.1772$

$Air = \frac{(3.748 - 2.74)}{4.83} = 0.209$ (Check: 0.178 + 0.4356 + 0.1772 + 0.209 = 1.000)

The composition of the dry gas is found from:

$CO_2 = \frac{0.178}{1 - 0.1772} = 0.2163$ $N_2 = \frac{0.4356}{1 - 0.1772} = 0.5294$ $Air = \frac{0.209}{1 - 0.1772} = 0.254$

4.1 Dry gas loss

The mean specific heat for the components found in flue gas can be determined from:

$$\text{Property} = A + Bt + Ct^2 + Dt^3$$

where t = gas temperature in °C.

Component	A	B	C	D
		Mean specific heat, kJ/kg°C		
CO_2	0,819372	$5{,}24968 \times 10^{-4}$	$-2{,}7566 \times 10^{-7}$	$6{,}1792 \times 10^{-11}$
N_2	1,03768	$1{,}410147 \times 10^{-6}$	$1{,}20329 \times 10^{-7}$	$-4{,}59217 \times 10^{-11}$
O_2	0,908963	$1{,}42472 \times 10^{-4}$	$-2{,}01556 \times 10^{-9}$	$-1{,}39593 \times 10^{-11}$
H_2O	1,85076	$1{,}32829 \times 10^{-4}$	$2{,}39327 \times 10^{-7}$	$-9{,}0209 \times 10^{-11}$
H_2	14,29387	$6{,}5992 \times 10^{-4}$	$-4{,}76564 \times 10^{-7}$	$3{,}01067 \times 10^{-10}$
Air	1,00269	$3{,}4628 \times 10^{-5}$	$8{,}94269 \times 10^{-8}$	$-3{,}63247 \times 10^{-11}$
SO_2	0,594236	$3{,}2344 \times 10^{-4}$	$-1{,}5249 \times 10^{-7}$	$2{,}7831 \times 10^{-11}$

The specific heat of the flue gas is determined from the summation of the products of the mass fraction of each component by its respective specific heat at the relevant temperature, or:

$$c_p = \sum_k m_k \cdot c_k$$

with:

c_p = mean specific heat of the flue gas in kJ/kg°C
m_k = mass fraction of the flue gas component in kg/kg
c_k = mean specific heat of the flue gas component in kJ/kg°C

(Stephan 2010)

Specific heat dry gas at 191 °C = $cp_{tg} = 1.0056$ kJ/kg°C

Specific heat dry gas at 36 °C (ambient) = $cp_{ta} = 0.9857$ kJ/kg°C

Mass of dry gas = $M_d = 4.83 - 0.856 = 3.974$ kg/kg

$$Loss_{DryGas} = \frac{3.974x100}{9890}\left(1.0056*191 - 0.9857*36\right) = 6.292\ \%$$

4.2 Wet gas loss

Mass of water produced = $M_w = 0.736$ kg/kg

Enthalpy water vapour at 191 °C and 0,10 bar absolute = $h_{wg} = 2862$ kJ/kg

Heat content water at ambient conditions = $h_a = 4.19x36 = 150.84$ kJ/kg

$$Loss_{WetGas} = \frac{0.736x100}{9890}\left(2862 - 150.84\right) = 20.176\ \%$$

4.3 Moisture in air loss

Mass of moisture in air = $M_{MoistInAir} = 0.12$ kg/kg

Saturation vapour pressure under ambient conditions = $p_{ws} = 5.979$ kPa absolute

Relative humidity = $\varphi = 80$ %

Partial pressure water vapour = $p_w = 0.80x5.979 = 4.7832$ kPa absolute

Enthalpy water vapour at 191 °C = $h_{moistg} = 2862$ kJ/kg

Enthalpy water vapour at 36 °C = $h_{moista} = 2550$ kJ/kg

$$Loss_{MoistInAir} = \frac{0.12x100}{9890}(2862 - 2550) = 0.379\ \%$$

4.4 Unburnt loss

Carbon loss = C_{Loss} = 0.0061

$$Loss_{UnburntC} = \frac{0.0061x33820x100}{9890} = 2.086\ \%$$

4.5 Radiation loss

The basic efficiency loss from radiation at ABMA reference conditions of:
28 °K differential temperature between cladding and ambient temperatue
0,51 m/s wind velocity and 0,95 emissivity can be written as:

$(a + b \times \ln(M) + c \times (\ln(M))^2 + d \times (\ln(M))^3)$

% radiation loss = $F_1 \times F_2 \times F_3 \times e$

where: M = gross boiler output in MW (heat to steam)
a = 1.5551 b = -0,72889
c = 4,4410 x 10^{-2} d = -1,4924 x 10^{-4}

F_1 is a correction factor for temperature differences and/or wind velocities different from the ABMA reference conditions and can be calculated from:

$F_1 = T \times (a + bT + cV + dVT)$

Where: T = temperature differential in °C
V = air velocity in m/s
a = 2,8766 x 10^{-2} b = 6,7708 x 10^{-5}
c = 9,7636 x 10^{-3} d = 5,0479 x 10^{-6}

Temp\Velocity	0,51 m/s (Std)	1 m/s	5 m/s	10 m/s	15 m/s
28 °C (Std)	1	1,13	2,25	3,63	5,02
40 °C	1,46	1,66	3,25	5,25	7,24

Calculated factors F_1 – Standard conditions are recommended

F_2 is a correction factor for the number of cooled furnace walls and can be found from:

F_2 = 1 – 0,063 x Number of water-cooled walls or 1 – 0,033 x Number of aircooled walls

# of walls	1	2	3	4
Water	0,94	0,88	0,81	0,75
Air	0,97	0,93	0,90	0,87

F_3 is a correction factor for partial load and is defined as:

F_3 = 100 / load as % of MCR

(ASME 1974)

$$Loss_{RadStd} = e^{\left(1.5551-0.72889\cdot\ln(116.6)+4.441\cdot10^{-2}\cdot\left(\ln(116.6)\right)^2-1.4924\cdot10^{-4}\cdot\left(\ln(116.6)\right)^3\right)} = 0.397$$

Correction factors:
Standard conditions: $F_1 = 1$
Four water-cooled furnace walls: $F_2 = 0.75$
100 % of MCR: $F_3 = 0.983$

$$Loss_{Rad} = 1x0.75x0.983x0.397 = 0.293$$

4.6 Unaccounted loss

$$Loss_{UnAcc} = 0.5$$

Total losses = 6.292+20.176+0.379+2.086+0.29+0.5 = 29.723

Efficiency on GCV = $\eta_{GCV} = 100 - 29.723 \cong 70.3$

Efficiency on NCV = $\eta_{NCV} = \frac{9890}{8092} \cdot 70.3 = 85.9$

E.5. Fuel parameters

Heat required from fuel on GCV = $\frac{116.6}{0.703} = 165.86$ MW

Fuel burnt = $\frac{165.86 \cdot 1000 \cdot 3600}{9890} = 60374$ kg/h

Appendix B: Lumped parameter boiler model of TSB Komati

B.1. Furnace Black Body Surface Area (BBSA)

The furnace consists of sections of panel wall and refractory covered panel wall. The tube diameter is 76.2 mm OD at 100mm pitch with a welded carbon steel strip between the tubes. The refractory is casted at 120mm thick onto the panels in certain areas.

The projected areas of the different sections of the furnace walls are calculated and then multiplied by factors for panel wall and refractory covered panels. These areas are summated in order to calculate the total black body surface area (BBSA).

Note: Since the furnace configuration has a radiant (unscreened) superheater, the projected area of the superheater entrance plane does not form part of the BBSA. The heat absorbed through this plane forms part of the superheater calculation.

Hence, BBSA for the furnace calculation = 447.2 m^2.

B.2. Furnace and superheater calculations

The following design information is given:

B.2.1 Furnace

Black body surface area = 447.2 m^2 (see B.1. above)
Furnace emissivity factor = 0.72 (bagasse firing)
Saturated steam temperature = 241 ^oC (furnace pressure assumed at 3300 kPa)
Furnace tube wall temperature = 241 + about 20 ^oC, 261 ^oC
Undergrate air : 85% of total combustion air at 186 ^oC (air exit temperature from the airheater)
Secondary air (including spreader air): 15% of total combustion air at 36 ^oC (ambient temperature).

B.2.2 Superheater cavity data

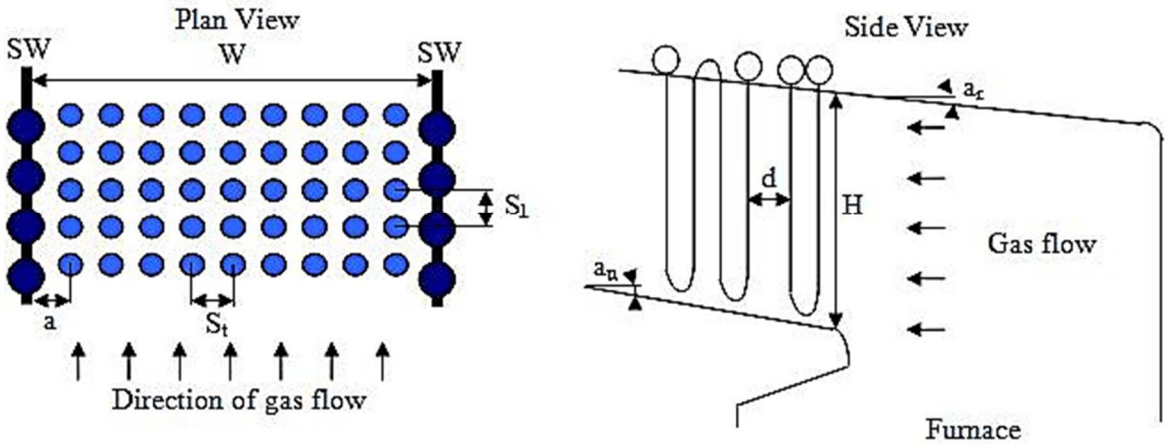

Upper nose angle a_n	= 25 ^{o}
Roof angle a_r	= 12.5 ^{o}
Superheater entry height H	= 6456 mm
Width between sidewalls W	= 9700 mm

B.2.3 Steam flow diagram

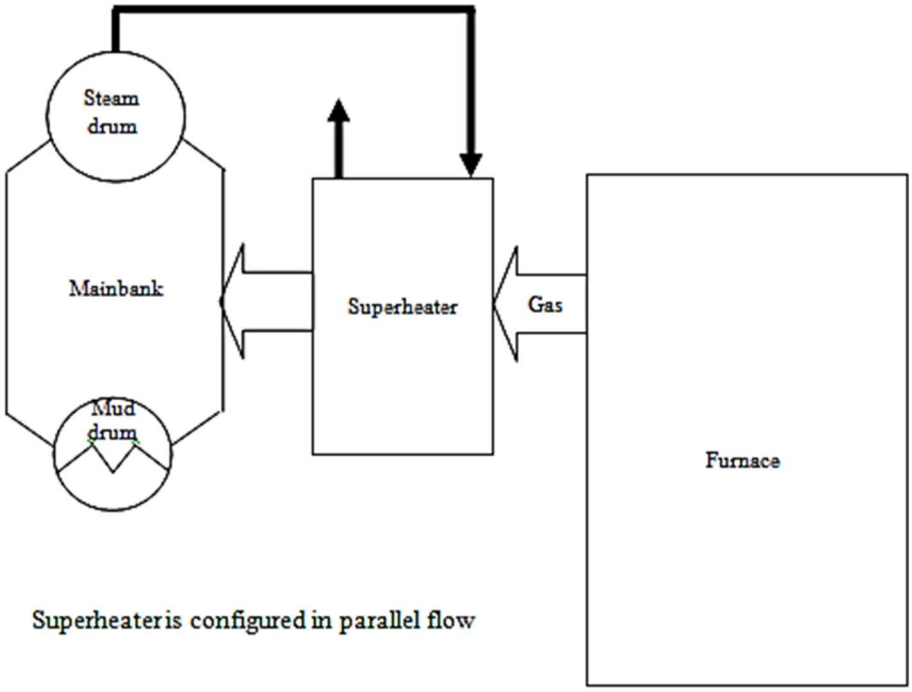

B.2.4 Geometrical data for the superheater

Description	
Tube outside diameter in mm	63.5
Tube thickness in mm	4.06
Number of transverse tubes	40
Longitudinal pitch S_l in mm	127
Transversal pitch S_t in mm	236
Number of rows in the direction of the gas flow	8
Number of parallel steam paths	40
Superheater to sidewall distance a in mm	250
Direct radiation factor f_r	0.41
Fouling factor for convection f_c	0.93

B.2.5.Calculation of preliminary values

Depth into cavity for the superheater:

D = *(number of longitudinal rows -1)*S_l*

= *(8-1)*127 = 889 mm*

Height of the cavity at exit of superheater:

H_{ex} = $H - D_{sec} * tg(a_n - a_r)$

= *6456 – 889*tg(25-12.5) = 6259 mm*

Average height of the superheater:

H_{av} = $(H + H_{ex})/2$

= *(6456 + 6259)/2 = 6358 mm*

Area of the cavity around the superheater:

$$A_{cav} = \left(WD\ (\frac{1}{\cos(a_r)} + \frac{1}{\cos(a_n)}) + H_{av} D\ 2 \right) * 10^{-6}$$

$$= \left(9700 * 889 * (\frac{1}{\cos(12.5)} + \frac{1}{\cos(25)}) + 6358 * 889 * 2 \right) * 10^{-6} = 29.7\ \text{m}^2$$

Heat transfer area of the superheater:

$$A = H_{av} \pi OD\ (\#long.rows)(\#trans.rows) * 10^{-6}$$

$$= 6358 * \pi * 63.5 * 8 * 40 * 10^{-6} = 405.8\ \text{m}^2$$

Planar area of the superheater at inlet:

$A_{plan} = HW*10^{-6} = 6456*9700*10^{-6} = 62.6\ \text{m}^2$

Gas mass flow M_g = fuel burnt * mass of wet products = 60374 * 4.714 = 284603 kg/h

Gas free area superheater = $A_f = H_{av}(W - OD\ (NumberOfTransversTubes) * 10^{-6}$

$$= 6358 * (9700 - 63.5 * 40) * 10^{-6} = 45.5\ \text{m}^2$$

Gas mass flux superheater = $G_c = \frac{M_g}{A_{f\,\text{sec}} * 3600} = \frac{284603}{45.5 * 3600} = 1.74\ \text{kg/m}^2\text{s}$

Steam free area superheater = $A_{fSt} = \frac{(NumParSteamPaths)\pi(OD\ - 2Th\ )^2}{4 * 10^6}$

$$= \frac{40 * \pi * (63.5 - 2 * 4.06)^2}{4 * 10^6} = 96.35 * 10^{-3} \text{ m}^2$$

Steam flux superheater = $\frac{Evaporation}{A_{fSt} * 3600} = \frac{152550 kg/h}{96.35 * 10^{-3} * 3600} = 439.8$ kg/m^{2}s

Mean beam length of the cavity for the superheater:

$$MBL_{cec} = \frac{0.85a\ S_l * 10^{-3}}{(S_l + \frac{\pi OD}{2})} = \frac{0.85 * 250 * 127 * 10^{-3}}{(127 + \frac{\pi * 63.5}{2})} = 0.119 \text{ m}$$

Hydraulic diameter =Dh_{cav} = 0.119/0.85=0.14m

Mean beam length of the superheater:

$$MB_c = \frac{0.85 * 4(S_t S_l - \frac{\pi OD^2}{4})}{\pi OD} * 10^{-3}$$

$$= \frac{0.85 * 4 * (236 * 127 - \frac{\pi * 63.5^2}{4})}{\pi * 63.5} * 10^{-3} = 0.457 \text{ m}$$

Luminous radiation absorbed in superheater:

S_t/OD = 236/63.5 = 3.72 and number of rows= 8
From JT curve: percentage radiation passing through = 13
Hence : % absorbed =100 – 13 = 87%

Luminous radiation absorbed in first row:

S_t/OD = 236/63.5 = 3.72 and number of rows= 1
From JT curve: percentage radiation passing through = 56
Hence : % absorbed =100 – 63 = 37%

B.2.6. Total heat input into the furnace

Heat from the fuel Q_f = $\frac{(1 - \frac{Loss_{UnburntC}}{100}) * NCV * FuelBurnt}{3600}$

$$= \frac{(1 - \frac{2.086}{100}) * 8092 * 60374}{3600} = 132876 \text{ kW}$$

Specific heat of wet air at ambient temperature (36^{o}C) = 1.031 kJ/kg^{O}C
Specific heat of wet air at 186 ^{o}C = 1.040 kJ/kg^{O}C

Heat from hot air Q_{air}= $\frac{0.85 * (3.638 + 0.116) * (186 * 1.040 - 36 * 1.031) * 60374}{3600}$

= 8365 kW

Total heat input into furnace = *HeatIn* = 132876 + 8365 = 141241 kW

B.2.7. Calculation of furnace exit temperature of 977 °C

The formula is based on the Stefan-Boltzmann relationship for radiative heat transfer:

$$Q_{rad} = \frac{20.41 \cdot F_r \cdot BBSA}{FB} \cdot \left\{ \left(\frac{t_e + 273}{100} \right)^4 - \left(\frac{t_w + 273}{100} \right)^4 \right\}$$

Where:

Q_{rad}	= heat transferred to the furnace by radiation	kJ/kg fuel burnt
20.41	= Stefan-Boltzmann constant	kJ/hm^2°K^4
F_r	= correction factor for geometry and emissivity	
BBSA	= black body surface area	m^2
FB	= mass of fuel burnt	kg/h
t_e	= gas temperature at the exit of the furnace	°C
t_w	= furnace wall temperature	°C

The furnace wall temperature for a tube carrying a mixture of water and steam is usually taken as 20 °C above saturation temperature.

Heat in the gases leaving the furnace

$$Q_{gas} = M_{Wet\,Prod} \cdot \left(c_{pt_e} . t_e - c_{pta} \cdot ta \right)$$

Where:

Q_{gas}	= heat in gases leaving the furnace	kJ/ kg fuel burnt
$M_{WetProd}$	= mass of flue gas produced (from XS air table)	kg/kg fuel burnt
c_{pt_e}	= specific heat of the gas at temperature t_e	kJ/kg°C
t_e	= gas temperature at the exit of the furnace	°C
c_{pta}	= specific heat at ambient air temperature	kJ/kg°C
ta	= ambient air temperature	°C

Summary:

The equation to establish the exit gas temperature from the furnace becomes:

$$Q_f + Q_{air} = Q_{rad} + Q_{gas}$$

Or

$$\left(1 - \frac{Loss_{UnburntC}}{100} \right) \cdot NCV + M_{HotAir} \cdot (c_{pt} \cdot t - c_{ta} \cdot ta) =$$

$$\frac{20.41 \cdot F_r \cdot BBSA}{FB} \cdot \left\{ \left(\frac{t_e + 273}{100} \right)^4 - \left(\frac{t_w + 273}{100} \right)^4 \right\} + M_{Wet\,Prod} \cdot (c_{pt_e} \cdot t_e - c_{pta} \cdot ta)$$

The equation is best solved by trial and error using assumed values for t_e.

Furnace corrected emissivity factor for bagasse = F_r = 0.72

Heat transferred to the furnace walls:

$$Q_{furn} = \frac{5.67 F_r * BBSA * \left[\left(\frac{t_g + 273}{100} \right)^4 - \left(\frac{t_w + 273}{100} \right)^4 \right]}{1000} = \frac{5.67 * 0.72 * 447.2 * \left[\left(\frac{1250}{100} \right)^4 - \left(\frac{348}{100} \right)^4 \right]}{1000}$$

= 44303 kW

The steam inlet temperature of the superheater, is 241°C:

$$t_1 = 241 \ ^{o}\text{C}$$

From steam tables:
Steam enthalpy at inlet of superheater = H_{in} = 2803 kJ/kg (241°C & 3300kPa)
Steam enthalpy at outlet of superheater = H_{out} = 3234 kJ/kg (403°C & 3163kPa)

Next, calculate the steam temperature in the first tube row and from this the direct radiant heat coming from the furnace.

Assume a steam outlet temperature in the first row of say t_1 + 30 = 241 + 30 = 271 °C

Log mean steam temperature in the first row $LMst = \frac{271 - 241}{\ln(\frac{271}{241})} = 256^{o}\text{C}$

The emissivity factor F_r for direct radiation in the superheater can be taken as 0.53 and a JT correction factor of 0.41.
Heat absorbed by the superheater from radiation:

$$Q_{rad} = \frac{0.41 * 5.67 * F_r * A_{plan} * \left[\left(\frac{t_{GasIn} + 273}{100} \right)^4 - \left(\frac{LMst + 273}{100} \right)^4 \right]}{1000} * \left(\frac{\%absorbed}{100} \right)$$

$$= \frac{0.41 * 5.67 * 0.53 * 62.6 * \left[\left(\frac{977 + 273}{100} \right)^4 - \left(\frac{256 + 273}{100} \right)^4 \right]}{1000} * \left(\frac{87}{100} \right) = 1585 \ \text{kW}$$

Total heat absorbed by the steam:

$$Q_{11} = \frac{Evaporation * (H_{out} - H_{in})}{3600} = \frac{152550 * (3234 - 2803)}{3600} = 18264 \ \text{kW}$$

Balance of the heat transferred by non-luminous radiation and convection:

$$Q_{left} = Q_{11} - Q_{rad} = 18264 - 1585 = 16679 \ \text{kW}$$

Specific heat of the gas at t_{GasIn} = c_{pGasIn} = 1.294 kJ/kg°C
Heat in gas at the inlet of the superheater:

$$Q_{GasIn} = \frac{M_g t_{GasIn} c_{pGasIn}}{3600} = \frac{284603 * 977 * 1.294}{3600} = 99946 \ \text{kW}$$

Heat in gas at the outlet of the superheater, without compensating for heat transferred to the cavity =

$$Q_{GasOut} = Q_{GasIn} - Q_{left} = 99946 - 16679 = 83267 \ \text{kW}$$

$$c_{GasOut}t_{GasOut} = \frac{83267*3600}{284603} = 1053 \text{ kJ/kg}$$

By trial and error we can find that this correlates to t_{GasOut} = 831 °C

Log mean gas temperature = $LMGT = \frac{(977-831)}{\ln(\frac{977}{831})} = 902$ °C

Cavity wall temperature = t_{cav} = 261 °C

Log mean temperature difference = $LMTD = \frac{977-831}{\ln\left[\frac{977-261}{831-261}\right]} = 640$ °C

Dynamic viscosity of gas at $LMGT = \mu = 45.881 * 10^{-6}$ kg/ms
Specific heat of gas at $LMGT = c_p$ = 1.282 kJ/kg°C

Convective coefficient $h_c = 0.161 * Dh_{cav}^{-0.2} G^{0.8} \mu^{0.2} c_p$

$= 0.161 * 0.14^{-0.2} * (1.74 * 3600)^{0.8} * (45.881 * 10^{-6})^{0.2} * 1.282 / 3.6$

= 12.6 W/m^2°C

For flue gas: $P_{pp} = \sqrt{P_h(P_h + P_c)}$

Where P_h is the partial pressure of water vapour in kPa
P_c is the partial pressure of carbon dioxide in kPa

$$Y = P_{pp} L_{mb}$$

$$h_r' = P_x \left[\frac{t_g + 71{,}5 - 28{,}5\frac{\ln(64X)}{\ln(2)}}{1271{,}5 - 28{,}5\frac{\ln(64X)}{\ln(2)}} \right] * 1{,}163 \text{ W/m}^2\text{°K}$$

where P_x = 10,248755 + 259,0015X – 521,4298X^2 + 583,836X^3
- 303,8581X^4 + 58,109X^5

X = Y * altitude correction factor / 101,325

t_g = Mean bulk gas temperature in °C

For a tube wall temperature $t_w \leq 300$ °C:

$$K_t = K_{t1} = \left[\frac{T_g^4 - T_w^4}{T_g^4 - 573^4} \right] \left[\frac{t_g - 300}{t_g - t_w} \right]$$

where $T_g = t_g + 273$
$T_w = t_w + 273$

For $300 < t_w < 600$ °C:

$$K_t = K_{t2} = 1 + (0{,}73K_{t1} - 0{,}719)\left(\frac{1100}{t_g}\right)^{0{,}25}$$

$h_r = K_t \; h_r'$ in W/m^2 °K.

(Sharan 1963)

With a mean beam length of 0.119m we can calculate:
Radiative coefficient h_r = 16.43 W/m^2°C

The external fouling factor f_o = 0.93
Hence the overall heat transfer coefficient =

$$U = f_o * (h_c + h_r) = 0.93 * (12.6 + 16.43) = 27 \text{ W/m}^2\text{°C}$$

Heat transferred to the cavity = $Q_{cavSec} = \frac{U * A_{cav} * LMTD}{1000} = \frac{27 * 29.7 * 640}{1000} = 513$ kW

We can now adjust the heat taken from the gas to 16524+513=17037 kW which will result in a different gas exit temperature.
The above calculations can then be repeated and the gas outlet temperature adjusted until it correlates with the heat transferred to the cavity.
The result of this gives a gas exit temperature from the superheater of t_{GasOut} = 825 °C

We can now calculate the convective and non-luminous radiation heat transfer coefficients for the superheater.

Log mean gas temperature = $LMGT = \frac{(977 - 825)}{\ln(\frac{977}{825})} = 899$ °C

Log mean steam temperature $LMst = \frac{403 - 241}{\ln(\frac{403}{241})} = 315$ °C

With a mean beam length of 0.457 m we can calculate:
Radiative coefficient h_r = 34.63 W/m^2°C

Calculate the convective heat transfer coefficient in accordance with the VDI method:
The Nusselt number can be calculated from the equations below.

$$Nu = f_a \; x \; Nu_1$$

$$Nu_1 = 0{,}3 + \sqrt{(Nu^2_{lam} + Nu^2_{turb})}$$

with

$$Nu_{lam} = 0{,}664 \; x \; Re_\psi^{1/2} \; x \; Pr^{1/3}$$

$$Nu_{turb} = \frac{0{,}037\, Re_{\psi}^{0,8}\, Pr}{1 + 2{,}443\, Re_{\psi}^{-0,1}\left(Pr^{2/3} - 1\right)}$$

The Nusselt, Reynolds (*Re*) and Prandtl (*Pr*) numbers are defined as $h_c L/k$, $LG/(\psi\mu)$ and $c_p\mu/k$ respectively with:

h_c = convective heat transfer coefficient in W/m^{2o}C

L = wetted length in m

= $\pi x\, OD / 2$

OD = tube outside diameter in m

ψ = area correction factor

= $1 - \pi / 4a$ for $b \geq 1$

= $1 - \pi / 4ab$ for $b < 1$

k = thermal conductivity of the gas in W/m^{o}C

G = gas mass flux in the free area (<u>without</u> tubes) in kg/m^{2}s

μ = dynamic viscosity of the gas in kg/ms

c_p = true specific heat of the gas in J/kg^{o}C

The gas properties are to be calculated at the average gas temperature defined as:

$\theta_{av} = (\theta_I + \theta_o) / 2$ in ^{o}C

with θ_I = gas inlet temperature in ^{o}C

θ_o = gas outlet temperature in ^{o}C

The arrangement factor is calculated from :

$f_a = 1 + 0{,}7 \text{ x } (b/a - 0{,}3) / [\psi^{1,5} \text{ x } (b/a + 0{,}7)^2]$ for in line tube arrangement

For less than ten rows the following correction factor can be applied:

$Nu = [1 + (n - 1)*f_a] \text{ x } Nu_1 / n$

with n = number of longitudinal rows and < 10

$$a = \frac{S_t}{OD} = \frac{236}{63.5} = 3.72 \qquad \text{and} \qquad b = \frac{S_l}{OD} = \frac{127}{63.5} = 2$$

Area correction factor $\psi = 1 - \pi / 4a = 1 - \pi / 4 * 3.72 = 0.79$

Wetted length = $L = \pi * OD / 2 = \pi * 0.0635 / 2 = 0.1\,\text{m}$

Average gas temperature = $\theta_{av} = (\theta_i + \theta_o) / 2 = (977 + 825) / 2 = 901$ ^{o}C

Gas mass flux in free area (no tubes) = $G = 284603 / (3600 * 6.358 * 9.7) = 1.282$ kg/m^{2}s

Dynamic viscosity of gas = μ = 45.852 * 10^{-6} kg/ms

Reynolds number = $\text{Re}_{\psi} = \frac{L * G}{\psi * \mu} = \frac{0.1 * 1.282}{0.79 * 45.852 * 10^{-6}} = 3539$

True specific heat of the gas at $\theta_{av} = 1.43$ kJ/kg^{o}C

Thermal conductivity of the gas at $\theta_{av} = 0.102$ W/m^{o}C

Prandtl number $\Pr = 1.43*1000*45.852*10^{-6} / 0.102 = 0.643$

$$Nu_{lam} = 0.664 * \mathrm{Re}_{\psi}^{1/2} * \Pr^{1/3} = 0.664 * 3539^{1/2} * 0.643^{1/3} = 34.09$$

$$Nu_{turb} = \frac{0.037 * 3539^{0.8} * 0.643}{1 + 2.443 * 3539^{-0.1} * (0.643^{2/3} - 1)} = 22.66$$

$$Nu_1 = 0.3 + \sqrt{34.09^2 + 22.66^2} = 41.2$$

$$f_a = 1 + 0.7 * (2/3.72 - 0.3) / \left[0.79^{1.5} * (2/3.72 + 0.7)^2\right] = 1.15$$

Corrected for 8 rows deep: $Nu = [1 + (8-1) * 1.15] * 41.2/8 = 46.6$

Convective heat transfer coefficient $h_c = 46.6 * 0.102 / 0.1 = 47.5$ W/m^{2o}C

Outside heat transfer coefficient $h_o = f_o * (h_r + h_c) = 0.93 * (34.63 + 47.5) = 76.38$ W/m^{2o}C

The following steam properties can be determined @ *LMst and the average steam pressure*:
Thermal conductivity k = 50.5*10^{-3} W/m^{o}C
Specific heat c = 2536 J/kg^{o}C
Dynamic viscosity μ = 20.6*10^{-6} kg/ms

The internal heat transfer coefficient can be determined from:

$$h_i = 0.023 * ID^{-0.2} * k^{0.6} * G^{0.8} * c^{0.4} * \mu^{-0.4}$$

where
h_i = internal heat transfer coefficient in W/m^{2o}C
ID = internal diameter in m
G = steam flux in kg/m^{2}s
Hence,

$$h_i = 0.023 * \left(\frac{63.5 - 2*4.06}{1000}\right)^{-0.2} * \left(\frac{50.5}{1000}\right)^{0.6} * 439.8^{0.8} * 2536^{0.4} * \left(\frac{20.6}{10^6}\right)^{-0.4} = 1534 \text{W/m}^{2o}\text{C}$$

Overall heat transfer coefficient = $U = \frac{1}{\frac{1}{h_o} + \frac{1}{h_i}} = \frac{1}{\frac{1}{76.38} + \frac{1}{1534}} = 72.8$ W/m^{2o}C

We can now calculate the heat transferred to the first row:

Log mean temperature differential = $LMTD = \frac{(271 - 241)}{\ln\left(\frac{977 - 241}{977 - 271}\right)} = 721$ ^{o}C

Heat transferred to the first row from convection and non-luminous radiation:

$$Q_{ConvRow1} = U * \left(\frac{A}{\#long.rows}\right) * LMTD / 1000 = 72.8 * \left(\frac{405.8}{8}\right) * 721/1000 = 2662.5 \text{ kW}$$

Heat transferred to the first row from direct radiation:

$$Q_{radRow1} = \frac{0.41 * 5.67 * F_r * A_{plan} * \left[\left(\frac{t_{GasIn} + 273}{100}\right)^4 - \left(\frac{LMst + 273}{100}\right)^4\right]}{1000} * \left(\frac{\%absorbedfirstrow}{100}\right)$$

$$= \frac{0.45*5.67*0.53*62.6*\left[\left(\frac{977+273}{100}\right)^4 - \left(\frac{315+273}{100}\right)^4\right]}{1000} * \left(\frac{37}{100}\right) = 663 \text{ kW}$$

Total heat to first row: $Q_{Row1} = 2662.5 + 663 = 3326$ kW

Hence the enthalpy of the steam increased in the first row to:

$$2803 + \frac{3326}{\frac{152550}{3600}} = 2883 \text{ kJ/kg}$$

From the steam tables this corresponds to a steam outlet temperature in the first row of 263 °C.
This differs slightly from the assumed steam temperature in the first row of 271 °C on page 88.
If the difference is substantial then a new temperature has to be assumed and the above calculation repeated.

We now calculate the total heat transferred from the gas over the total superheater.
Heat transferred from convection and non-luminous radiation:

$$LMTD = \frac{977 - 241 - 825 + 403}{\ln\left(\frac{977-241}{825-403}\right)} = 565 \text{ °C}$$

$$Q_{Conv} = 72.8*405.8*565/1000 = 16691.4 \text{ kW}$$

From page 88 : $Q_{rad} = 1585$ kW

Total heat transferred to superheater $Q = 16691.4 + 1585 = 18276$ kW

Increase in steam enthalpy over the superheater = $\frac{18276}{\left(\frac{152550}{3600}\right)} = 431$ kJ/kg

Enthalpy steam at superheater outlet =2803 + 431 = 3234 kJ/kg
Steam temperature at superheater outlet ± 403 °C

This is similar to the assumed value of 403 °C and reiteration is not required. The end result in this case for the superheater:

Heat transferred $Q_{sec} = 18276$ kW

Gas exit temperature $t_e = 825$ °C

Steam outlet temperature $t_{ost} = 403$ °C

This result is also very close to the 399 °C measured on site.

Appendix C: Tube bank convection heat transfer

The published results of (Murray 1993) and (Zukauskas 1972) were used to verify the convection heat transfer of the boiler simulation in isolation from the combustion and related phenomena.

The method of calculating cross flow heat transfer and pressure drop over tube banks from the VDI Warmte Atlas (Stephan 2010) based on the work of (Gnielinski 1979) was also researched and implemented in Microsoft® Excel to compare to the results of the afore mentioned authors.

Murray

(Murray 1993) investigated heat transfer in staggered and in-line tube banks with gas particle cross flow. The literature published included the experimental setup (Figure C1 and C2) and data on heat transfer coefficients over the bank, per row and local around the tubes.

The flow patterns through the bank can be seen in Figure C.3 and clearly indicates the stagnation point on the first tube, boundary layer separation at the side of the tube and flow reattachment on the side of the next tube.

These characteristics are typical examples of non-equilibrium boundary layers and important to consider for the near wall treatment of the turbulence model used in the boiler simulation.

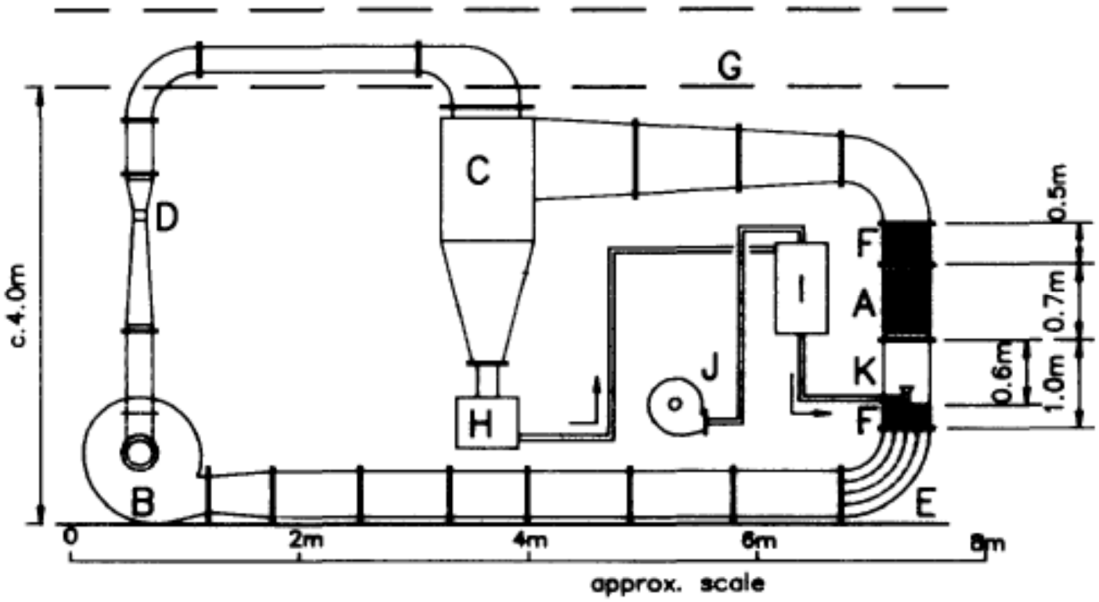

Figure C.1: Schematic diagram of testing facility. A, test section; B, centrifugal fan; C, cyclone; D, venturi meter; E, vanes; F, honeycomb; G, false ceiling; H, airlock and solids storage hopper; I, solids feed hopper; J, auxiliary blower; K, solids feed cone (Murray 1993)

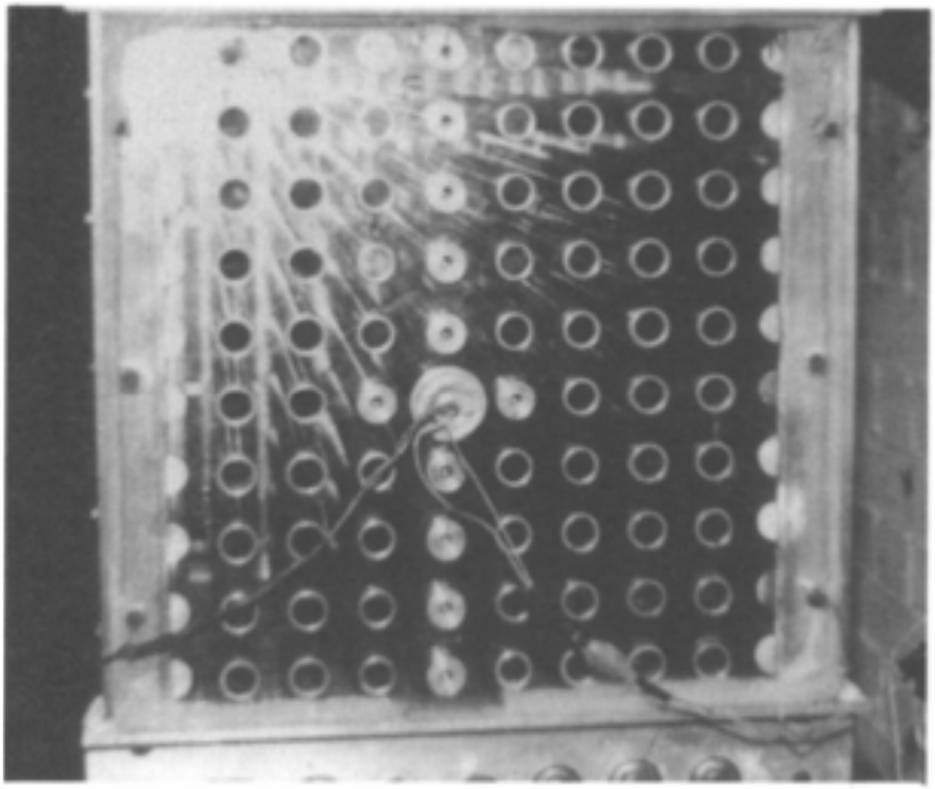

Figure C.2: Model heat exchanger (Murray 1993)

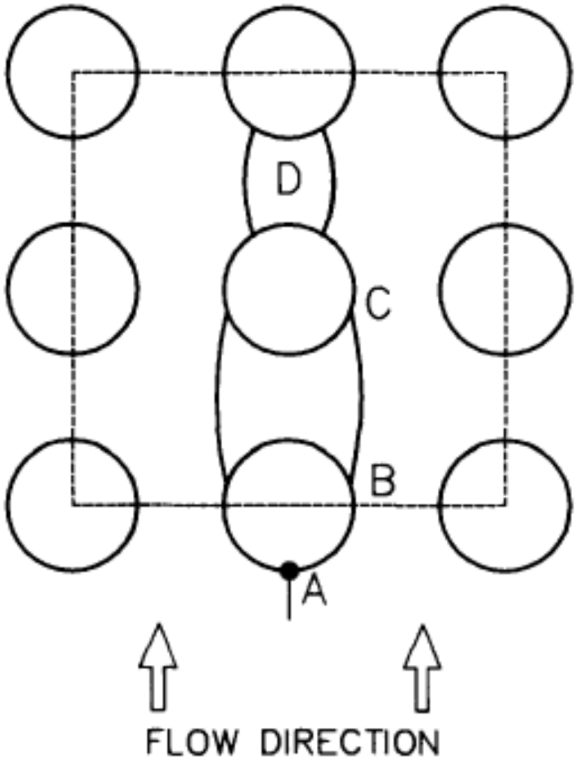

Figure C.3: Flow patterns in a tube bank. A, front stagnation point; B, boundary layer separation; C, flow reattachment; D, narrow wake (Murray 1993)

The experiments of Murray were simulated using ANSYS® Fluent in 2D with ambient air over the tube bank geometry displayed Figure C2. A constant tube surface temperature of 100 °C was specified. Simulations were performed at Reynolds numbers of 6000, 12000 and 24000. To check that the heat transfer coefficient calculation performed in his work was correctly interpreted, the VDI method was used to verify the CFD and experimental values.

Although good qualitative information could be gained from the work done by (Murray 1993), the data was only for Reynolds numbers of 6000 and 12000. These Reynolds numbers are higher than typical boiler applications. Therefore another well documented benchmark experiment was needed.

Zukauskas

The review paper of (Zukauskas 1972) explains the flow and heat transfer phenomena in tube banks very well and confirmed the findings of the Murray experiments.

The experimental setup for the results in Figure C.4 was modelled with ambient air over the tube bank and a constant tube surface temperature of 100 °C. It was decided to evaluate the CFD results globally (looking at the effect over the entire bank), per row and locally (around the tube).

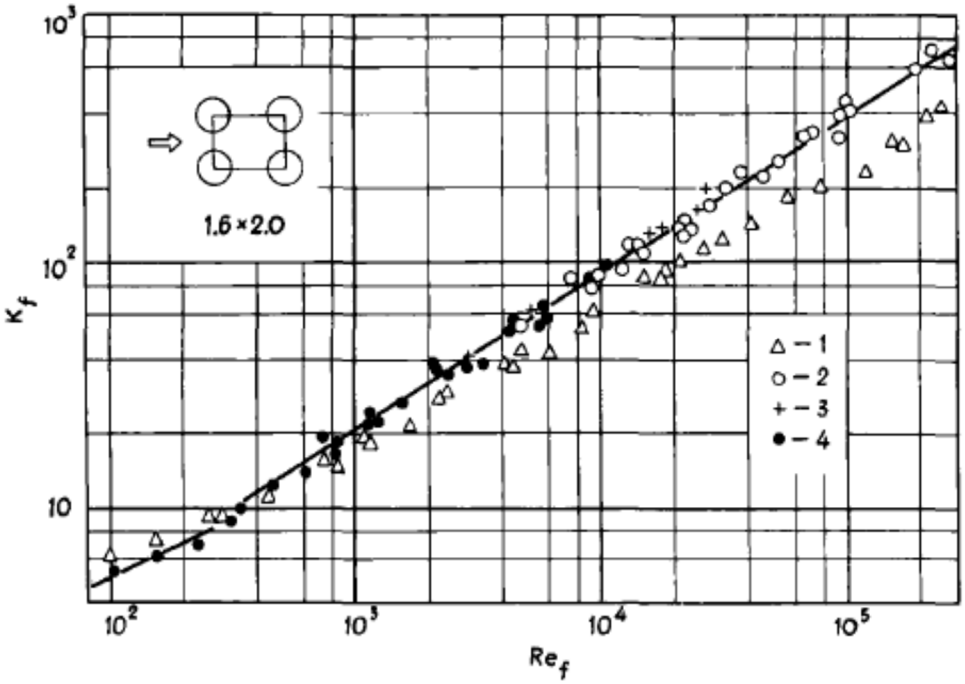

Figure C.4: Heat transfer of tubes of in-line banks, 1.6 x 2.0 – First row and 2, 3, 4 – inner rows in water, air and transformer oil, respectively (Zukauskas 1972)

From the lumped parameter model of Komati, Appendix B, the average Reynolds number is 4000 for the tube bank in the boiler simulation at full load. Thus a Reynolds number range from 1000 to 10000 was chosen for the evaluation in order to cater for variations in the flow field and future simulations of slightly different geometries or boiler loads.

VDI calculations were also performed using the geometry and conditions of the CFD simulation from a Reynolds number of 1000 to 10000.

The mesh used can be seen in Figure C.5.

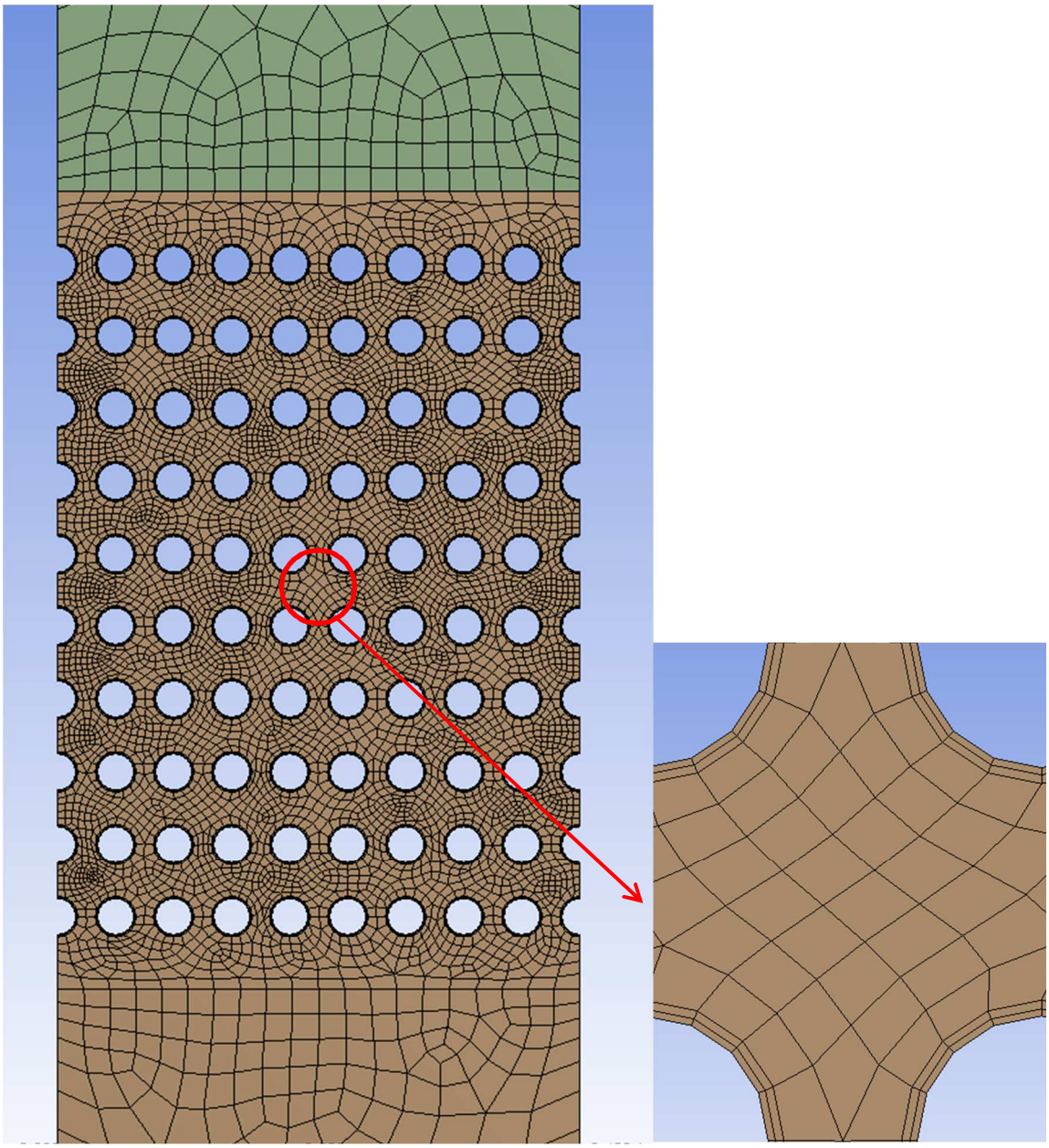

Figure C.5: 2D mesh used for Zukauskas experiment with 25.4 x 40.64 x 50.8 mm tube diameter, transversal pitch and longitudinal pitch

This investigation is divided into 3 sections for the findings using wall functions, a two layer method and LRN models.

C.1. Wall functions

Murray

On a global scale looking at the heat transfer over the entire bank, good correlation was achieved comparing the CFD results to the VDI calculations and experimental results at Reynolds numbers of 6000, 12000 and 24000. Standard wall functions and the blended wall functions by (Kader

1981) were used. The largest difference was 28 % at a Reynolds number of 24000 (see Figure C.6).

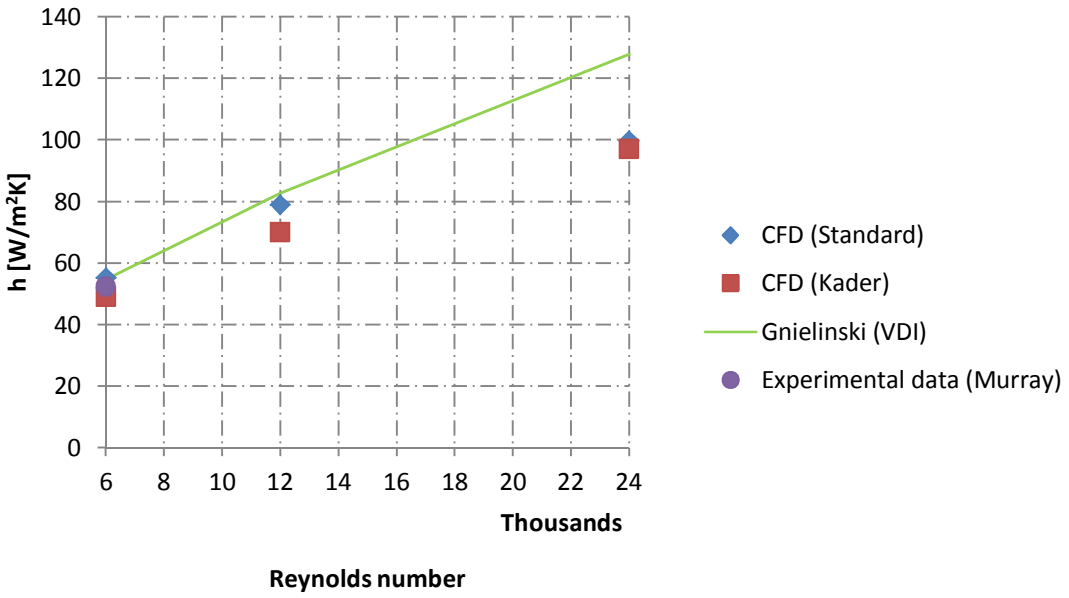

Figure C.6: Comparison of heat transfer coefficient from CFD results using standard and blended wall functions at 0.5mm FLT to empirical correlation of (Gnielinski 1979)

The CFD values of pressure drop differed from the VDI calculations by 16 %, 25 % and 11 % at Reynolds numbers of 6000, 12000 and 24000 respectively (see Figure C.7).

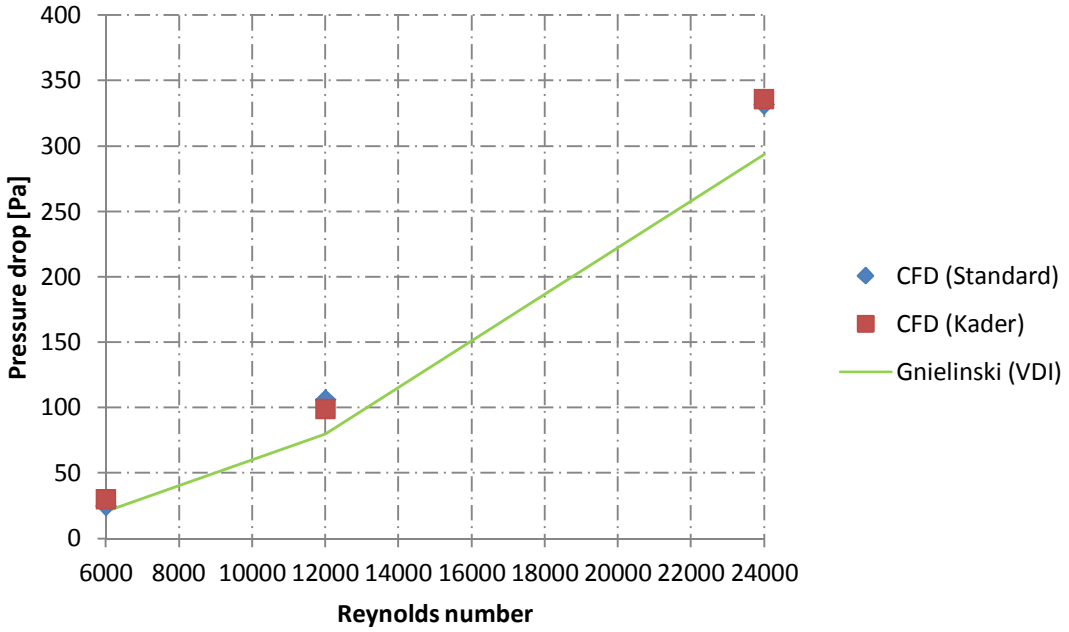

Figure C.7: Comparison of pressure drop from CFD results using standard and blended wall functions at 0.5mm FLT to empirical correlation of (Gnielinski 1979)

It was found that the CFD over predicted the heat transfer to the first row of tubes in the direction of flow and under predicted the following rows using both wall function formulations (see Figure C.8).

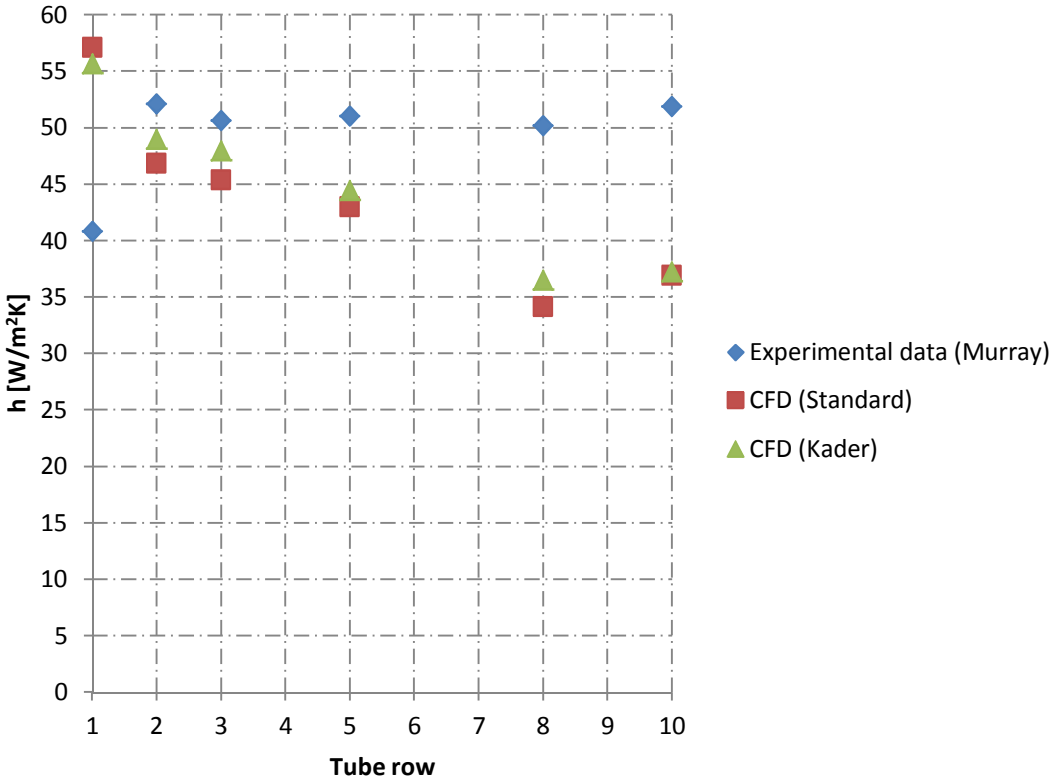

Figure C.8: Comparison of heat transfer coefficient from CFD results per tube row using standard and blended wall functions at 0.5mm FLT to empirical correlation of (Gnielinski 1979)

The heat transfer coefficient around the tubes was also checked (tube no. 1, 2 and 3 in the direction of air flow). Generally the same trend was seen as in the experimental results of (Murray 1993) (see Figures C.7 and C.8).

The CFD predictions for the first tube were closer to the data of (Murray 1993) using the blended wall functions by (Kader 1981) compared to using standard wall functions.

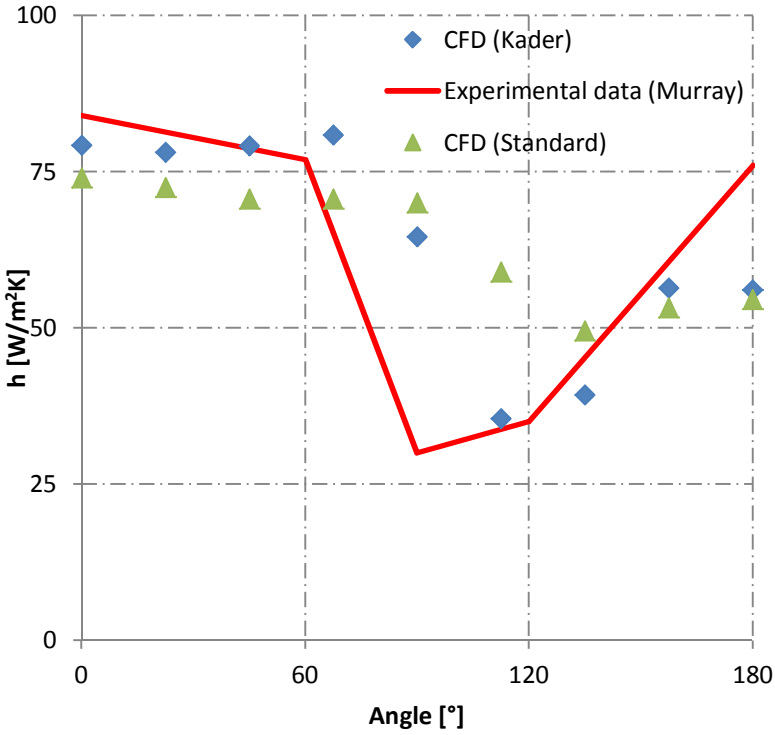

Figure C.7: Comparison of CFD results using standard and blended wall functions at 0.5 mm FLT to the experimental data of (Murray 1993) for heat transfer coefficient around first tube (0 ° at front of tube)

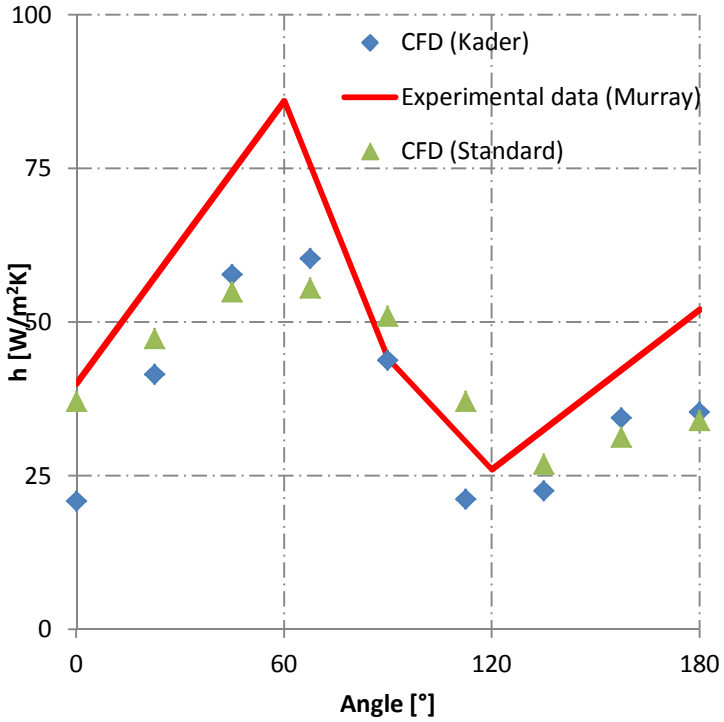

Figure C.8: Comparison of CFD results using standard and blended wall functions at 0.5 mm FLT to the experimental data of (Murray 1993) for heat transfer coefficient around third tube (0 ° at front of tube)

Due to the sensitivity of turbulence intensity on the heat transfer in the bank, a value of 0.5 % for wind tunnel conditions was used at the inlet to the domain.

The y^+-value varied from 3, for a Reynolds number of 6000, to 7.7, for a Reynolds number of 24000. This is the average y^+-value reported on the tube walls. The thickness of the first layer of cells (FLT) on the tube walls was 0.5 mm.

Zukauskas

The empirical correlations of (Zukauskas 1972) and (Gnielinski 1979) from the VDI were compared with the CFD results. The standard wall functions, blended wall functions by (Kader 1981), scalable wall functions (ANSYS Inc. 2013) and non-equilibrium wall functions by (Kim, Choudhury & Patel 1997) were used with the Realizable k-ε turbulence model.

The same grid resolution and first layer mesh thickness on the tube walls of 0.5 mm, used for the simulations of the experiments of (Murray 1993), were utilised with the standard wall functions.

The CFD results under-predicted the heat transfer coefficient by 12 % on average but followed the same trend from a Reynolds number of 1000 to 10000 compared to the VDI calculations using the formulas of (Gnielinski 1979) and the correlation of (Zukauskas 1972) (as can be seen in Figure C.9). The y^+-value varied from 0.9, for the Re number of 1000, to 4.3, for the Re number of 10000. This is the average y^+-value reported on the tube walls.

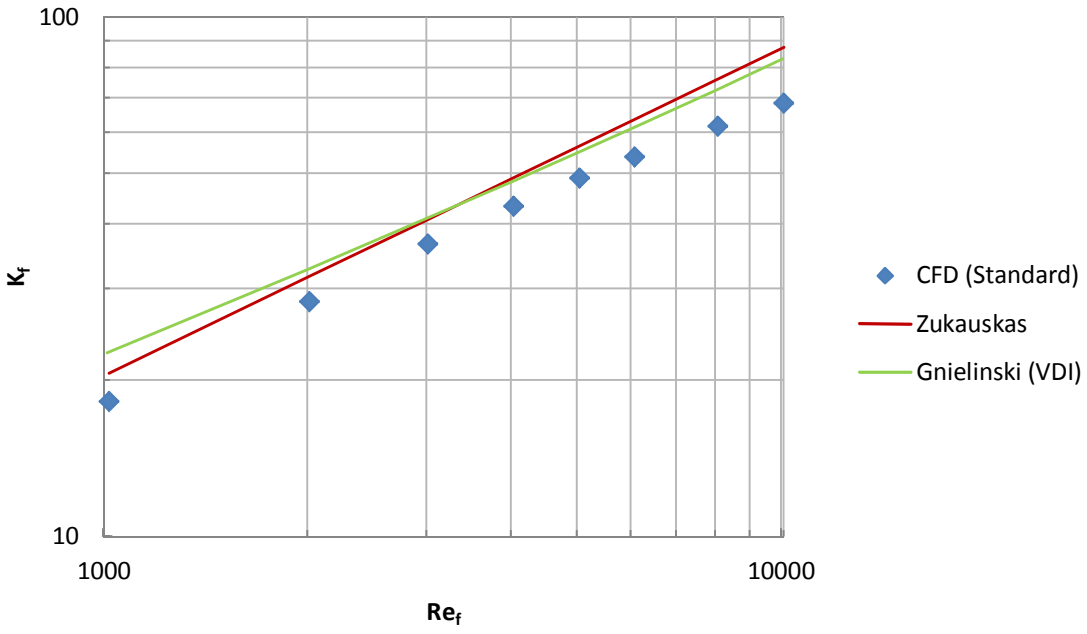

Figure C.9: Comparison of CFD results using standard wall functions to empirical correlations

A small improvement was noted using the blended wall functions by (Kader 1981) at a slightly higher y^+-value. At the new y^+ value of 6.2 on the upper limit at a Reynolds number of 10000, the standard wall functions under-predicted the heat transfer by 39 % as opposed to the blended wall

functions of 22 %.This was expected since the blended functions perform better in the buffer region for $3 < y^+ < 10$. The first layer thickness was 0.75 mm for this mesh (see Figure C.10).

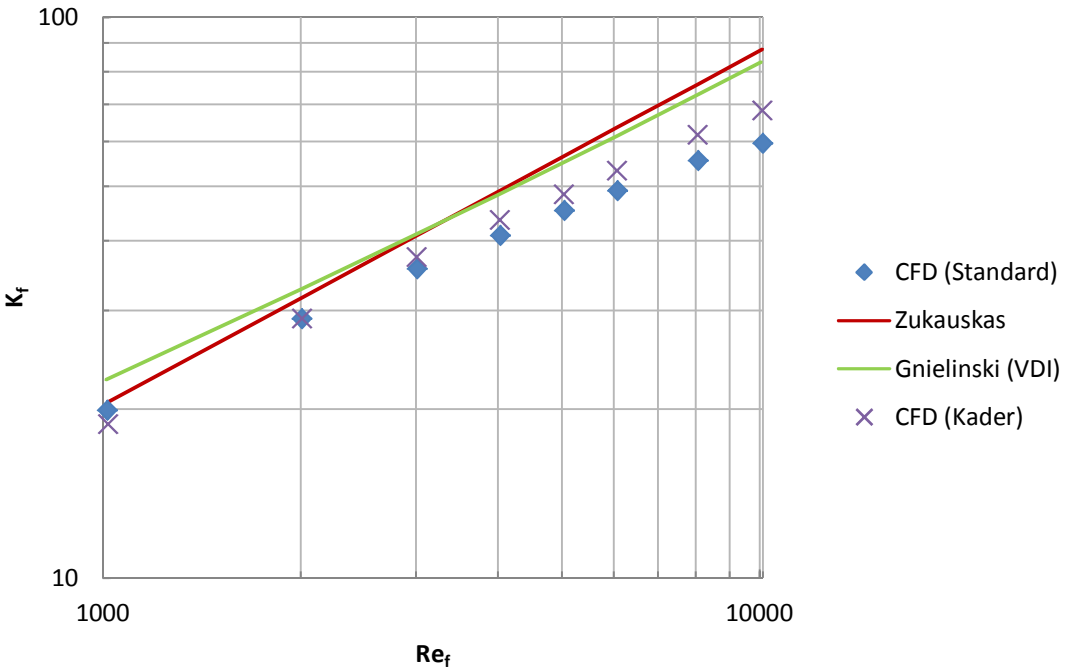

Figure C.10: Comparison of CFD results using standard and blended wall functions to empirical correlations

The grid resolution was increased until grid independence was reached considering pressure drop over the tube bank. See Figure C.11 for a comparison between the initial grid (7 746 cells) and resolution for independence with regards to pressure drop (21 623 cells).

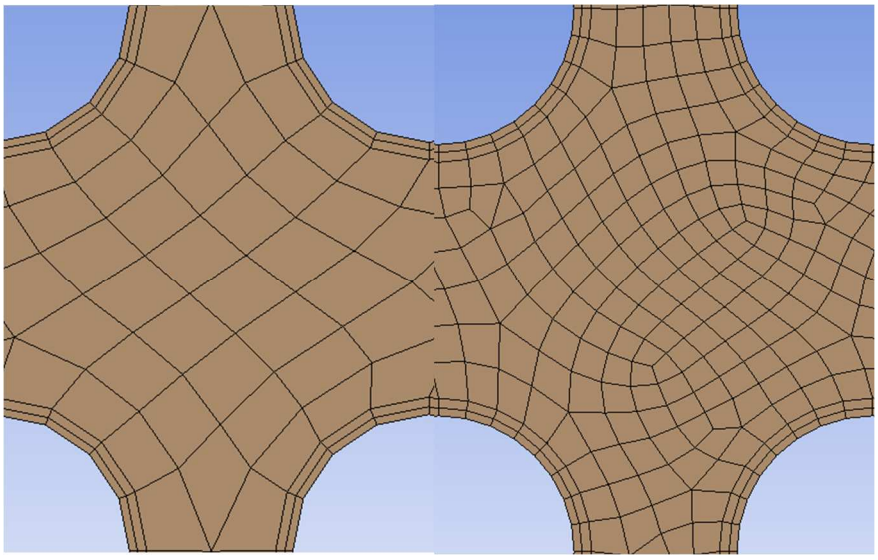

Figure C.11: The initial grid compared to the grid required for independence with regards to pressure drop

This resulted in only a slight improvement on heat transfer, but a considerable improvement on pressure drop comparing the CFD results to the VDI calculations (see Figure C.12).

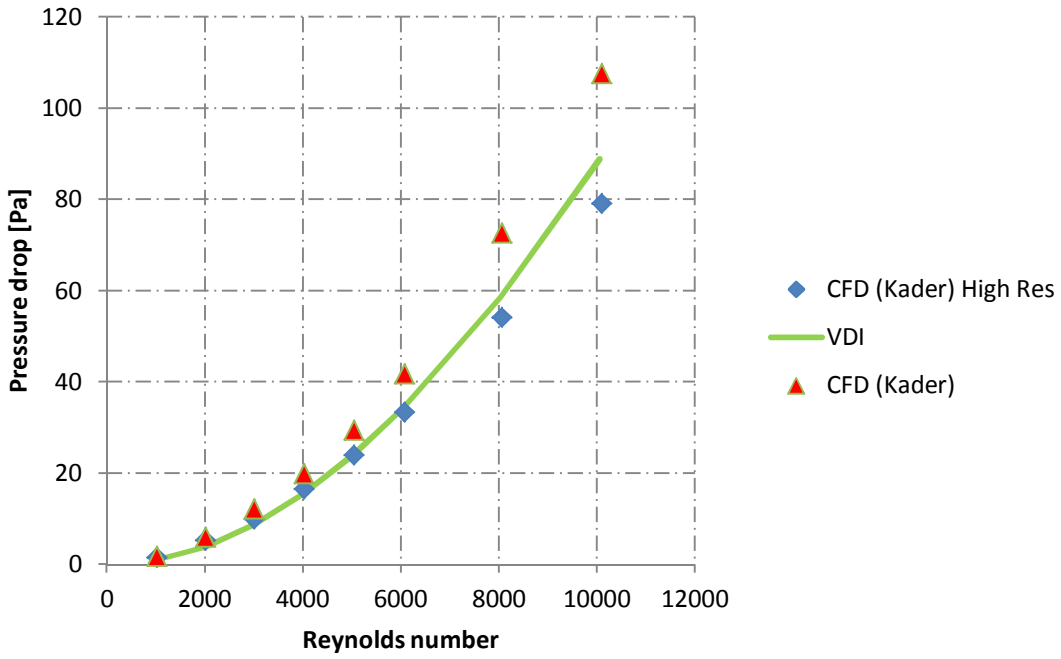

Figure C.12: Comparison of CFD results using blended wall functions to empirical correlations

Due to the substantial effect of the y^+-value on the tube heat transfer, simulations were run changing the first layer thickness (FLT) of the mesh on the tubes. This trial and error process was chosen since the traditional recommended y^+-value range of 30 to 300 was not found suitable.

The flow phenomena in the tube bank deviate substantially from flat plate flow due to the non-equilibrium characteristics as shown in Figure C.3. Therefore wall functions are not suitable and the aim of this study was to establish if it could be considered by evaluating the error made for the computational saving.

Since a Reynolds number range was evaluated for reasons stated before, from here on reference will be made to the average y^+-value at a Reynolds number of 4000 and FLT only, although the y^+-value varies for the Reynolds number range, around the tubes and throughout the bank.

The Blended wall functions were used for these comparisons due to the superior performance compared to standard wall functions.

The CFD results for heat transfer at a Reynolds number of 4000 compared the best with the empirical correlations using a FLT of 0.75 mm. The y^+-value was 3.7. See Figure C.10.

From a Reynolds number of 1000 to 10 000 blended wall functions captured the same trend as the heat transfer experiments, but with an overall heat transfer under prediction of 15 %.

The first row heat transfer was also over-predicted, similar to the results using the geometry of (Murray 1993). Using a thicker FLT on the first row increased the overall heat transfer error to approximately 16 %, but the heat transfer per tube row was more realistic.

Blended wall functions corrected for pressure gradients and thermal effects were tested and delivered better results than without these corrections (the under prediction decreased from 15 % to 10 % on average over the Reynolds number range from 1000 to 10 000) at 1mm FLT and y^+-value of 4.8 (see Figure C.13.

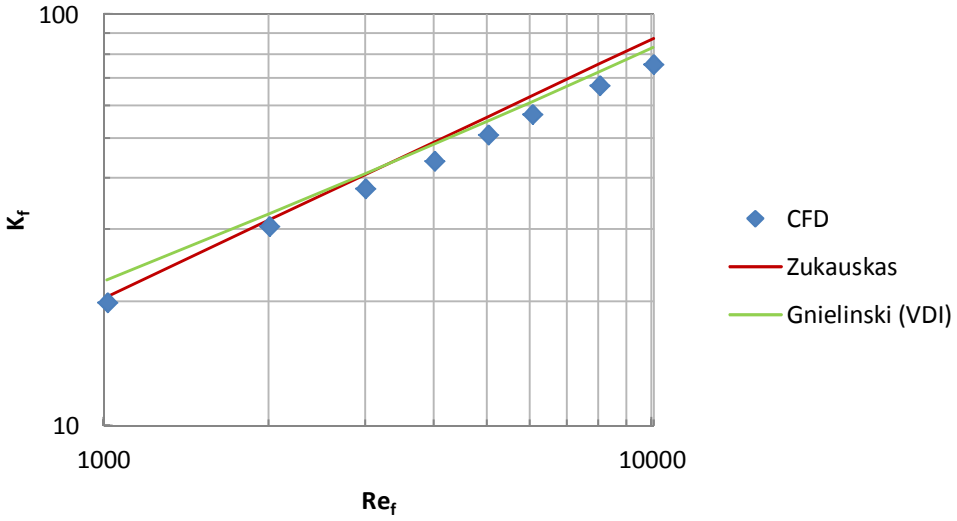

Figure C.13: Comparison of CFD using blended wall functions (corrected for pressure gradients and thermal effects) & 1 mm FLT to empirical correlations

The modification for pressure gradients and thermal effects were developed for compressible flows by (White & Christoph 1971) and (Huang, Bradshaw & Coakley 1993).

However the first row of the bank absorbed more heat than the rest, in contrast to experimental evidence where it absorbed 20 % less than other rows (see Figure C.14).

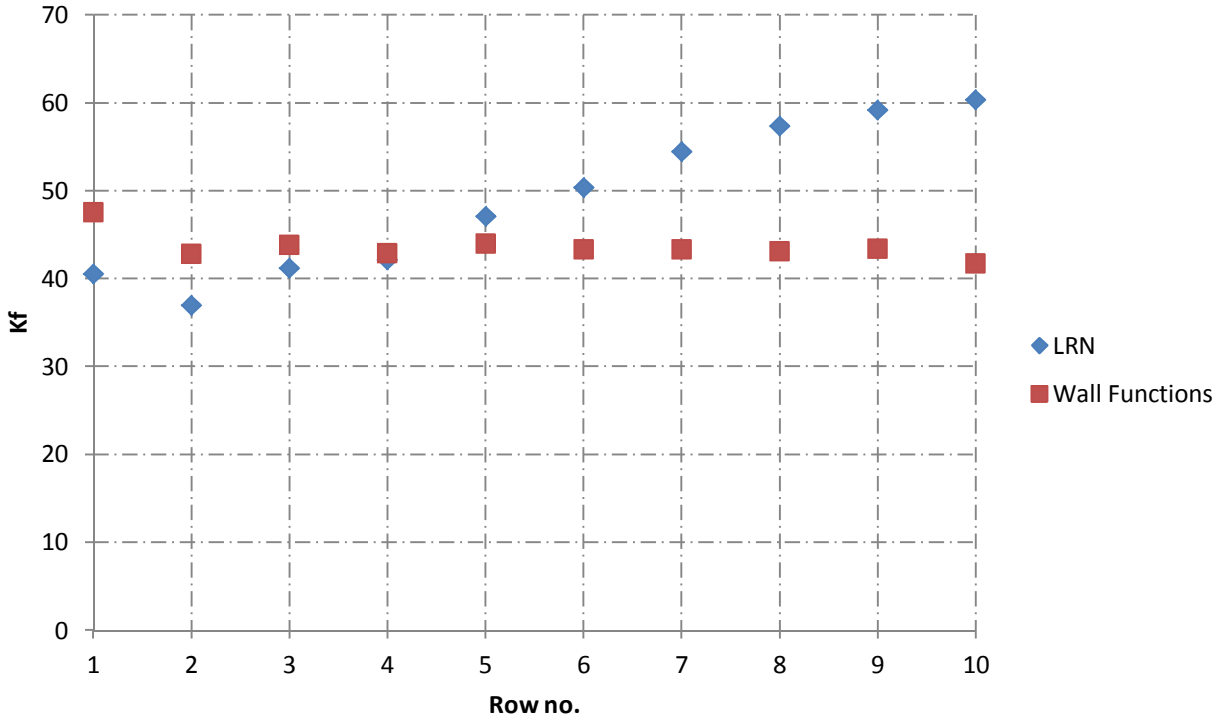

Figure C.14: Heat transfer coefficient per row at a Reynolds number of 4000 for CFD using blended wall functions (corrected for pressure gradients and thermal effects) and a LRN with1 mm and 0.35 mm FLT respectively

Experiments with a thicker FLT on the first row were conducted. A FLT of 2 mm on the first row and 0.75 mm on the rest of the tubes resulted in a realistic heat transfer distribution per row, while still maintaining the best overall absolute value of heat transfer over the bank. The results were however lower than using only 0.75 mm for the FLT.

The effect of an increased grid resolution on heat transfer per row was found to be negligible as seen with the study of the work done by (Murray 1993).

The local heat transfer coefficient around the tube was plotted for the 2nd row to compare to experimental data (see Figure C.15). It was found that the overall trend was the same, but the absolute values for the front part of the tube were lower and the peak value higher than the experimental data.

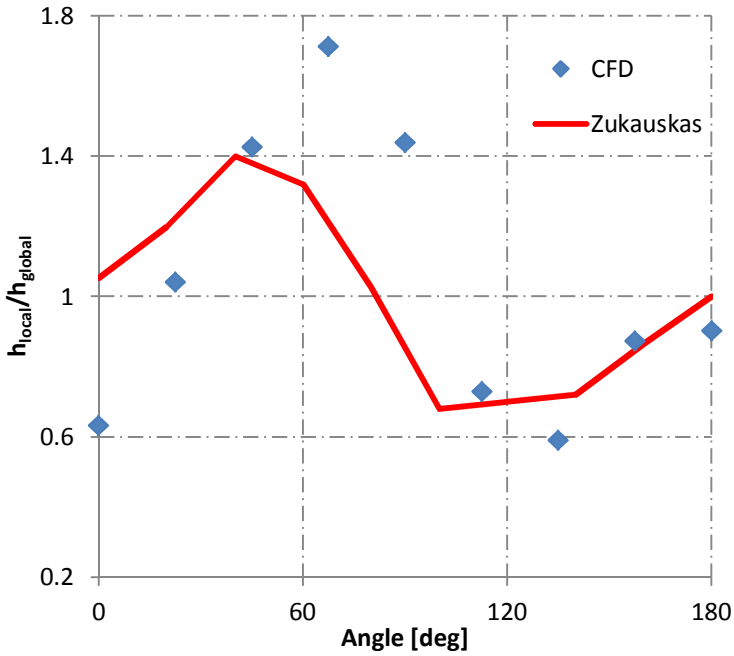

Figure C.15: Comparison of CFD results using blended wall functions corrected for pressure gradients and thermal effects to Zukauskas experiments for heat transfer coefficient around in – bank tube (0 ° at front of tube)

Scalable wall functions produced similar results to the blended functions.

Non-equilibrium wall functions were developed for flow involving separation, reattachment and impingement, (ANSYS Inc. 2013). It was implemented with different values of FLT.

This trial and error approach was again used since (Kim, Choudhury & Patel 1997) used a wide range of y^+-values during validation as discussed in Chapter 4.

The back step validation study was the closest to the current tube bank configuration. The y^+-value range was 13 to 22 for the back step simulation. Grid independence was checked for pressure drop over the tube bank. The increased mesh resolution had negligible effects on heat transfer.

The best results were achieved at a FLT of 0.75 mm and y^+ -value of 4.8. From a Reynolds number of 4000 to 10 000 non-equilibrium wall functions produced results closer to the empirical correlations, but over-predicted heat transfer considerably for a Reynolds number of 3000, 2000 and 1000 (see Figure C.16).

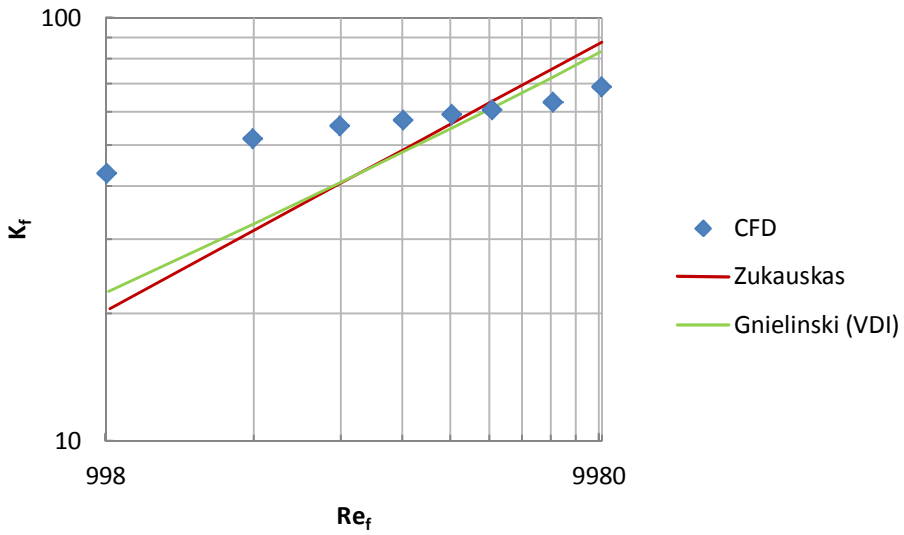

Figure C.16: Comparison of CFD using non-equilibrium wall 0.75 mm FLT to empirical correlations

A realistic heat transfer distribution per row was however predicted (see Figure C.17).

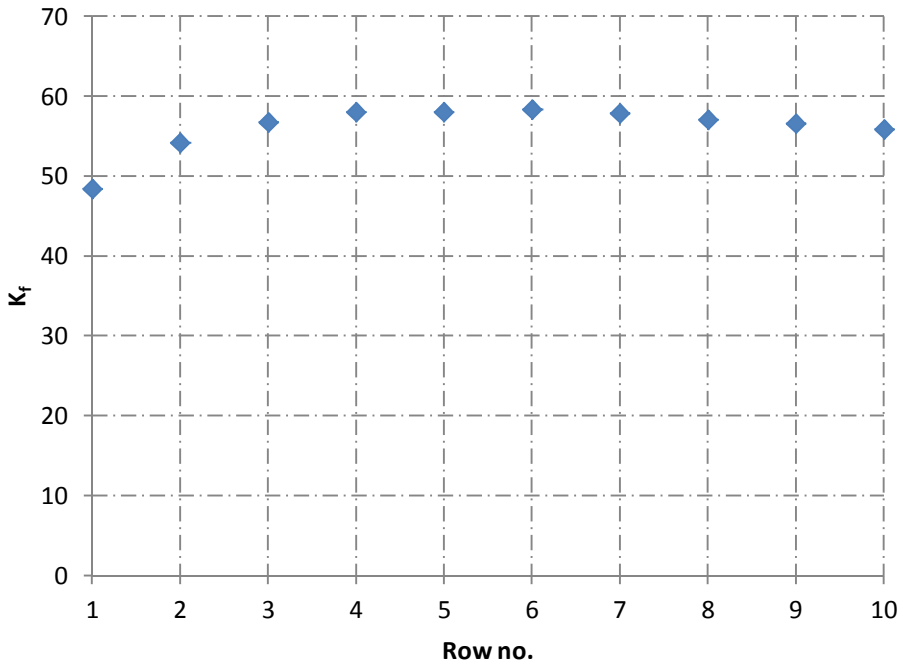

Figure C.17: Heat transfer coefficient per row at a Reynolds number of 4000 for CFD results using non-equilibrium wall functions

C.2. Two-layer zonal model

The two-layer near wall treatment approach of (Wolfshtein 1969) with the Realizable k-ε turbulence model was evaluated with the Zukauskas geometry. A y^+-value of less than 4 is recommended with at least 10 cells in the viscosity-affected near-wall region, as described in Chapter 4.

Different FLT values (corresponding to y^+-values within the recommended range) and amount of cells in the near-wall-region were used, but even the best combination resulted in a 33 % under-prediction of global heat transfer over the entire tube bank (see Figure C.18). The FLT value was 0.05 mm with 15 layers of cells near the wall at a y^+-value of 0.3.

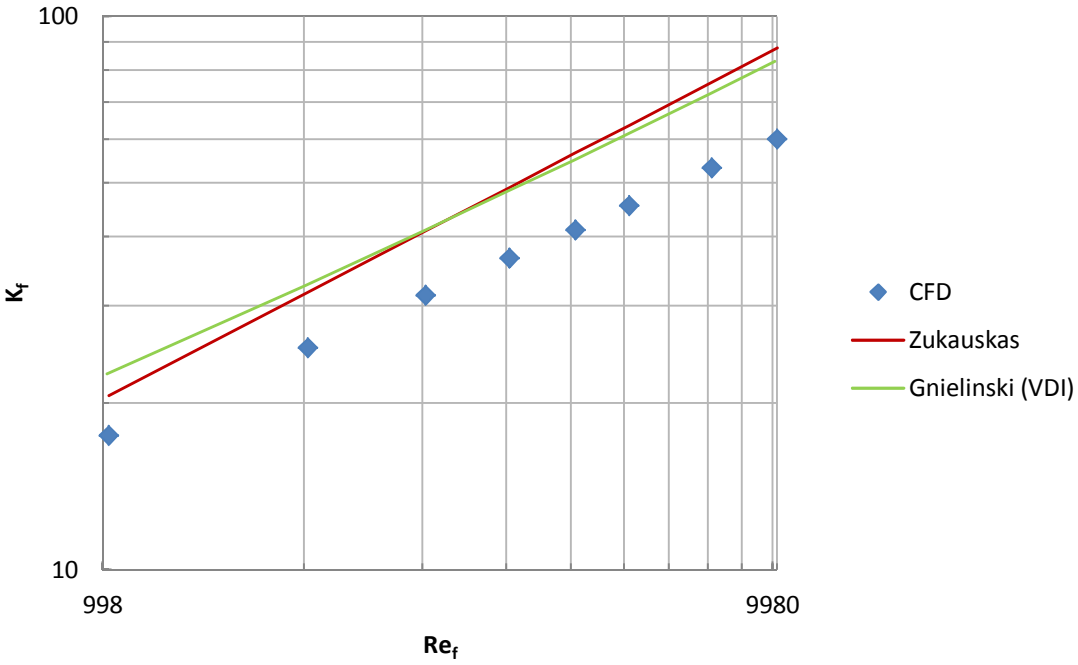

Figure C.18: Comparison of CFD results using the model of (Wolfshtein 1969) & 0.05 mm FLT to empirical correlations

The two-layer model of (Wolfshtein 1969) is part of the suite of models called "enhanced wall treatment" in ANSYS® Fluent. This suite alternates between blended wall functions and the two-layer model as described in Chapter 4.

A combination of these two approaches was tested at higher y^+-values than 1. The best performance was achieved with a FLT of 0.5 mm at a y^+-value of 2.7. However the global heat transfer was under-predicted by 20 % (see Figure C.19).

Due to the poor global performance of this model, no further detailed analysis was done.

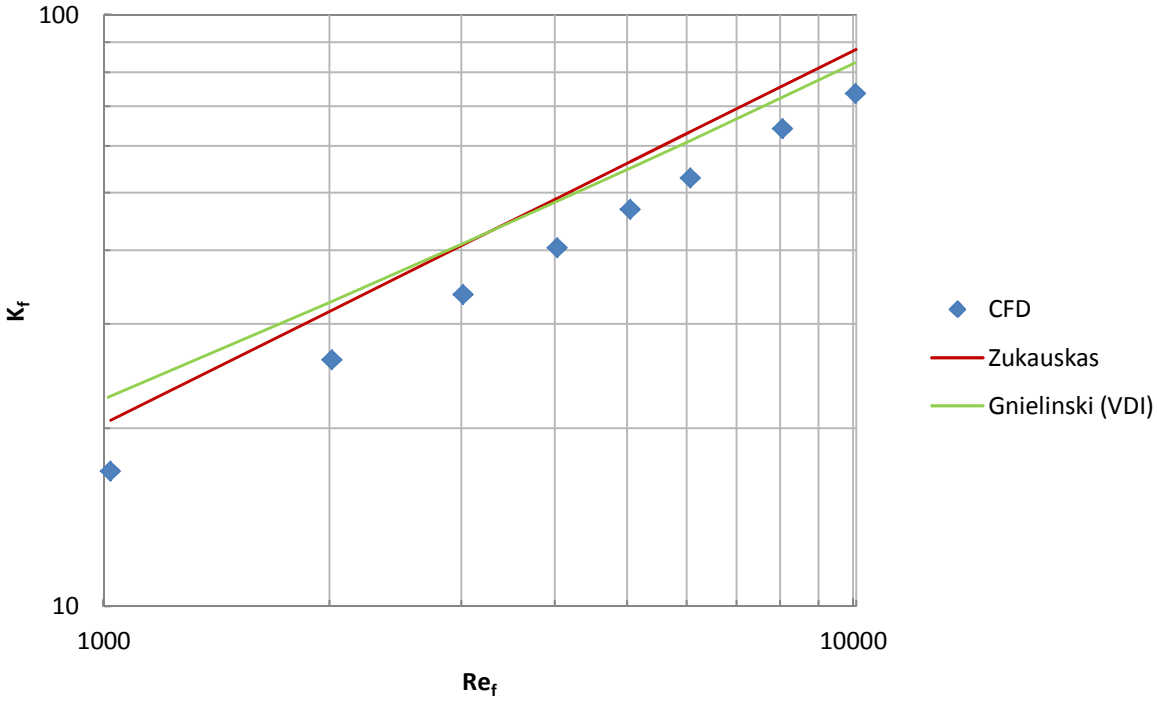

Figure C.19: Comparison of CFD results using the model of (Wolfshtein 1969) in combination with the blended wall functions of (Kader 1981) & 0.5 mm FLT to empirical correlations

C.3. Low-Reynolds-Number (LRN) k-ε turbulence models

The Low-Reynolds-Number (LRN) k-ε turbulence model of (Chang, Hsieh & Chen 1995) was evaluated with the Zukauskas geometry. A y^+-value of less than 4 is recommended as described in Chapter 4.

Different FLT values (corresponding to y^+-values within the recommended range) and amount of layers were used. The best combination resulted in an exact correlation of heat transfer with the experiments conducted by (Gnielinski 1979) and (Zukauskas 1972) at a Re value of 4000 as can be seen in Figure C.20.

The FLT value was 0.35 mm with 5 layers at a y^+-value of 2. Interestingly this is the same FLT used for the TSB Komati superheater geometry that resulted in the best fit with the empirical correlations. However the y^+-value for the Komati geometry was 0.7.

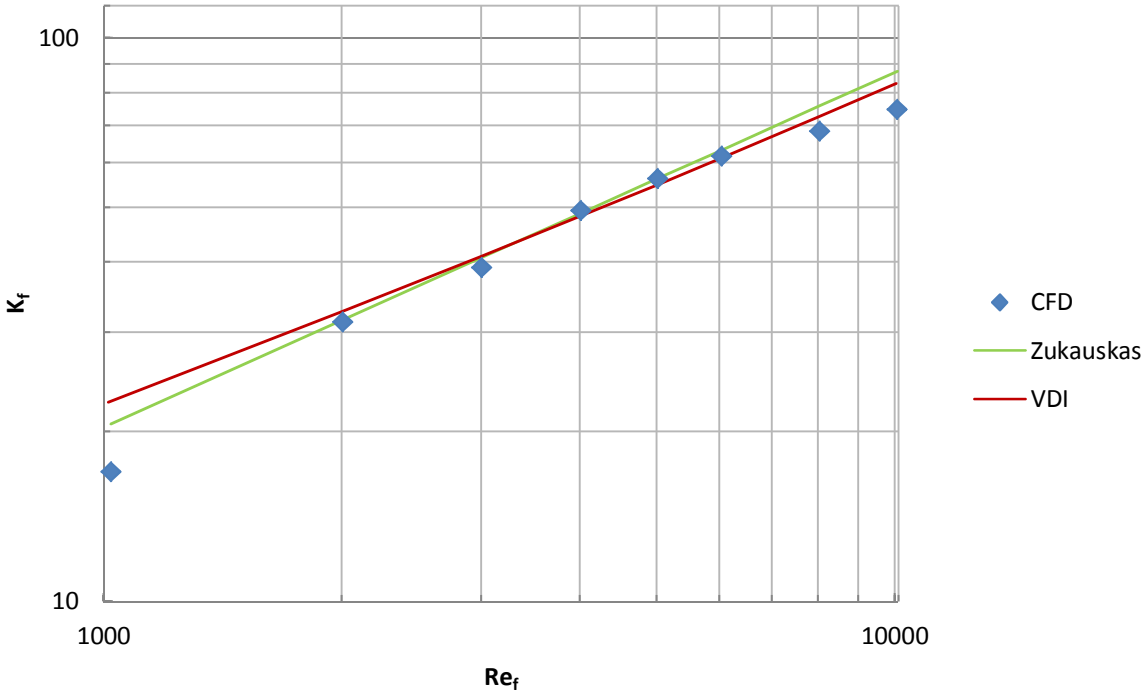

Figure C.20: Comparison of CFD using the LRN of (Chang, Hsieh & Chen 1995) & 0.35mm FLT to empirical correlations

The heat transfer distribution per row is more realistic than using blended wall functions. The first row heat transfer is lower than the in bank-tubes, as can be seen in Figure C.14.

The heat transfer coefficient distribution around tube no.2 is also more realistic since the peak value is at 1.4 in accordance with (Zukauskas 1972) as opposed to 1.8, comparing Figure C.15 to Figure C.21.

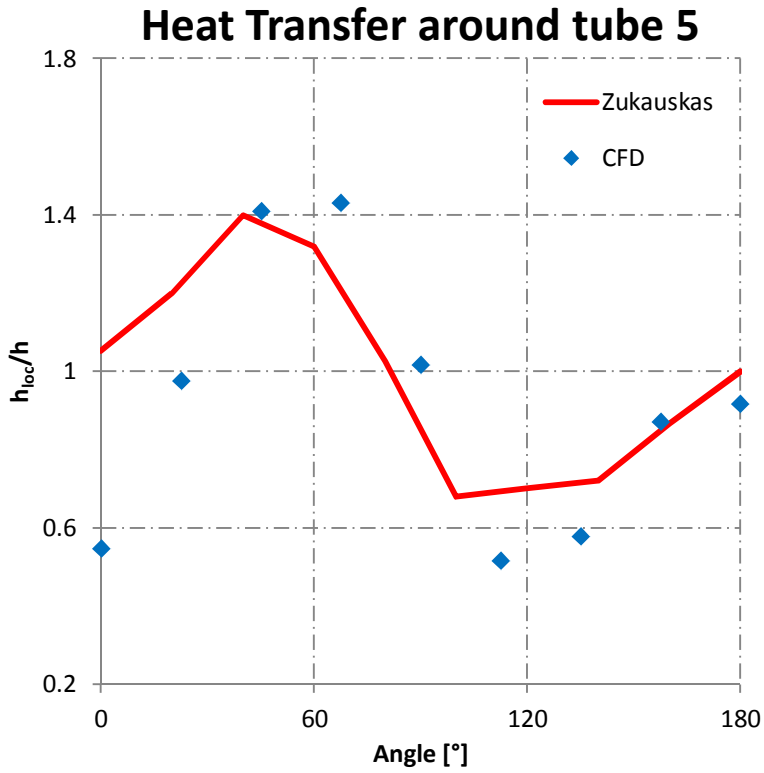

Figure C.21: Variation of local heat transfer of a tube in an in-line bank, CFD results (blended wall functions corrected for pressure gradients and thermal effects)

C.4. Conclusions from using different turbulence near-wall treatment

Considering the three turbulence wall treatment approaches evaluated, the best fit with experimental results was achieved using the LRN k-ε turbulence model of (Chang, Hsieh & Chen 1995).

Globally looking at the heat transfer over the entire tube bank the best wall function fit with the experimental data was using the blended formulas of (Kader 1981) with corrections by (White & Christoph 1971) and (Huang, Bradshaw & Coakley 1993) at a heat transfer under-prediction of 10 %.

The two-layer near wall treatment approach of (Wolfshtein 1969) under predicted the global heat transfer by 20 %.

The LRN k-ε turbulence model of (Chang, Hsieh & Chen 1995) correlated with the experimental results of global heat transfer exactly.

The heat transfer per tube row could be captured realistically only using the LRN k-ε turbulence model of (Chang, Hsieh & Chen 1995) and the non-equilibrium wall functions of (Kim, Choudhury & Patel 1997).

The CFD results of heat transfer rate around the circumference of a tube in an in-line bank was the closest to experimental results using the LRN k-ε turbulence model of (Chang, Hsieh & Chen 1995).

Appendix D: Application of CFD model

As mentioned before, the current co-generation drive in the RSA led to the need for higher pressure, more efficient boilers. This presents challenges with e.g. new superheater designs and thus more detailed modelling is needed as steam temperature is critical in order to achieve the required turbine performance.

Therefore after reaching the objectives of this study, the methodology was applied to a new superheater design for an 80 bar pressure, 525 °C steam temperature industrial boiler (see Figure D.1).

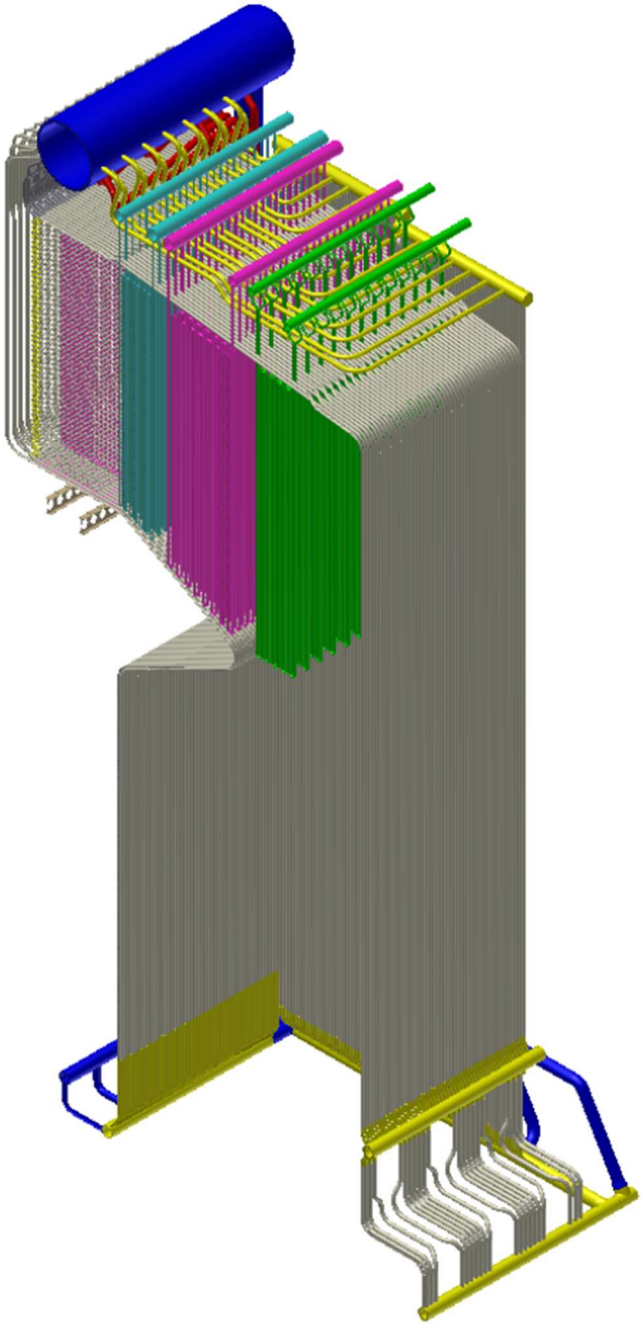

Figure D.1: 80 bar industrial boiler design

The mesh of this simulation is 60 million cells (see Figure D.2). It was extremely challenging and time consuming to set up. The large mesh also resulted in a very long solving time. However the results were worth the effort. As expected the CFD results differed from the lumped parameter approach.

Currently the two methods will be used conservatively in combination until the CFD model is further validated. However considering the shortcomings of the lumped parameter approach, the size and arrangement of this design, the CFD results carry the most weight.

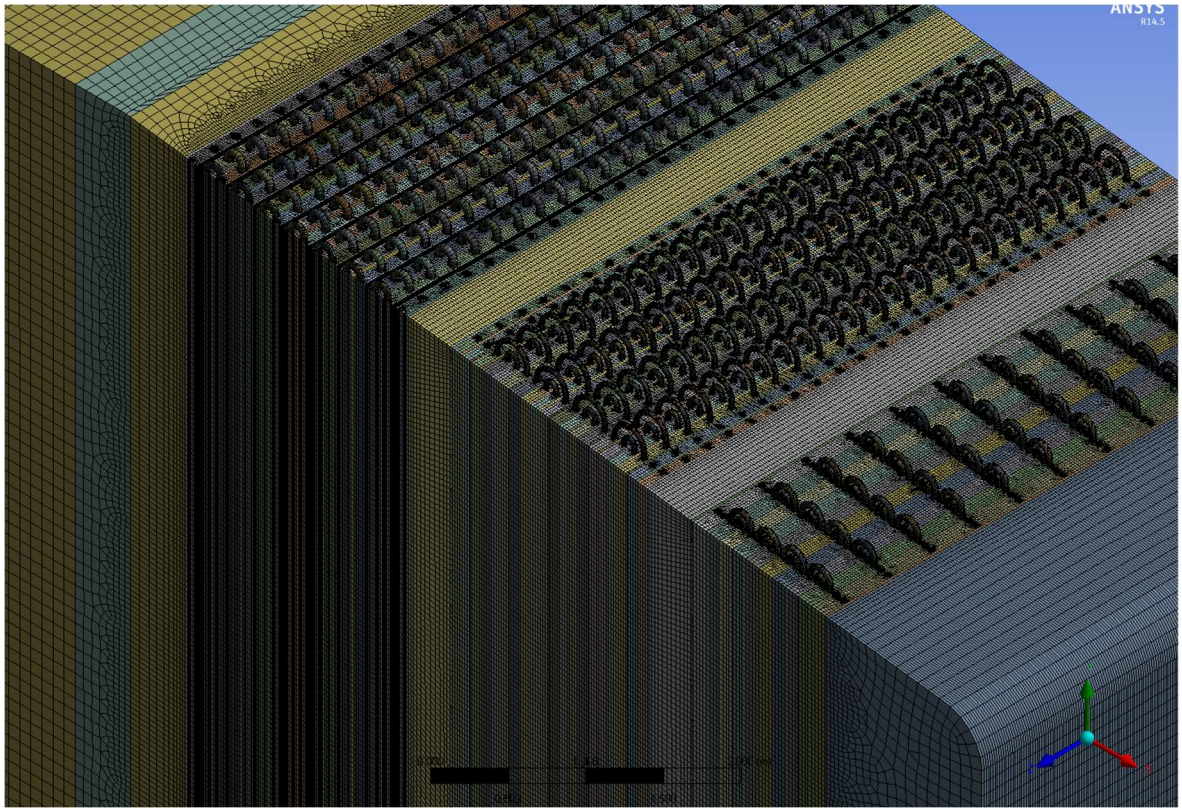

Figure D.2: Top section of 80 bar industrial boiler superheater